# Scanning Probe Energy Loss Spectroscopy (SPELS) of Structured Surfaces

by

Karl Bauer

A thesis submitted to the
University of Birmingham
for the degree of
Doctor of Philosophy

Nanoscale Physics Research Laboratory
School of Physics and Astronomy
University of Birmingham
April 2015

# Abstract

In scanning probe energy loss spectroscopy (SPELS) an STM tip is used as a localised source of field emitted electrons by applying a high voltage. Energy loss measurements of the backscattered electrons provide spectroscopic information from the sample. The energy resolution is $\approx 0.3$ eV. In principle, a raster scan provides a spatially resolved image of these excitations. In this work, a new generation instrument is employed and developed in which the electrons are captured by an electrostatic lens system and focussed onto a multichannel detector using a 127° cylindrical-sector analyser. Additionally, a compact retarding field analyser has been built, which can be placed within 20 mm of the tip position. Both detectors have been positioned at an angle of 7° to the surface plane, as most of the backscattered electrons are expected to emerge near the surface plane due to the high electric field between tip and sample. Ag and Au nanostructures on graphite designed for the SPELS instrument covering a large sample area have been prepared by electron beam lithography. The characteristics of the instrument have been measured, with high spatial resolution (down to 25 nm) images showing various contrast mechanisms. Spatially resolved silver surface plasmon maps are presented.

Für Julia und Robert

# Acknowledgements

I thank my supervisor Professor Richard E. Palmer for the opportunity to work on this project and for his guidance during this project. I also thank Dr. Shane Murphy for the initial training, the great time in the lab and for proof reading of this thesis. I thank Tianluo Pan and Lin Tang for their help in the lab. My thanks to William Terry, Scott Holmes, Andreas Frommhold and Dr. Simon Plant for proof-reading of my thesis. Special thanks are due to Dr. Wolfgang Theis and Dr. George Barreto for many helpful discussions. I thank the NPRL group for the great time.

I thank Yu Chen for the loan of the ORTEC electronics for the CEM and Paul Jagpal for the loan of the NIM crate.

I like to thank my family for their constant support. Special thanks go to Julia for her great patience and support during the last years.

# Contents

**List of Figures** **X**

**List of Tables** **XI**

**List of Abbreviations** **XII**

**Table of Symbols** **XIV**

**1 Introduction and Background** **1**

1.0 Perspective . . . . . 1
1.1 Surfaces on the Sub-100 nm Scale . . . . . 3
1.2 Scanning Tunnelling Microscopy and Scanning Tunnelling Spectroscopy 4
1.2.1 Scanning Tunnelling Microscopy . . . . . 4
1.2.2 Scanning Tunnelling Spectroscopy . . . . . 8
1.3 Field Emission . . . . . 10
1.4 Scanning Probe Energy Loss Spectroscopy . . . . . 14
1.4.1 Historical background . . . . . 16
1.4.2 Previous work at NPRL . . . . . 17
1.4.3 Electron scattering . . . . . 23
1.5 Existing Elemental Imaging Techniques . . . . . 28
1.5.1 AES . . . . . 29
1.5.2 EELS . . . . . 29
1.5.3 PEEM, XPS, UPS . . . . . 30
1.5.4 SIMS . . . . . 31
1.5.5 Summary . . . . . 33

**2 Experimental Apparatus** **35**

2.0 Perspective . . . . . 35
2.1 Ultra High Vacuum System . . . . . 36
2.2 Scanning Tunnelling Microscopy Head . . . . . 38
2.3 Electron Energy Analyser . . . . . 41
2.4 In situ Sample Preparation . . . . . 42
2.5 SPELS Software Environment . . . . . 43

**3 Development of SPELS Instrument** **45**
3.0 Perspective . . . 45
3.1 Retarding Field Analyser . . . 46
3.1.1 Method of Operation . . . 46
3.1.2 Design . . . 47
3.1.3 Detector . . . 49
3.1.3.1 Pulse Counting Mode . . . 51
3.1.3.2 Analog Mode . . . 54
3.1.4 SIMION simulations for the Retarding Field Analyser . . . 55
3.2 Fabrication and Characterisation of Tungsten Tips . . . 61
3.2.1 Electrochemical etching of tungsten tips . . . 61
3.2.2 Optimisation of the electrochemical etching setup . . . 63
3.2.3 Characterisation of Tips . . . 65
3.2.3.1 Scanning Electron Microscopy of Tips . . . 65
3.2.3.2 Tip dependence on etching parameters . . . 67
3.2.4 Cleaning of etched tungsten tips . . . 70
3.3 *In situ* Tip Conditioning Stage . . . 70
3.3.1 Design of the tip conditioning stage . . . 71
3.3.2 Software controller for the tip conditioning stage . . . 72
3.3.3 Tip preparation methods . . . 72
3.3.3.1 Field emission . . . 74
3.3.3.2 Field-surface-melting . . . 76
3.3.3.3 Self sputtering . . . 80
3.3.3.4 E-beam heating . . . 81
3.3.4 Summary . . . 81
3.4 Software Developments . . . 82
3.4.1 MCA controller . . . 82
3.4.1.1 Setting up Lens Voltages . . . 82
3.4.1.2 Fowler Nordheim Plot . . . 84
3.4.1.3 Detector Calibration . . . 85
3.4.2 RFA controller . . . 86
3.4.3 SPELS Image Processing . . . 88

**4 Creation of Nanostructured Surfaces** **91**
4.0 Perspective . . . 91
4.1 Evaporator . . . 92
4.2 Electron Beam Lithography . . . 96
4.2.1 Method . . . 96
4.2.2 Reduction of structure size . . . 102
4.2.3 EBL Pattern Layout Optimisation . . . 103
4.2.4 Silver structures on HOPG by EBL . . . 105
4.2.5 Gold structures on HOPG by EBL . . . 106
4.3 Summary . . . 107

**5 SPELS Performance and Images of Nanostructured Surfaces** **108**
5.0 Perspective . . . 108
5.1 Field emission performance . . . 109
5.2 SIMION simulations of SPELS . . . 111
5.3 Comparison of Detectors: Energy resolution and signal to noise . . . 114
5.3.1 SPELS with the MCA . . . 115
5.3.2 SPELS with the RFA . . . 118
5.4 Energy loss images due to plasmon excitation . . . 123
5.5 Imaging via the electron reflectivity contrast . . . 129
5.5.1 Negative reflectivity contrast . . . 130
5.5.2 Positive reflectivity contrast . . . 133
5.6 Nonlinear Field Effects . . . 141
5.7 Summary . . . 144

**6 Summary and Outlook** **145**
6.1 Summary . . . 145
6.2 Outlook . . . 150
6.2.1 Towards next generation SPELS . . . 151

**Appendices** **153**

**A Derivation of the Spot Size of the Evaporator** **153**

**B Set up of Electron Lens Voltages** **155**

**C Characterisation of Tips and Samples: AFM and SEM** **158**
C.1 AFM . . . . . 158
C.2 SEM . . . . . 162

**List of References** **164**

# List of Figures


1.1 Schematic of the STM instrument . . . . . 5
1.2 Energy diagram of the STM tunnelling junction . . . . . 5
1.3 Schematic illustration of the distortion effect due to the tip geometry . . 8
1.4 Schematic of the potential barrier for field emission . . . . . 11
1.5 Schematic of the SPELS instrument . . . . . 14
1.6 Structure of an energy loss spectrum . . . . . 15
1.7 SPELS spectra for different detector angles . . . . . 17
1.8 SPELS images demonstrating edge effect . . . . . 18
1.9 Schematic of contrast mechanism in SPELS images . . . . . 19
1.10 SPELS images demonstrating blocking effect . . . . . 19
1.11 Calculated electron distribution and SPELS resolution . . . . . 20
1.12 Schematic of a co-axial tip for SPELS . . . . . 22
1.13 Energy dependence of the electron mean free path . . . . . 25
1.14 Ion current density profiles . . . . . 32

2.1 Photograph of the SPELS instrument . . . . . 36
2.2 STM-1 . . . . . 38
2.3 STM-1 details of sample support . . . . . 40
2.4 Schematic of the Electron Energy analyser with electron lens system . . 42

3.1 Sketch and Photograph of the Retarding Field Analyser . . . . . 47
3.2 RFA flange design . . . . . 49
3.3 Electron Detection Efficiency . . . . . 50
3.4 RFA signal during a CEM high voltage sweep . . . . . 52
3.5 RFA electronics for pulse counting mode . . . . . 53
3.6 Input protection circuit for picoammeter . . . . . 54
3.7 2-dimensional electron paths in the RFA . . . . . 56
3.8 SIMION simulated spectra for the Retarding Field Analyser (RFA) . . . 59
3.9 SIMION simulation of the Retarding Field Analyser . . . . . 60
3.10 Modified tip etching stage . . . . . 64
3.11 New custom tip etching beaker . . . . . 64
3.12 SEM image of a STM tip . . . . . 66

3.13 SEM reference tips . . . 67
3.14 Schematic of tip geometry . . . 68
3.15 Tip apex diameter versus tip length for different etching voltages and modes . . . 68
3.16 Photograph of the tip conditioning stage . . . 71
3.17 Tip conditioning stage controller . . . 72
3.18 FEMM simulation of an STM tip . . . 74
3.19 field intensity during field emission tests . . . 75
3.20 Field emission test of tip208 . . . 77
3.21 Field emission test of tip209 . . . 78
3.22 SEM image of tip used for field-surface-melting . . . 79
3.23 Field-surface-melting results . . . 80
3.24 Serial digital signal to set a lens voltage . . . 83
3.25 LabView front panel for the electron lens voltage setup . . . 84
3.26 LabView front panel for detector calibration . . . 86
3.27 Direct comparison of calibration methods using "AN1" and FE voltage . 87

4.1 Photograph of the new evaporator . . . 93
4.2 AFM and SEM images of a Ag/HOPG sample and TEM quantifoil grid 95
4.3 AFM image (tapping mode) of Ag islands on graphite . . . 96
4.4 SEM image of sample HS14 showing stitching errors . . . 98
4.5 SEM dosetest with sample HS16 . . . 99
4.6 EBL lift-off . . . 100
4.7 EBL lift-off failure . . . 100
4.8 SEM images of silver structures on sample HS1 . . . 101
4.9 SEM image of failed lift-off . . . 102
4.10 SEM image of 50 nm silver islands prepared by EBL . . . 103
4.11 EBL sample layout using patterned areas of 200 µm×40 µm . . . 104
4.12 EBL sample layout using the full writefield . . . 104
4.13 SEM images of Ag nanostructures prepared by EBL . . . 105
4.14 AFM images of Au nanostructures prepared by EBL . . . 106

5.1 Backscattered electron count rate versus FE current . . . 109
5.2 Tip-sample separation versus backscattered electron count rate . . . 110
5.3 Tip annealing effect on count rate . . . 110
5.4 SIMION simulation for backscattered electrons . . . 112

5.5 Simulated probing area using SIMION . . . 113
5.6 PA displacement as a function of tip-sample separation . . . 113
5.7 SPELS spectra of Au and Ag . . . 115
5.8 SPELS spectra of HOPG using the MCA . . . 116
5.9 MCA spectra dependence on DAC values . . . 117
5.10 Image of MCA signals from the detector plane . . . 118
5.11 Spectra of HOPG using the RFA with a 3 mm aperture . . . 119
5.12 Spectra of HOPG using the RFA with a 1 mm aperture . . . 120
5.13 Spectra of HOPG using the RFA with a 1 mm aperture . . . 121
5.14 Spectra of HOPG using the RFA with a 1 mm aperture . . . 122
5.15 Electron reflectivity image using the MCA . . . 124
5.16 SPELS image using the MCA . . . 125
5.17 SPELS Spectra . . . 126
5.18 STM image of Ag lines at HOPG step edges . . . 128
5.19 Electron reflectivity image of 200 nm Ag squares on HOPG . . . 129
5.20 SEM and electron reflectivity image of Ag structures . . . 130
5.21 Electron reflectivity image of Ag structures with line profiles . . . 132
5.22 Electron reflectivity image using the RFA . . . 133
5.23 Electron reflectivity image using the RFA . . . 134
5.24 Electron reflectivity image using the RFA . . . 135
5.25 Profiles at island edge . . . 136
5.26 Profiles at island edge . . . 137
5.27 Electron reflectivity image with line profile . . . 140
5.28 Images from Xu *et al.* (2014) . . . 141
5.29 Spectra of Ag on HOPG to test nonlinear field dependence . . . 143

6.1 Images from Assa'd and Gomati (1998) . . . 149

A.1 Schematic of the aperture of the evaporator . . . 153

C.1 Schematic of an AFM . . . 159
C.2 Example of the Lennard-Jones potential . . . 160
C.3 Schematic of an AFM distortion effect . . . 160
C.4 Schematic of the influence of the SEM aperture on the electron beam . . . 162

# List of Tables

1.1 Overview of the resolution for spectral imaging techniques . . . . . 33

3.1 Examples for applied CEM voltages. Typical values for HV are between 2.5 kV and 3.1 kV. . . . . 53
3.2 Summary of the influence of the etching voltage . . . . . 69

B.1 Range of DAC values and lens voltages . . . . . 155
B.2 Coefficients of the DAC conversion formula . . . . . 156

# List of Abbreviations

| | |
|---|---|
| **AES** | Auger Electron Spectroscopy |
| **AFM** | Atomic Force Microscopy |
| **CEM** | Channel Electron Multiplier |
| **CNT** | Carbon Nanotubes |
| **DOS** | Density Of States |
| **EBID** | Electron Beam Induced Deposition |
| **EBL** | Electron Beam Lithography |
| **EELS** | Electron Energy Loss Spectroscopy |
| **FE** | Field Emission |
| **FEM** | Field Emission Microscope |
| **FESAM** | Field Emission Scanning Auger Microscope |
| **FIM** | Field Ion Microscope |
| **FWHM** | Full Width Half Maximum |
| **HOPG** | Highly Oriented Pyrolytic Graphite |
| **HREELS** | High Resolution Electron Energy Loss Spectroscopy |
| **IPA** | Isopropyl alcohol |
| **LDOS** | Local Density Of States |
| **LEED** | Low-Energy Electron Diffraction |
| **LMIS** | Liquid Metal Ion Source |
| **MCA** | Multi Channel Analyser |
| **MCP** | Multichannel Plate |
| **MIBK** | Methyl isobutyl ketone |
| **NIM** | Nuclear Instrumentation Module |
| **NIL** | Nanoimprint Lithography |
| **NSL** | Nanosphere Lithography |
| **PA** | Probing Area |
| **PEEM** | Photoemission Electron Microscopy |
| **PMMA** | Poly(methyl methacrylate) |
| **PTFE** | Polytetrafluorethylene |
| **RFA** | Retarding Field Analyser |
| **RHEED** | Reflection High-Energy Electron Diffraction |

| | |
|---|---|
| **SE** | Secondary Electron |
| **SEM** | Scanning Electron Microscopy |
| **SIMS** | Secondary Ion Mass Spectrometry |
| **SHV** | Safe High Voltage |
| **SPELS** | Scanning Probe Energy Loss Spectroscopy |
| **STEM** | Scanning Transmission Electron Microscope |
| **STM** | Scanning Tunnelling Microscope |
| **STS** | Scanning Tunnelling Spectroscopy |
| **TEM** | Transmission Electron Microscopy |
| **TSP** | Titanium Sublimation Pump |
| **UHV** | Ultra High Vacuum |
| **UPS** | Ultraviolet Photoelectron Spectroscopy |
| **XPS** | X-ray Photoelectron Spectroscopy |

# Table of Symbols

| | |
|---|---|
| Å | 1 Angstrom is $1 \cdot 10^{-10}$ m |
| $k_B$ | Boltzmann constant; $k_B = 8.617 \cdot 10^{-5}$ eV/K |
| $E_{\|\|}$ | electron energy component parallel to the axis of the RFA |
| $E_{\perp}$ | electron energy component perpendicular to the axis of the RFA |
| $E_{RF}$ | Potential of the retarding field in the RFA |
| $E$ | Total energy of the incoming electron |
| $F$ | Electric field |
| $R$ | Radius of the tip apex |
| $e$ | Elementary charge; $e = 1.602 \cdot 10^{-19}$ C |
| $j$ | Field emitted current |
| $\omega_p$ | Plasma frequency |
| $\hbar$ | Reduced Planck constant; $\hbar = 6.582 \cdot 10^{-16}$ eV/s |
| $a$ | Effective emission area |
| $\epsilon_0$ | Vacuum permittivity; $\epsilon_0 = 8.854 \cdot 10^{-12}$ F/m |
| $k$ | Field reduction factor |
| $m_e$ | Mass of an electron; $m_e = 9.109 \cdot 10^{-31}$ kg |
| $\Phi$ | Work function |

# Chapter 1

# Introduction and Background

## 1.0 Perspective

The study of surfaces has been a vibrant physical research field for several decades, driven by the invention of superior analysis methods and by the importance of surfaces in various disciplines (e.g. chemistry and biology) and engineering fields (e.g. electronics). The development of experimental techniques in surface physics led to the first imaging of single atoms through the field ion microscope (FIM) and then scanning tunnelling microscope (STM), as well as to the ability to characterise the chemical and elemental composition of a surface [1–3].

The composition and structure of surfaces can have an important influence on the chemical, electrical and optical properties of a surface. A brief introduction to these fields is given in Section 1.1.

The ultimate purpose of the present research work is to develop a relatively new analysis technique, scanning probe energy loss spectroscopy (SPELS), into a practical method for nanoscale surface analysis. This technique combines the advantages of two existing analysis methods, STM and electron energy loss spectroscopy (EELS), in order to provide, with nanoscale spatial resolution, information about the chemical composition of a sample surface through spectroscopic information. This technique

has been a subject of investigation for twenty years, initially at Cambridge and then at the Nanoscale Physics Research Laboratory at the University of Birmingham. The current apparatus is Mark IV in the development of this program. The technique has been proved suitable to distinguish different materials on a surface by their surface plasmon energies, with a spatial resolution below 50 nm [4, 5], as well as to measure local secondary electron spectra [6]. SPELS employs an STM tip, operated in the field emission (FE) mode near the surface. The electrons reaching the sample are detected as a current to run a feedback loop for a measurement in constant current mode. Simultaneously, the backscattered electrons are detected by an electron energy analyser to provide an electron energy loss spectrum. The intense electric field between tip and sample acts rather like a focussing lens for the SPELS image, by suppressing most of the backscattered electrons whilst only allowing electrons from a certain area to reach the detector. The detector is positioned at a small angle to the surface as many electrons are bent back into trajectories almost parallel to the surface [7]. The objectives of this study were to perform spatially resolved plasmon images of nanostructures at enhanced signal to noise ratios, to increase the resolution limits of the instrument and to conceive and build reliable methods to support its operation. The SPELS idea is described in more detail in Section 1.4 after the underlying STM technique and FE method are explained in Sections 1.2 and 1.3.

A wide range of existing surface analysis techniques allow a thorough investigation of the atomic and molecular structure of the interface. The analysis method should be selected depending on the sample and the objective in mind. While some techniques allow the characterisation of the chemical composition of the sample but have limited spatial resolution, other techniques are able to provide topographic information with atomic resolution but fail to identify the chemical nature of the features they image. Chapter 1.5 provides a brief overview of common analysis techniques for elemental

imaging and compares them to SPELS.

## 1.1 Surfaces on the Sub-100 nm Scale

This section provides a brief introduction about techniques producing sub-100 nm structures at surfaces as well as applications of these structures to motivate the need for analysis instruments working at this resolution, such as SPELS.

In the last few decades new methods of producing structures smaller than 100 nm have been developed. For instance, the semiconductor chip industry pushed the barrier for the half pitch of a DRAM cell down to 90 nm in 2004 and has reached 22 nm since then [8]. The method with the highest precision to produce a nanostructure is the manipulation of single atoms using a STM, although this is a time consuming approach with a low throughput [9]. Size selected clusters on surfaces and self assembled layers of molecules also allow sub-100 nm structures to be obtained [10, 11]. A challenge for surface analysis techniques is to determine these structures, which are not necessarily crystalline and also sensitive to damage caused by a probe tip or an intense beam [12, 13].

Another important example of sub-100 nm structures are fullerenes [14] and carbon nanotubes (CNT) [15]. Both are allotropes of carbon and represent stable three dimensional structures in the sub nanometre regime. CNT are already used to improve properties of products like resins or composite materials [16].

## 1.2 Scanning Tunnelling Microscopy and Scanning Tunnelling Spectroscopy

The first instrument to obtain an image with atomic resolution of a flat surface in real space was the scanning tunnelling microscope (STM) invented by G. Binnig and H. Rohrer in 1982 [2, 17, 18] . It utilises the quantum mechanical tunnelling effect, which was first described in 1928 by Gamow [19] and at the same time independently by Gurney and Condon [20, 21]. The SPELS technique utilises a STM and therefore benefits from the precision of this instrument.

In this section STM and scanning tunnelling spectroscopy (STS) are described.

### 1.2.1 Scanning Tunnelling Microscopy

The STM uses a sharp tip to probe a conductive sample with atomic resolution by applying a voltage and measuring the tunnel current between tip and sample. The sample can be a metal or a semiconductor. Ideally the tip is never in direct contact with the sample. Although in classical physics an electron cannot pass a potential barrier which exceeds its own energy, like the gap between tip and sample, one consequence of quantum mechanics is that an electron has a finite probability of passing the barrier. A schematic of an STM configuration is shown in Figure 1.1.

The STM is often used in an ultra high vacuum (UHV) environment to reduce the contamination of the sample, but it can also be used in air and even in water [22].

The physical background of this system was first described by Tersoff and Hamann [23] in 1985 based on the work of Bardeen from 1961 [24]. A schematic of the one-dimensional potential barrier is displayed in Figure 1.2. The wavefunction of a tunneling electron

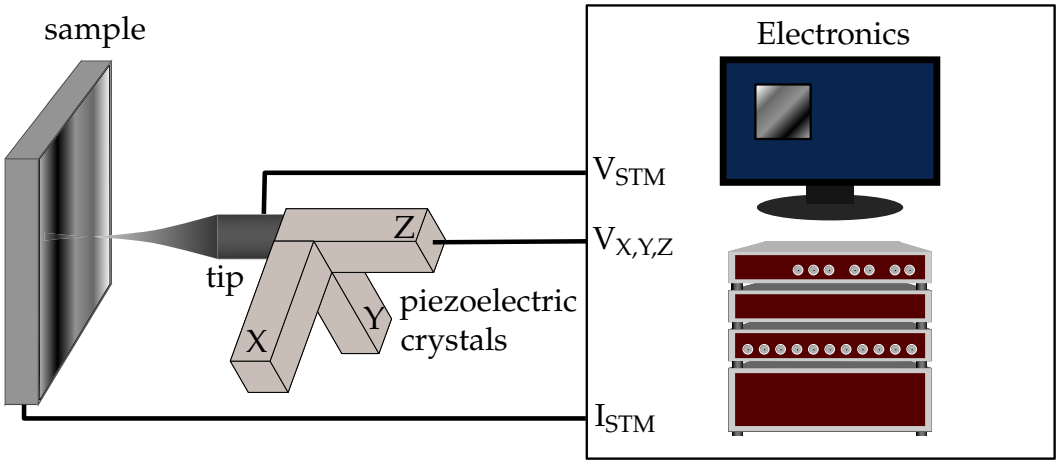


**Figure 1.1:** Schematic of a STM configuration. The electronics controls the position of the tip by adjusting the applied voltages $V_{X,Y,Z}$ at the piezoelectric crystals. The tip-sample distance is measured by the tunnel current $I_{STM}$ between tip and sample which is dependent on the applied bias $V_{STM}$.

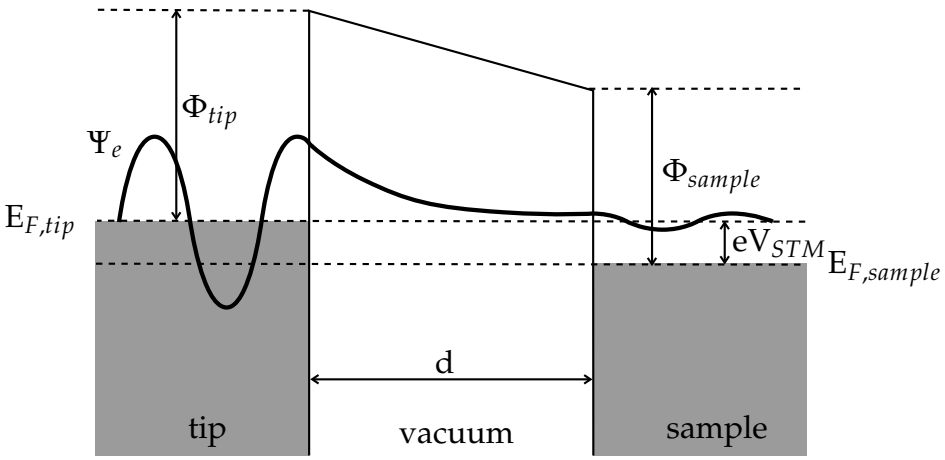


**Figure 1.2:** Energy diagram of the one-dimensional potential barrier of width d between two metal surfaces. The tip is biased ($V_{STM}$) negative with respect to the sample. The wavefunction for a tunnelling electron $\Psi_e$ is displayed as the thick black line. $\Phi_{tip}$ and $\Phi_{sample}$ are the work functions of the tip and the sample. $E_{F,tip}$ and $E_{F,sample}$ are the fermi energies of the tip and the sample.

from the Fermi level of the tip in the vacuum is

$$\Psi_e(x) \propto e^{-kx} \qquad \text{with} \qquad k = \sqrt{\frac{2m_e\Phi}{\hbar^2}} \tag{1.1}$$

where $k$ is the inverse decay length in the gap, $m_e$ is the mass of an electron, $\hbar = h/2\pi$ is the reduced Planck constant and $\Phi$ is the work function of the tip and sample ($\Phi_{tip} = \Phi_{sample} = \Phi$) [25]. Assuming a small voltage ($eV << \Phi$) and identical work functions for the tip and sample the current $I$ is proportional to

$$I \propto e^{-2kd}. \tag{1.2}$$

The STM current is proportional to the local density of states (LDOS) of the surface and depends exponentially on the distance between tip and sample and therefore can provide electronic and topographic information about the sample surface [23].

If the tip is biased negatively with regards to the sample then the measured current $I$ represents the probability of the electrons in the tip to tunnel to an empty state in the sample whilst a positive bias at the tip measures the probability of the electrons of the sample to tunnel to an empty state at the tip.

By scanning over an area of a sample with constant work function, the STM provides a topographical image of the surface. This is done either in *constant height mode* where the Z-position of the tip is held constant and the variations of the current represents the topography, or in *constant current mode* where the Z-position of the tip is dynamically adjusted to keep the current constant. The latter mode is more suitable for samples with a rough surface to avoid collisions between tip and sample.

In order to work in constant current mode it is necessary to have a feedback loop for the Z-position which reacts to changes in the tunneling current with respect to a target

current $I_{SP}$ (set point current). The coefficients of the feedback loop have to be optimised for each tip/sample configuration. The main settings for a STM measurement are these coefficients, the set point for the STM current, the applied voltage and the scan speed.

Apart from the measurement settings, another important requirement for a successful STM image is a suitable tip. Common materials for STM tips are tungsten or platinum/iridium wires. While platinum/iridium tips can be produced by simply cutting the wire, tungsten tips are produced by an electrochemical etching process, which is described in Section 3.2.

Since the typical tip-sample separation $d$ for a STM is in the range of 1 nm or less [23], the instrument uses piezoelectric crystals to move the tip and an advanced vibration damping system to prevent the tip from crashing into the sample. These techniques are described in detail in Section 2.2.

Tersoff and Hamann also published an approach to determine the theoretically effective lateral resolution of the STM [23]. They approximated the tip apex to a sphere of radius $R$. This radius, together with the tip-sample separation $d$, leads to a resolution of

$$\sqrt{A \cdot (R + d)}, \tag{1.3}$$

where $A = 2$Å and Å (Angstrom) is the unit of $1 \cdot 10^{-10}$ m.

For rough sample surfaces the geometry of tip and sample can limit the lateral resolution. This is shown in Figure 1.3. If the size of the surface features is in the same range as the tip apex diameter then the resulting image will be distorted by what is known as tip dilation. In this case, steep flanks are smoothed. While small islands appear larger, holes are smaller in the image and the depth of narrow holes could be underestimated as shown in Figure 1.3 b).

To reduce this geometrical source of distortion, it is preferable to have a sharp tip with

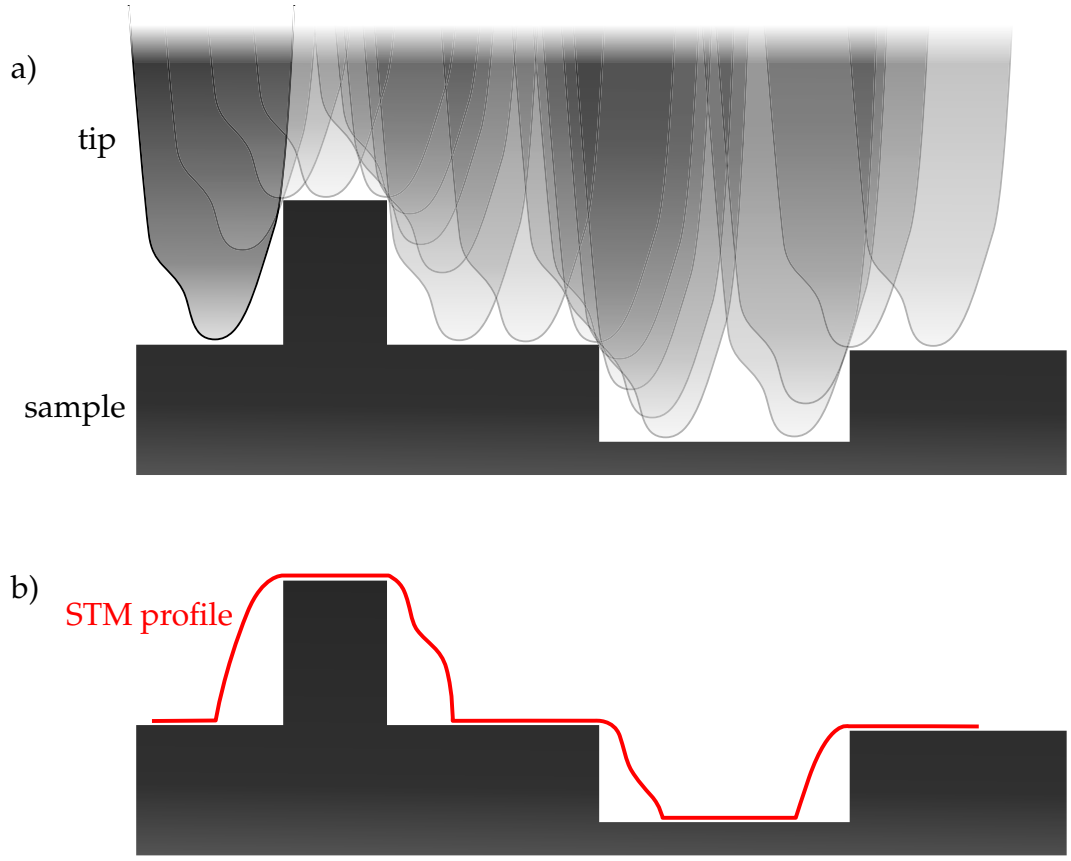


**Figure 1.3:** Schematic illustration of the distortion effect due to the tip geometry. The movement of the tip over the sample is displayed in (a) while (b) shows the expected STM profile (illustration takes only geometry into account). Note that islands appear wider while the width of a trench or a pit is underestimated.

a high aspect ratio. However, a narrow tip is also less rigid and therefore less stable during the scan. The optimal tip shape is a trade-off between resolution and stability and depends on the sample roughness and the quality of the damping system of the STM.

### 1.2.2 Scanning Tunnelling Spectroscopy

The STM enables the acquisition of spectroscopic information by changing the voltage applied between tip and sample. This method, known as scanning tunnelling spec-

troscopy (STS), measures the probability of the electrons to tunnel through the gap between the tip and the sample. This probability is dependent on the energy of one electrode (tip) with respect to the other (sample). It can be adjusted by changing the applied voltage, and the number of occupied energy states in the tip and the sample. Therefore, the current is dependent on the LDOS of the surface and the density of states (DOS) of the tip [23].

The electrons tunnel from the negative to the positive biased part of the junction. At the negative electrode, the occupied electron states with the highest energy, which are at the Fermi level, have the highest influence on the tunnel current because these electrons have the highest probability to tunnel through the gap. To help remove the influence of the DOS of the tip, the applied voltage should be negative at the tip. Then the current variations, while changing the applied bias, are mainly influenced by the unoccupied states at the sample [23, 26]. If the DOS of the tip is known then it is possible to measure the LDOS of the sample. The DOS of a tungsten tip can be manipulated to be comparable to the DOS of a free electron gas by the method described in [27]. There the tip apex is first melted by a FE current of a few microampere until it recrystallizes to a blunt tip.

For the STS measurement the applied voltage is varied while the current is recorded and the height of the tip is held constant. The voltage is limited by the work function of the positive biased part of the barrier gap. If the energy of the electrons at the Fermi level of the negative biased part exceeds the work function of the positive biased part, field emission appears. Field emission is described in the next section. The resolution for the measurement of the LDOS decreases with higher temperatures $T$ as the Fermi function changes from a step function to a distribution of width $2k_BT$ with the Boltzmann constant $k_B$.

## 1.3 Field Emission

Field emission (FE) describes the escape of electrons from a surface by tunneling through the potential barrier of the surface under the presence of an electrostatic field into vacuum. The strength of the field $F$ is in the order of 0.3-0.7 V/Å [28]. The field reduces the barrier width and therefore increases the probability of an electron to tunnel through the barrier. The emitted electrons are accelerated by the field after they have escaped from the metal.

The form of the potential barrier in one dimension can be approximated by the potential of a constant electric field $-eFx$ and by the Coulomb interaction of an electron outside of the metal with the metal surface $-e^2/(4\pi\epsilon_0 x)$ by

$$V(x) = -\frac{1}{4\pi\epsilon_0}\frac{e^2}{x} - eFx, \tag{1.4}$$

where $\epsilon_0$ is the vacuum permittivity and $e$ is the electronic charge. The maximum of the barrier is

$$V_{max} = -\frac{2}{\sqrt{4\pi\epsilon_0}\sqrt{e^3F}} \qquad at \qquad x = \sqrt{\frac{1}{4\pi\epsilon_0}\frac{e}{F}}. \tag{1.5}$$

The form of the barrier is displayed in Figure 1.4.

In 1928 Fowler and Nordheim introduced a theory of the field emitted current density [29]. Their theory was based on a one dimensional approach by assuming a flat tunnel junction. This approach was used by Young in 1959 while taking the total energy distribution of the incident electrons into account [30]. He started by deriving formulae for the number of incident electrons at the surface $N(W, E)$ and for the probability of these electrons to penetrate the potential wall $D(W)$. $N(W, E)\,\mathrm{d}W\mathrm{d}E$ is the number of electrons arriving at the surface with an energy within $E$ and $E + \mathrm{d}E$ and an energy part normal to the surface which lies between $W$ and $W + \mathrm{d}W$ per unit time. The total

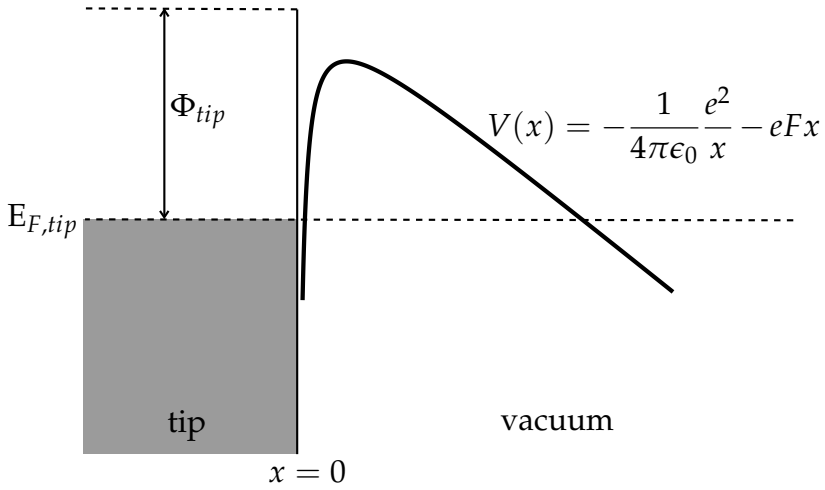


**Figure 1.4:** Schematic of the potential barrier at a metal surface under the presence of a electric field $F$. For the $V(x)$ plot an electric field of $0.5\,\mathrm{V/Å}$ is used.

energy distribution is

$$P(E)\,\mathrm{d}(E) = \int_W N(W,E)D(W)\,\mathrm{d}W\mathrm{d}E \tag{1.6}$$

and the field emitted current density $j$ is then

$$j = e\int_E P(E)\,\mathrm{d}(E) = e\int_E\int_W N(W,E)D(W)\,\mathrm{d}W\mathrm{d}E. \tag{1.7}$$

The number of incident electrons can be written as

$$N(W,E)\mathrm{d}W\mathrm{d}E = -\frac{4\pi m}{h^3}\frac{\mathrm{d}W\mathrm{d}E}{\exp\left((E-\Phi)/k_BT\right)+1} \tag{1.8}$$

while the transmission coefficient for electrons with energies near $W = -\Phi$ is

$$D(W) = \exp\left(-c + \frac{W+\Phi}{d}\right) \tag{1.9}$$

with

$$c = \frac{4\sqrt{2m_e\Phi^3}}{3\hbar eF} v\left(\frac{\sqrt{e^3F}}{\Phi}\right), \tag{1.10}$$

$$d = \frac{\hbar eF}{2\sqrt{2m_e\Phi}t\left(\frac{\sqrt{e^3F}}{\Phi}\right)}, \tag{1.11}$$

$$t(y) = v(y) - \frac{2}{3}y\frac{\mathrm{d}v(y)}{\mathrm{d}y}, \tag{1.12}$$

$$v(y) = \frac{1}{\sqrt{2}}\sqrt{1+\sqrt{1-y^2}}\left(E(b) - \left(1-\sqrt{1-y^2}\right)K(b)\right), \tag{1.13}$$

$$b^2 = \frac{2\sqrt{1-y^2}}{1+\sqrt{1-y^2}}, \tag{1.14}$$

$$E(b) = \int_0^{\pi/2} \sqrt{1-b^2\sin^2\phi}\,\mathrm{d}\phi, \tag{1.15}$$

$$K(b) = \int_0^{\pi/2} \frac{\mathrm{d}\phi}{\sqrt{1-b^2\sin^2\phi}} \tag{1.16}$$

where $t(y)$ and $v(y)$ are slowly varying functions [31]. Substituting in Equations (1.8) and (1.9), Equation (1.7) can be written explicitly as

$$j = \frac{e^3F^2}{8\pi h\Phi t^2(\sqrt{e^3F}/\Phi)} \exp\left[-\frac{4\kappa\Phi^{\frac{3}{2}}}{3eF}v(\sqrt{e^3F}/\Phi)\right] \frac{\pi\frac{k_BT}{d}}{\sin\left(\pi\frac{k_BT}{d}\right)} \tag{1.17}$$

where $\Phi$ is the work function, $\kappa = \sqrt{2m_e/\hbar^2}$ a constant, $e$ the elementary charge and $F$ the field strength [30]. Equation (1.17) is only valid where $k_BT < d$. If numerical values are inserted in Equation (1.17), $\Phi$ is expressed in eV and $F$ in V/cm and $j$ becomes

$$j = 1.03\frac{1.54\cdot10^{-6}F^2}{\phi t^2\left(3.79\cdot10^{-4}\sqrt{F}/\Phi\right)} \exp\left(-6.83\cdot10^7\frac{\Phi^{\frac{3}{2}}}{F}v\left(3.79\cdot10^{-4}\sqrt{F}/\Phi\right)\right) \tag{1.18}$$

at room temperature [31]. Equation (1.18) is sufficient for tips made of chemically etched

tungsten wires and the emission currents which are used in SPELS [32, 33].

By neglecting the slowly varying functions $t(y)$ and $v(y)$ and looking at the $F$-dependency of $j$ in Equation (1.18) it can easily be derived that

$$j \propto F^2 \cdot e^{\frac{1}{F}}. \tag{1.19}$$

The field at a tip apex depends on the applied voltage $V$, the radius of the apex, and a field reduction factor $k$ which takes the geometry of the tip into account such as

$$F = \frac{V}{kR}. \tag{1.20}$$

By multiplying $j$ with the effective emission area, $a$, the result is the generated current of the tip $I = a \cdot j$. If the measured FE current, $I$, is plotted against the applied voltage squared ($V^2$) a straight line with intercept $\alpha$ and slope $\beta$,

$$\ln\left(\frac{I}{V^2}\right) = \alpha + \frac{\beta}{V} \tag{1.21}$$

is obtained. This plot is called the Fowler-Nordheim plot and can be used to gain a rough approximation of the tip apex radius. By comparison of Equation (1.21) with (1.18) and $v$ set to 1 the slope $\beta$ is

$$\beta = -6.83 \cdot 10^7 \Phi^{\frac{3}{2}} kR. \tag{1.22}$$

If the effective work function and the field reduction factor of the tip are known the tip apex radius $R$ can be calculated from Equation (1.22).

## 1.4 Scanning Probe Energy Loss Spectroscopy

The scanning probe energy loss spectroscopy (SPELS) technique utilises an STM in field emission mode above a sample and records electron energy loss spectra from backscattered electrons. A schematic of the setup is shown in Figure 1.5. The applied voltage which extracts the electrons minus the work function of the tip defines the energy of the electrons which hit the sample. These electrons scatter inelastically in the

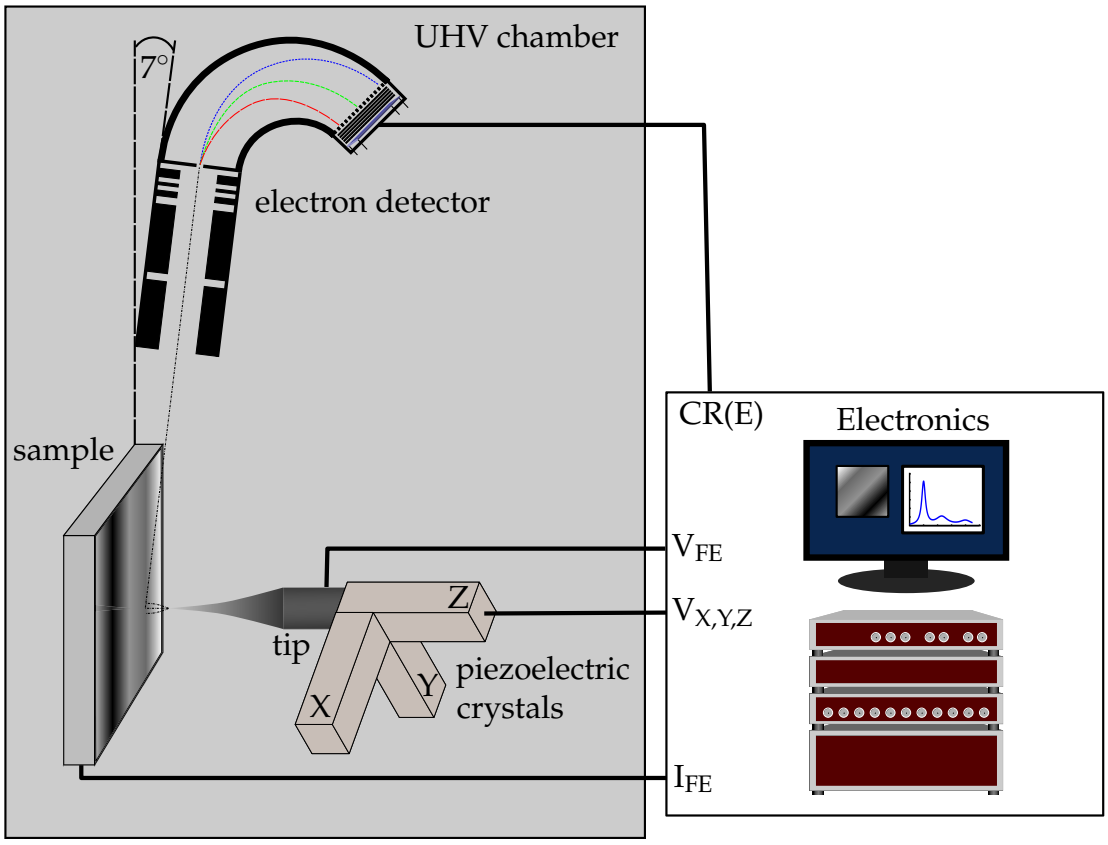


**Figure 1.5:** Schematic of the SPELS instrument as it is used in this thesis (not to scale), showing the STM in field emission mode and electron detector. The dotted lines illustrate electron trajectories. CR(E) is the measured count rate in respect of the electron energy.

material and are detected after they leave the sample. The energy loss of an electron corresponds to one or more excitations in the sample. The resulting spectrum is usually

displayed as an energy loss spectrum with the peak of elastically scattered electrons on the left and peaks of inelastically scattered electrons which lost energy to the sample on the right (see Figure 1.6).

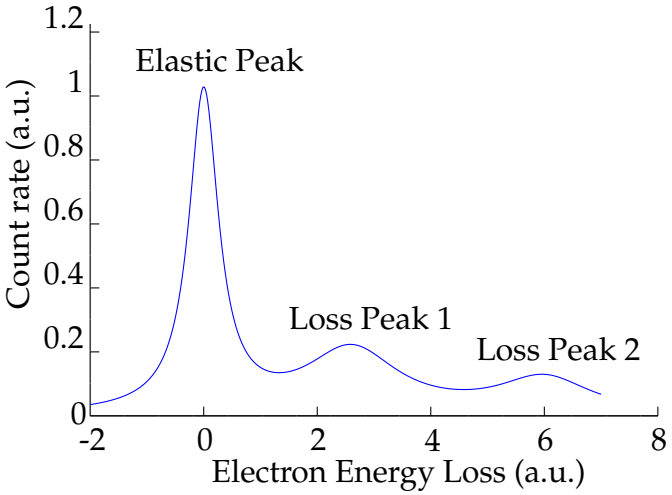


**Figure 1.6:** Example of an expected energy loss spectrum with the elastic peak at 0 and excitation peaks at 2.6 and 6 (a.u.).

The backscattered electrons are influenced by the same field by bending their trajectories back towards the sample. The majority of the electrons are absorbed by the sample and form a current which depends on the tip-sample separation and can be used in a feedback loop to adjust the Z-position of the tip, as it is performed in the tunnelling regime for a constant current measurement. Here this current is referred to as FE-current which is explained in the previous section. The area of the sample surface which is exposed to the electron beam is in the same range as the tip-sample separation [4]. This leads to a good spatial resolution for tip-sample separations in the nanometre regime. Also the field improves the spatial resolution, as described below.

A brief overview about related work is given in the next subsection. After this the previous work on SPELS in Birmingham is explained. A more detailed view of electron scattering in the sample is given at the end of this section.

### 1.4.1 Historical background

The first attempt to use field emitted electrons from a tip to measure surface properties of a sample was performed by Young in 1972 [34]. He called his instrument the Topografiner and achieved a spatial resolution of 400 nm by measuring the secondary electrons from the sample. It was the precursor to the STM. Young achieved a count rate of 1 kHz by using an emitter voltage of 160 V. This work was improved by Fink in 1988 [35]. He obtained a spatial resolution of 3 nm with an STM operating at 15 V and an FE-current of 0.1 nA.

The next step was to perform an energy-resolved measurement of the backscattered electrons, which was done by Reihl and Gimzewski in 1987 [36]. Their instrument was called the field emission scanning auger microscope (FESAM) and allowed them to measure surface and bulk plasmons of a silicon surface at an initial electron energy of 574 eV and Auger electrons at 1050 eV. The tip-sample separation during the experiment was 100 µm and above. In 1988 Allenspach and Bischof added a Mott detector to a STM and used the tip in FE mode to measure magnetic domains on the sample [37]. Their detector was set up at an angle of 25° to the surface. Tomitori *et al.* combined a field emission microscope (FEM) and a FIM with a STM in FE mode and an electron energy analyser which was set up at an angle of 20° to the surface [38, 39]. They studied the influence of the tip-sample separation on the obtained spectra in the range of 0.1-3 mm and found decreasing count rates for energy loss peaks for lower voltages and therefore smaller tip-sample separations. They tried to reduce the effect of the field between tip and sample by introducing a grounded molybdenum shield around the tip which led to the disappearance of a broad peak at lower energies in their spectra. Recently Xu *et al.* used a toroidal electron energy analyser with an azimuth angular range of 245° to measure the energy of backscattered electrons field emitted from a tungsten tip which is mounted onto Omicron micro piezo slides [40]. They achieved an image of energy

loss spectra with a spatial resolution of 4.8±2.4 μm.

### 1.4.2 Previous work at NPRL

The work presented here builds upon previous research conducted at the Nanoscale Physics Research Laboratory (NPRL) at the University of Birmingham, which will be summarised in this section.

In 2000 Eves *et al.* reported spectra from backscattered electrons from a silicon sample for different angles between the detector and the sample [7]. They used a hemispherical electron energy analyser. The spectra for detector angles of 0°, -0.8° and 1.4° are shown in Figure 1.7. This experiment demonstrated that the highest count rate of backscattered

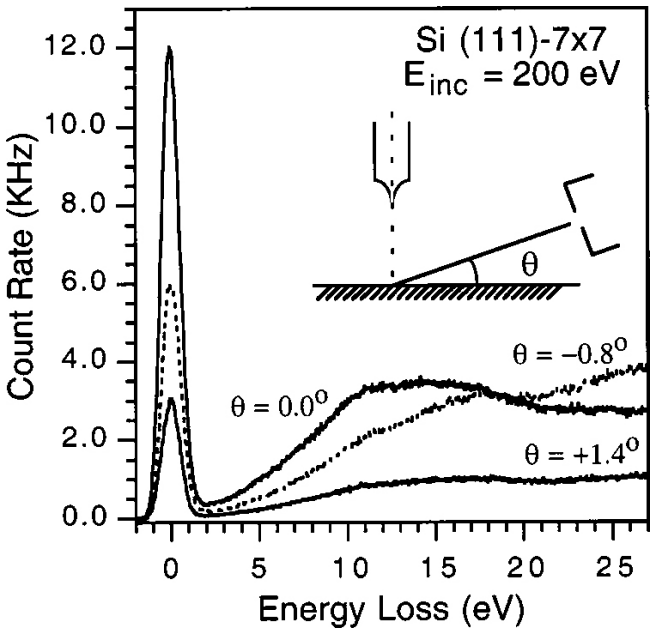


**Figure 1.7:** Electron energy loss spectra obtained on a Si(111)-7×7 sample for different angles between detector and sample. The incident electron energy was 200 eV and the FE-current was 20 nA (from [7]).

electrons can be obtained by a detector set up parallel to the surface of the sample. In the same year Festy *et al.* discussed the influence of the surface topography on the obtained SPELS images [41]. They reported a spatial resolution of 40 nm by collecting

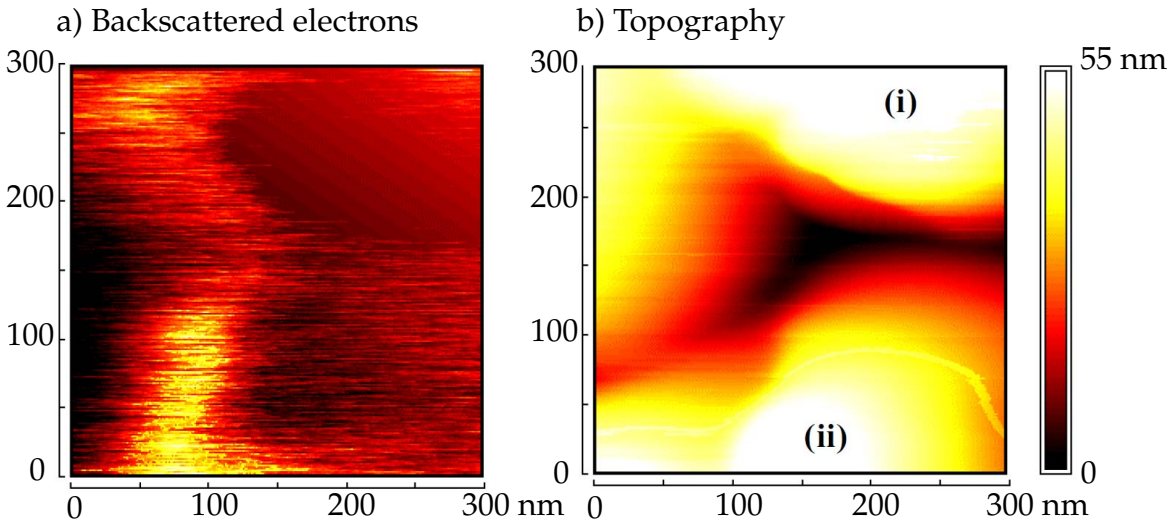


**Figure 1.8:** Backscattered electron image (a) and topography image (b) of a roughened Si(111) sample. The detector is positioned at the left side of the image. The applied voltage was 120 V and the FE-current was 20 nA. Only the edges facing the detector appear bright in the backscattered electron image (from [41]).

backscattered electrons with one energy whilst the tip scanned over the sample. In Figure 1.8 the topography and the backscattered electron image of a roughened Si(111) surface are displayed. The highest count rate of backscattered electrons was detected at the edges of islands facing the detector. The underlying mechanism is comparable to SEM images and is shown in Figure 1.9. The difference to the contrast mechanism in SEM is that the high electric field in SPELS suppresses most of the electrons on the edge opposite to the detector as these electrons are suppressed by the field under the tip. If the feature size on the sample is in the range of the tip-sample separation electrons can be blocked by these features. This blocking effect is displayed in Figure 1.10 where the lower part of an edge facing the detector does not produce a high count rate due to the blocking of these electrons at the next high feature.

An analysis of the trajectories of the backscattered electrons was published by Palmer *et al.* in 2002 [4]. The results are shown in Figure 1.11. The first important information from

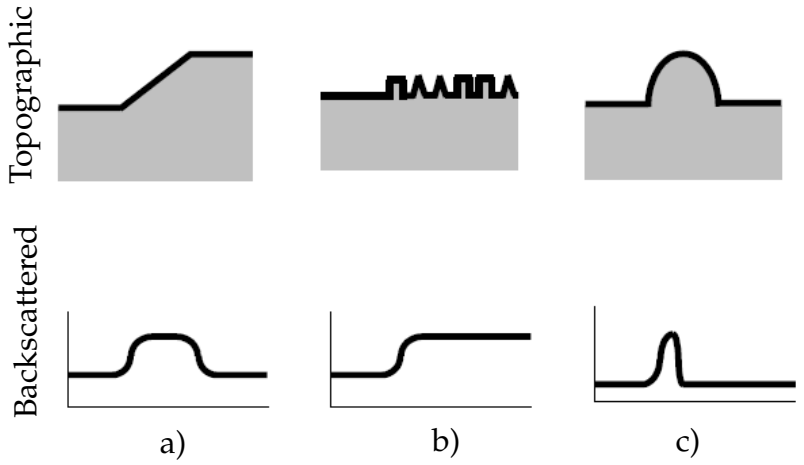


**Figure 1.9:** Image contrast in the image for backscattered electrons for three different surface features. The detector is assumed to be on the left. The features are a surface edge facing the detector in (a), a series of small particles below the resolution of the instrument in (b) and a big particle in (c) (from [41]).

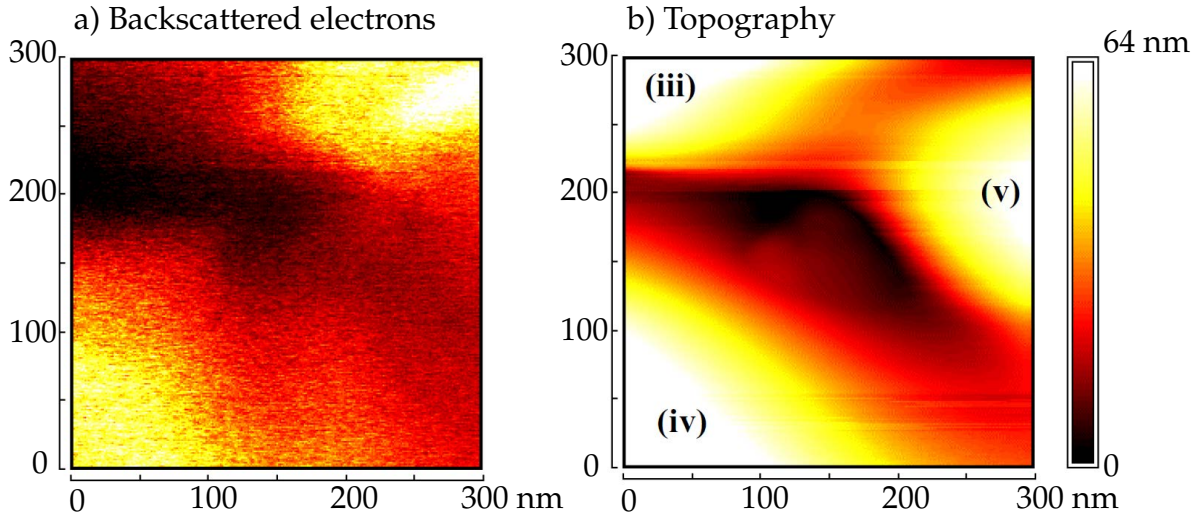


**Figure 1.10:** Backscattered electron image (a) and topography image (b) of a roughened Si(111) sample. The detector is positioned at the left side of the image. The applied voltage was 120 V and the FE-current was 20 nA. The electrons from the lower part of the left edge of island (v) are blocked by island (iv) (from [41]).

this simulation is that the area illuminated by the electron beam is in the range of the tip-sample separation, as mentioned before. In the calculations a tip-sample separation of

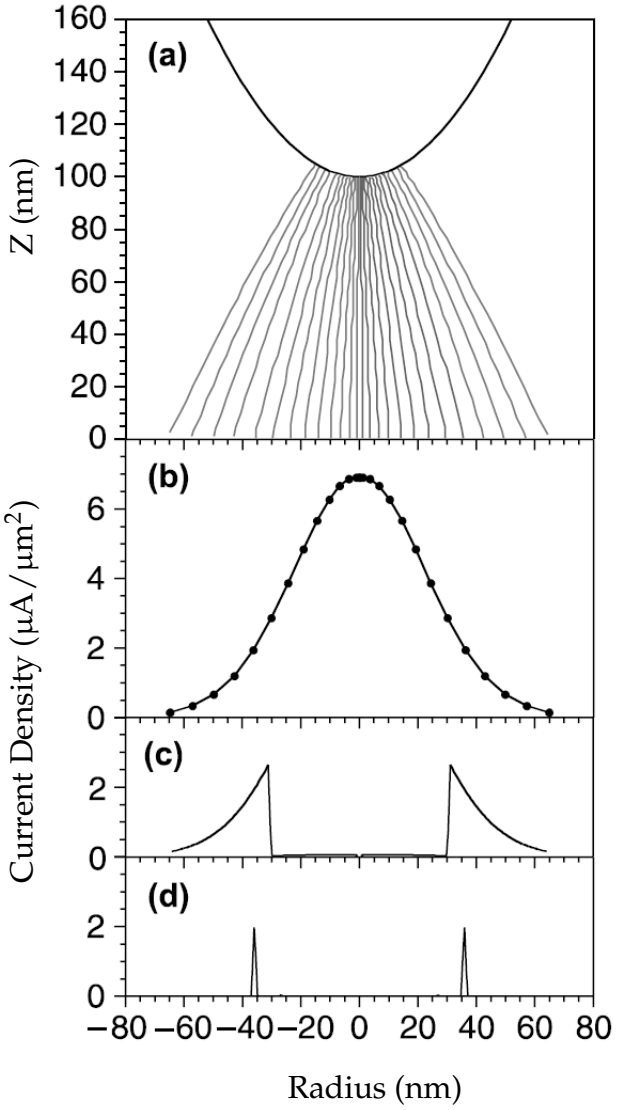


**Figure 1.11:** Simulated electron trajectories of field emitted electrons from a tip with an apex radius of 28 nm, 100 nm above a surface and an applied voltage of 100 V at 1.16 nA FE-current are shown in (a). The upper region of the tip is assumed to be shielded as the long range field effects are neglected in this simulation. In (b) the current density of incident electrons is displayed. (c) shows the backscattered electrons which reach the detector during a angle-integrated measurement. In (d) the measured distribution of electrons reaching a detector at an angle of $85 \pm 0.5^{\circ}$ is displayed (from [4]).

100 nm leads to a electron beam distribution with a full width half maximum (FWHM) of 54 nm. The second important fact is that most of the electrons which are backscattered do not reach the detector. Only the electrons from a narrow annulus around the tip position can escape and be detected. This selection process increases the resolution achievable with SPELS. For an integrated electron measurement the FWHM of the distribution of the detected electrons is 10 nm. If the measurement is taken at a fixed angle of $85 \pm 0.5^{\circ}$ simulations demonstrate that the FWHM of the electron distribution is only 1.3 nm. In calculating this value it is assumed that the upper parts of the tip are shielded as the influence of the long range electric field is neglected.

In 2004 Festy and Palmer demonstrated that an energy-resolved image of the backscattered electrons with a spatial resolution of at least 50 nm is possible [5]. This image was obtained by recording spectra on each point of a $10 \times 10$ grid on a $500 \times 500\,\mathrm{nm}^2$ area with a retarding field analyser. The sample they used was a roughened silicon sample. Yin *et al.* reported energy loss spectra obtained from graphite with SPELS [42]. They could identify plasmon and secondary-electron emission peaks. The secondary electron emission peaks can be identified by changing the FE voltage and therefore the energy of the incident electrons. A secondary electron has a fixed energy and the corresponding peak in the energy loss spectra shifts as the FE voltage is changed. Lawton *et al.* extended this work by performing SPELS measurements at tip-sample distances from 50-3000 nm on graphite and gold samples [6]. They also reported the influence of carbon contamination on the spectra taken from gold samples. Pulisciano *et al.* published SPELS measurements of silver and gold samples where they could identify the surface plasmon peaks and interband transition features [43].

The goal of the work performed by Song *et al.* was to reduce the influence of the tip on the trajectories of the backscattered electrons [44, 45]. They produced a micro fabricated silicon tip coated with a co-axial layer consisting of two layers of gold which were

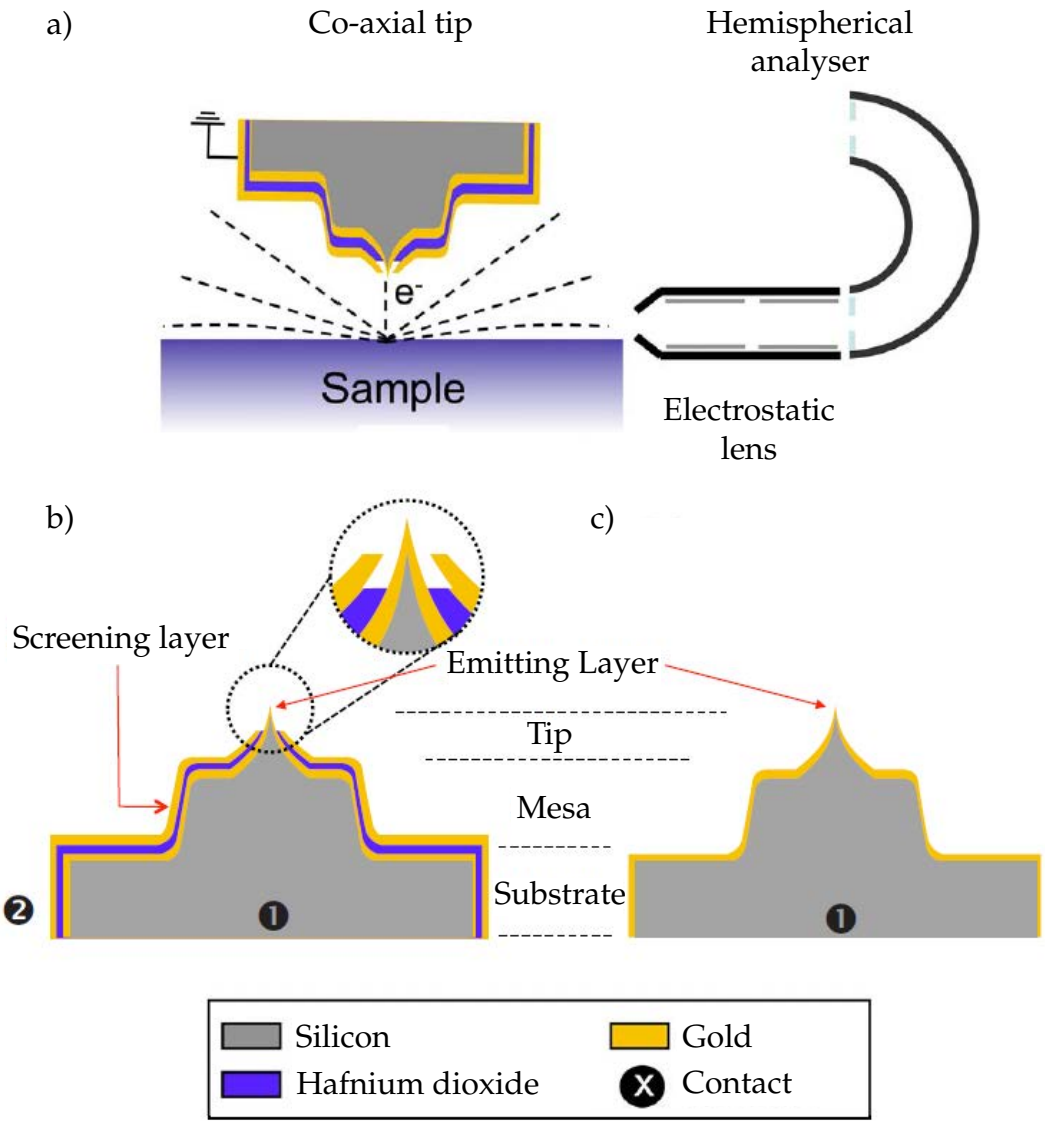


**Figure 1.12:** a) Schematic of the co-axial tip produced by Song for SPELS measurements. b) The inner gold layer forms the tip apex and is electrically isolated from the outer gold layer by a hafnium dioxide layer. c) The gold coated silicon tip without shielding (from [45]).

electrically isolated by a hafnium dioxide layer as displayed in Figure 1.12 (taken from [45]). With the co-axial tips the spectra of the backscattered electrons showed a higher signal for secondary-electron emission peaks. The confinement of the field to the tip-sample junction allowed low energy electrons and electrons which are emitted at a

shallow angle (electrons originating from the M-point of the Brillouin zone of graphite) to reach the detector.

### 1.4.3 Electron scattering

The following subsection provides the theoretical background of the electron scattering mechanism present during a SPELS measurement.

The incident electrons can undergo elastic and inelastic scattering events in the sample and at adsorbates on the sample surface. The amount of energy lost by an electron to one or more inelastic scattering events can be found by comparing the measured electron energy with the initial electron energy. This is done by recording an energy loss spectra of the backscattered electrons which also includes the peak for the elastic backscattered electrons.

The electrons scatter elastically at the ion cores of the sample. Therefore the cross section for elastic scattering is dependent on the energy and the angle of the incident electrons according to Bragg's law. If $d$ is the spacing between lattice planes and $\theta$ the angle of the incident electron beam, then the spectrum of the elastic scattered electrons has peaks at

$$E = \left( \frac{\hbar^2 \pi^2}{2 m_e d^2} n^2 - V_0 \right) \frac{1}{\cos^2 \theta} \tag{1.23}$$

with $n \in \mathbb{N}$ and $V_0$ as the real part of the inner potential of the specimen [46]. The position of the Bragg peaks provides structural information about the specimen such as the spacing between lattice planes. The wave function $\Psi_s$ of the scattered beam can be

described as

$$\Psi_s(\vec{r}) = \sum_{\vec{g}_{||}} \beta_{\vec{g}_{||}} \exp\left( i\left(\vec{k}_{||} + \vec{g}_{||}\right)\vec{r}_{||} - \underbrace{i\sqrt{\frac{2mE}{\hbar^2} - \left|\vec{k}_{||} + \vec{g}_{||}\right|^2}}_{A} \cdot z \right) \tag{1.24}$$

where $\vec{k}'_{||} = \vec{k}_{||} + \vec{g}_{||}$ is the momentum of the scattered electrons. Part $A$ is real when $|\vec{k}_{||} + \vec{g}_{||}|^2 > 2mE/\hbar^2$. Under this condition the electron wave is evanescent. By adjusting the energy of the incident electrons the momentum of the scattered electrons can be limited. Only about 0.5 % of the incident electrons in the energy range of 50-100 eV are elastically backscattered [47].

The energy dependence of the mean free path of electrons in graphite, silver and gold is presented in Figure 1.13 and was calculated in [48] using Penn's algorithm [49].

A theory for inelastic backscattered electrons was published by Saldin in 1988 [50]. He found that if the energy loss is small compared to the electron energy a two phase scattering process is more likely than a single inelastic scattering process. Most of the backscattered electrons undergo an elastic backscattering and an inelastic forward-scattering event. Therefore, two main channels for detected inelastically scattered electrons are to be considered. The electron could first be elastically scattered and thereafter lose energy to an inelastic scattering event, which is called $(D + L)$ event, or it can first lose energy and then diffraction occurs, named $(L + D)$. For small energy losses (0-35 eV) the probability for both channels were found to be equal by Ruocco *et al.* for highly oriented pyrolytic graphite (HOPG) [46]. They compared the electron energy spectra for elastic scattered electrons with those electrons which have a certain energy loss (inelastically scattered electrons). The Bragg peaks found in the spectra for elastically scattered electrons remain in the spectra for inelastically scattered electrons. Additionally, for each Bragg peak a second peak occurs at an energy which exceeds

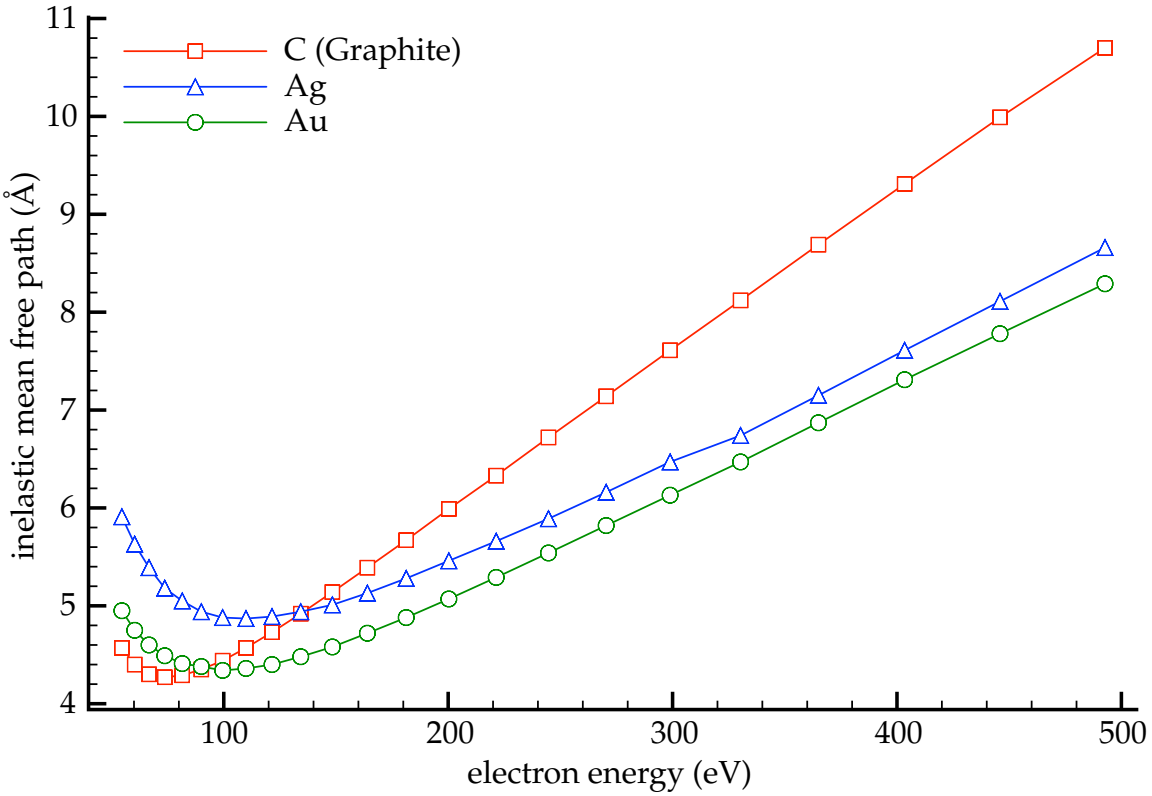


**Figure 1.13:** Electron mean free path in graphite, silver and gold in the electron energy range from 54.6 eV to 492.7 eV. This graph was plotted using values calculated by [48].

the Bragg peak by the same amount as the energy loss of the electrons. This second peak is interpreted as the $(L + D)$ channel, because the energy of these electrons is at the Bragg peak after the inelastic scattering event. The electrons at the Bragg peak are interpreted as the $(D + L)$ channel, because as their initial energy is at the Bragg peak the probability of measurement is higher when the inelastic scattering has occurred after the elastic scattering.

The incident electrons can scatter inelastically at the ion cores of the substrate which is referred to as impact scattering or it can happen as dipole scattering between the incident electron and the electron gas of the sample crystal or with dipoles from adsorbates on the sample surface.

*Dipole scattering* includes excitations of the electron gas, including plasmons, as well as *inter*- and *intra*-band transitions and changes of the rotational and vibrational states of adsorbates. The range of dipole scattering is determined by the cut-off frequency $\omega_c = v/d$, where $v$ is the velocity of the electron and $d$ is the distance between the sample surface and the electron [51]. Dipole scattering is a weak interaction resulting in only a small momentum change. Therefore the trajectory of inelastic scattered electrons which are scattered by dipole scattering and elastic backscattering is near the trajectory of only elastic backscattered electrons.

*Impact scattering* can excite phonons and Auger electrons. Auger electrons are produced when the incident electron ionizes a core electron of the atom. The new free state is refilled by an outer electron and the energy of this transition ionizes a third electron, which is called an Auger electron. The Auger electron is characteristic for the element and can be used to characterise the sample. The momentum transfer during impact scattering can be in a wide range which leads to a diversification of the trajectories of the scattered electrons.

*Resonance scattering* leads to enhanced scattering cross sections at certain electron energies due to the temporary formation of negative ions. The negative ion resonance occurs when an electron attaches to an adsorbed molecule at the sample surface [52]. The excited ion emits an electron after the resonance lifetime $\tau$. The energy of this electron is determined by the energy difference between the excited state of the ion and the state of the molecule after electron emission, which can be a vibrationally excited state [53].

In the energy range for SPELS at 30-200 eV the energy loss spectra are determined mainly by surface and bulk plasmons and interband transitions which are dipole scattering events. The plasmon frequency can be derived from the dielectric function $\xi(\omega, k)$ at $k = 0$ assuming a free electron gas model. A free electron in a field $E$ has the equation

of motion

$$m\frac{\mathrm{d}^2x}{\mathrm{d}t^2} = -eE \tag{1.25}$$

and with $x, E \propto e^{iwt}$ inserted in (1.25) it is

$$x = \frac{eE}{m\omega^2}. \tag{1.26}$$

Here, the polarisation $P$ is the dipole concentration multiplied by the dipole moment of one electron. Using Equation (1.26) and the electron density $n$, it can be written as

$$P(\omega) = -nex = -\frac{ne^2}{m\omega^2}E. \tag{1.27}$$

The dielectric function at $k = 0$ is then

$$\xi(\omega, 0) = 1 + \frac{P(\omega)}{\epsilon_0 E} = 1 - \frac{ne^2}{\epsilon_0 m\omega^2} = 1 - \left(\frac{\omega_p}{\omega}\right)^2 \tag{1.28}$$

with the plasma frequency

$$\omega_p = \sqrt{\frac{ne^2}{\epsilon_0 m}}. \tag{1.29}$$

The dielectric theory predicts the occurrence of a bulk plasmon at $\Re(\xi) = 0$ which corresponds to a frequency

$$\omega_{bp} = \omega_p. \tag{1.30}$$

The surface plasmon frequency can be found at $\Re(\xi) = -1$ which is at

$$\omega_{sp} = \frac{\omega_p}{\sqrt{2}}. \tag{1.31}$$

In this derivation, the surface plasmon is assumed to be at the surface of a metal to air or vacuum with $\epsilon = 1$. Surface plasmons at a interface between two materials must

consider the dielectric functions of both materials. For metals damping effects from low energy interband transitions must also be considered [54].

In summary, it was demonstrated that SPELS can achieve a spatial resolution below 50 nm for images of energy loss spectra. The electron energy used with SPELS is in the range of about 30-200 eV. The energy resolution of the instrument depends on the energy distribution of the emitted electron, which is in the range of 0.3 eV, and on the detector resolution [55]. In the following section other techniques and their properties are compared to SPELS.

## 1.5 Existing Elemental Imaging Techniques

This section describes common surface analysis techniques which perform spatially resolved elemental analysis in order to compare them with SPELS. This includes techniques for spectral imaging which perform a spatially resolved measurement of the electron energies emitted from a surface as well as secondary ion mass spectrometry (SIMS) which images the elemental mass. There are three main groups of instruments which can identify the composition of a sample on a small scale: those which use electrons to probe the surface like Auger electron spectroscopy (AES) and EELS; those which use photons like photoemission electron microscopy (PEEM), X-ray photoelectron spectroscopy (XPS) and ultraviolet photoelectron spectroscopy (UPS); and those which use ions like SIMS.

For heterogeneous samples, like nanostructures, the imaging resolution of the technique is an important factor. In general the resolution can be split into a lateral part, which describes the distinguishability of two features parallel to the surface, and a vertical part, which describes the distinguishability of two features orthogonal to the surface. Vertical resolution can be particularly useful for multi layered surfaces as then the signal can be

assigned to only one layer. This type of sample can also be analysed with techniques with a high surface sensitivity where only the first layer at the surface is measured.

Operation under a vacuum is essential for all the following techniques in order to avoid surface contamination. For techniques based on electrons as a probe, an UHV chamber is needed to increase the mean free path of electrons between sample and detector.

### 1.5.1 AES

AES relies on the Auger-Meitner effect, discovered independently by Pierre Auger and Lise Meitner [56, 57], which is based on the emission of an electron which gains its energy from an *inter*- (for a Coster-Kronig transition) or *intra*-band transition in the same excited atom. These Auger electrons can be used to identify the elemental composition of the sample [58–60]. To excite the atoms, AES uses electrons with energies in the range of several eV to several keV [61–63]. Newer methods use synchrotron radiation as an electron source [60]. The spectra of the emitted electrons is then measured.

The resolution for AES is determined by the electron beam width and electron energy and can reach the nanometre regime [64].

### 1.5.2 EELS

EELS is, like SPELS, a method which measures the energy loss of electrons in a sample to obtain information about surface excitations of a sample. These excitations include surface and bulk plasmons, *inter*- and *intra*-band transitions, phonons, surface state transitions, Auger transitions and rotational and vibrational states of absorbed molecules. The difference to SPELS is that the electron beam is generated and focussed in an electron gun and hits the sample in a field free space. Thus, the backscattered electrons are not influenced by any field and the lateral resolution is only determined by the width of

the electron beam. Another difference is the range of electron energies which is in the range of a few to several hundred keV. The surface sensitivity decreases with higher electron energies as this increases the mean free path of the electrons in the sample. EELS is not only a surface analysis technique, but can also work in transmission with thin samples due to the higher mean free path of electrons at higher energies (see Figure 1.13).

If an EELS detector is combined with a scanning transmission electron microscope (STEM) and a monochromator, high spatial resolution (<1 nm) and energy resolution (<0.2 eV) can be achieved at an electron energy of 300 keV [65]. Only samples with a sufficient electron transparency can be used in this instrument. Common STEM samples are thinner than 100 nm.

### 1.5.3 PEEM, XPS, UPS

PEEM excites a sample by a photon beam and measures the photoemitted electrons. It is therefore based on the photoelectric effect. Incident photons with energy $E_p$ transfer this energy to electrons which travel to the surface, overcome the material's work function $\Phi$, escape with a kinetic energy $E_{kin}$ and are measured by a detector. The absolute value of the binding energy $E_b$ of the measured electrons can be calculated by

$$E_b = E_p - E_{kin} - \Phi. \tag{1.32}$$

If synchrotron light is the photon source then a wide continuous range of energies, typically from a few up to 1500 eV, can be used to probe the sample.

If the incident photons are in the X-ray regime one speaks of XPS. XPS measures the atomic binding energies of electrons and was first demonstrated by Siegbahn in 1957 [3, 66]. Other than X-ray absorption spectra it provides the absolute binding energies rather

than the differences between energy levels. As the binding energies are characteristic for each element, XPS measures the chemical composition of the sample surface. Each element with an atomic number above 2 can be detected. Hydrogen (Z = 1) and helium (Z = 2) are not directly visible due to the low cross section of their electron orbitals for photon absorption.

If the initial photon energy is in the range of ultraviolet light the method is called UPS. UPS measures valence electrons and binding properties of the sample.

The surface sensitivity of these measurements is determined by the mean free path of the electrons in the sample rather than by the much greater penetration depth of the photons. XPS has a vertical resolution of less then 2 nm while UPS has less then 1 nm due to the smaller electron energies. The lateral resolution is given by the size of the photon beam which can be lower than 150 nm [67].

The maximum energy resolution in XPS is limited by the lifetime width of the core hole produced in the photoemission process [68]. Recently Daimon *et al.* performed stereo-PEEM by using a large acceptance angle objective lens [69].

### 1.5.4 SIMS

SIMS removes surface atoms from the sample by ion bombardment [70, 71]. Most of these atoms are neutral, but those which are charged can be analysed by mass analysers like quadrupole or time of flight analysers [72, 73]. This allows a highly sensitive analysis of the elemental composition of the sample surface. The disadvantage of this method is that it erodes the sample and gives no information about electronic states.

The lateral resolution is determined by the size of the initial ion beam which can have a FWHM down to 10 nm in case of a liquid metal ion source (LMIS). However, the intensity distribution of the ion current is not a Gaussian distribution but has large

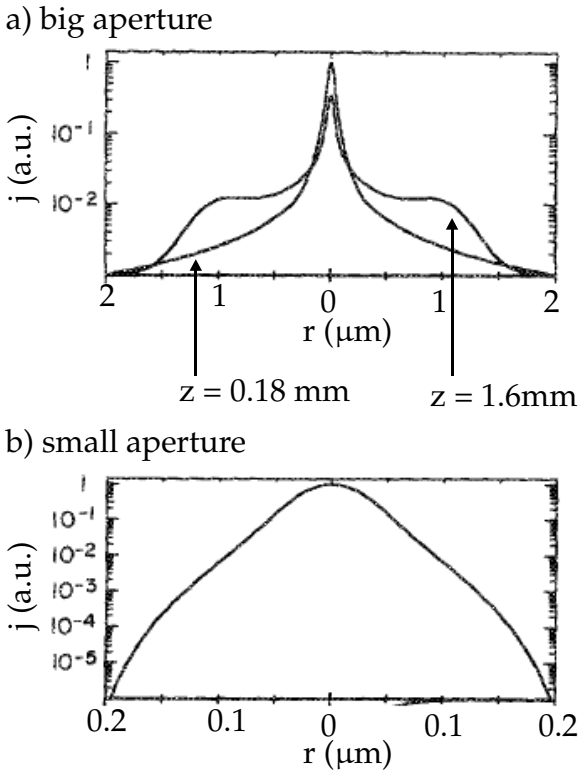


**Figure 1.14:** Profile of the ion current density j for a large (a) and small (b) aperture in the ion optics of a ion gun. In (a) the profile is displayed for two different distances z after the ion optic (taken from [74]).

tails as displayed in Figure 1.14 [74]. Note that the current density axis of this figure is exponential. The long tails reduce the lateral resolution because atoms from regions far away from the area described by the FWHM are also removed from the sample. Aberration effects can also occur in ion optics and are caused by the velocity distribution of the ions.

The surface sensitivity of the instrument is one atomic layer as for a small incident ion flux only atoms from the first layer are removed. SIMS can be used to measure a depth profile of the sample while the ion beam removes material at one site of the sample and therefore provide vertical resolution.

### 1.5.5 Summary

Table 1.1 shows a list of the previously mentioned elemental imaging techniques along with their resolutions from the most recent experiments. The resolution of 8 nm for AES

**Table 1.1:** Overview of the resolution for spectral imaging techniques.

| Technique | Lateral Resolution | Surface Sensitivity | Electron Energy $E$ |
|---|---|---|---|
| SPELS | <50 nm | first layers | 30-200 eV |
| AES [64] | 8 nm | ($E$-dependent) | 25 keV |
| STEM-EELS [65] | sub-nm | ($E$-dependent) | 300 keV |
| XPS, UPS [67] | 120 nm | <2 nm | – |
| SIMS [75] | $\leq$50 nm | first layers | – |

and sub-nm for STEM-EELS is reached only at the high electron energies of 25 keV and 300 keV stated in the table. The resolution decreases for lower energies. STEM-EELS is limited to thin samples and has therefore practically no surface sensitivity as the electrons pass through the whole sample. SPELS works at much lower electron energies of less then 200 eV and therefore damage to the sample is smaller.

The resolution in the imaging XPS and UPS measurements presented in Table 1.1 were taken at the UE-52/SGM undulator beamline at BESSY II. The Omicron Nanotechnology GmbH which distribute the NanoESCA analyser used in this experiment states a lateral resolution of 500 nm for lab experiments and 100 nm at a synchrotron.

SIMS provides a high sensitivity measurement of the elemental composition of a sample but does not provide electronic spectra. It is not comparable with the other techniques mentioned in terms of beam damage as it needs to remove the sample material in order to perform an analysis.

The advantages of SPELS are the combination of high lateral resolution and surface

sensitivity with low electron energies in a lab experiment without the need of a sophisticated electron source and the direct measurement of the topography of the sample during the experiment or directly thereafter in STM mode. This allows us to link spectral information with an atomic resolution image of the surface.

# Chapter 2

# Experimental Apparatus

## 2.0 Perspective

The SPELS system is described in this chapter as it stood in the spring of 2011 when I began this work. This instrument is referred to as the fourth generation SPELS or "mark IV SPELS" and was in large part the result of the work of James Lawton in conjunction with collaborating companies. His main aim was to provide a machine which allows routine spectral imaging through the introduction of a multi-channel electron detector.

As SPELS utilises electrons to image a sample it requires a vacuum system, which is described in the following section. The vacuum system is also necessary to avoid contamination of the sample surface and the tip. The STM scanner head is based on an Omicron[1] STM-1 system which was slightly modified to allow STM, FE and SPELS measurements. The electron energy analyser consists of an EA5000MCA multi channel analyser and electron optics from LK Technologies[2]. The sample preparation method as well as the software environment is described at the end of this chapter.

[1]Omicron NanoTechnology GmbH, Limburger Straße 75, 65232 Taunusstein, Germany, www.omicron.de
[2]LK Technologies, Inc., 1590 S. Liberty Drive, Suite A, Bloomington, Indiana , USA, www.lktech.com

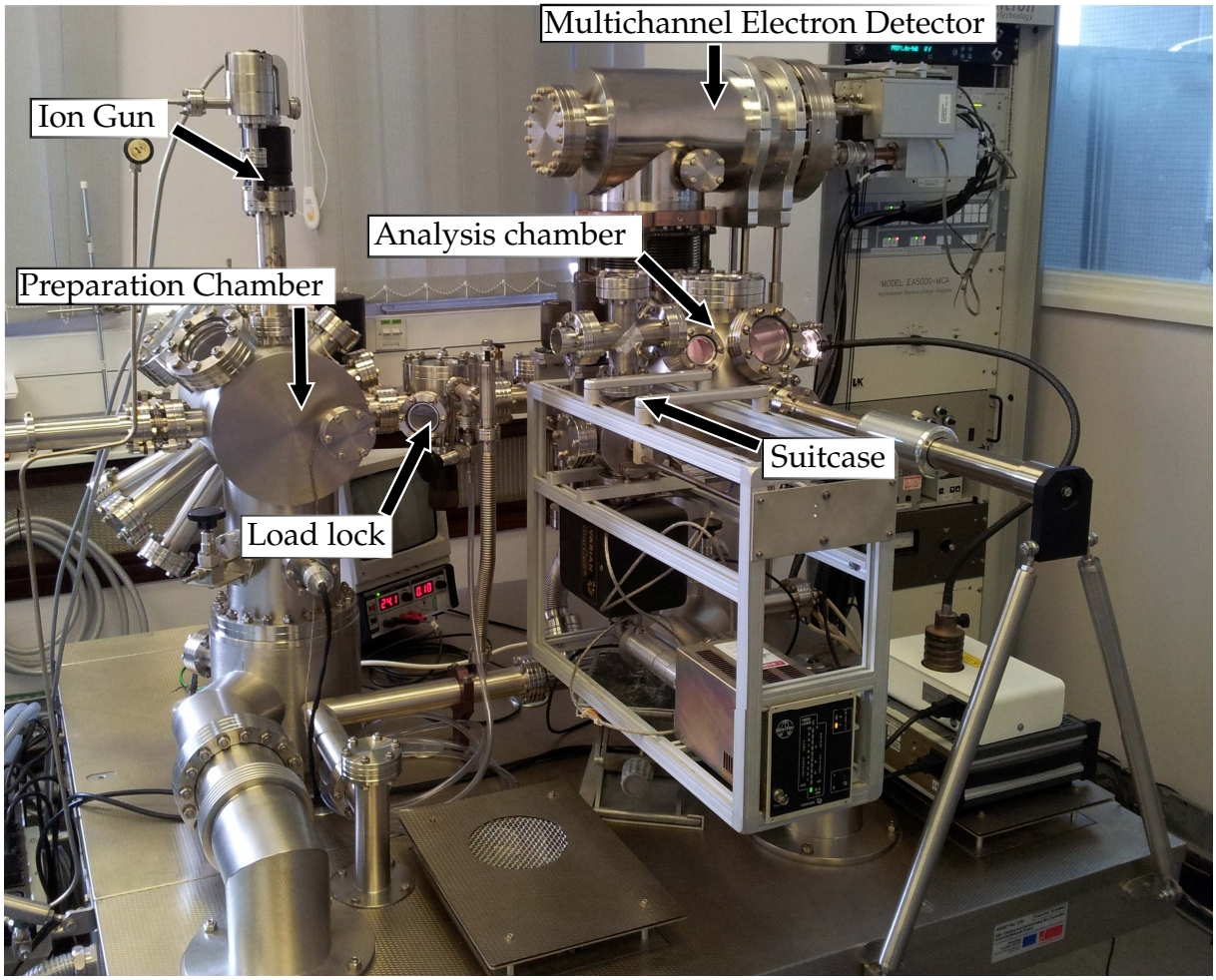


**Figure 2.1:** Image of the SPELS instrument with attached suitcase. The preparation chamber is at the left and the analysis chamber is at the right part of the image. The multichannel electron detector is raised. The metal tube partly visible at the left side contains the linear positioner to transfer between the two main chambers and the load lock.

## 2.1 Ultra High Vacuum System

Figure 2.1 shows the SPELS UHV system. The UHV system consists of a preparation chamber where tips and samples are prepared and an analysis chamber where the measurements are performed and the samples are stored. The two chambers are separated by a gate valve and samples and tips can be transferred between the two

chambers using a magnetic transfer arm. Also a small load lock chamber and an UHV suitcase are connected to the preparation chamber. The load lock chamber allows a transfer of tips and samples into and out of the vacuum into air without venting the preparation chamber. It therefore contains a venting valve. The UHV suitcase allows a transfer of samples between different UHV systems by retaining the vacuum with an ion pump. It also contains a tip holder, which allows annealing of STM tips by direct heating, and a simple evaporator which consists of a tantalum crucible heated by direct resistive heating.

The typical pressures of $3 \cdot 10^{-11}$ mbar for the analysis chamber and $5 \cdot 10^{-10}$ mbar for the preparation chamber are reached by four different types of vacuum pumps. Both chambers are in each case equipped with a turbo molecular pump which is pre-pumped by a rotary pump, an ion pump and a titanium sublimation pump (TSP). With the turbo molecular pumps the pressure can be decreased from standard pressure down to $1 \cdot 10^{-09}$ mbar. The turbo molecular pump at the analysis chamber is only used for the initial pumping and while the system is baked out. If the turbo molecular pump is not used it must be vented to prevent the chamber being polluted by oil residues in the lower parts of the pump. Therefore it can be disconnected from the main chambers. The UHV is reached and maintained by the ion pump and by the TSP. The ion gauge can be used from $1 \cdot 10^{-6}$ mbar to the low $10^{-11}$ mbar.

If a chamber was vented by air, the system has to be baked out at 150°C for about two days in order to remove the water adsorbed on the inner wall of the vacuum chambers and on the instruments. During this time only the turbo molecular pumps together with the rotary pump are running and the whole instrument is enclosed by insulated metal heat shields.

The suitcase and the load lock chamber can be connected separately to the turbo molecular pump of the preparation chamber.

The preparation chamber contains a manipulator and an ion gun. The manipulator allows the annealing of a sample and the placing of it in front of the ion gun. The temperature of the manipulator is measured by a thermocouple. The ion gun is used to clean sample surfaces which is described in Section 2.4.

## 2.2 Scanning Tunnelling Microscopy Head

The STM head has to provide a piezoelectric scanner together with a damping system to achieve atomic resolution without being influenced by external vibrations. It also has to allow voltages between tip and sample for the STM and the FE mode to be applied and currents at the sample to be measured. The Omicron STM-1 is shown in Figure 2.2.

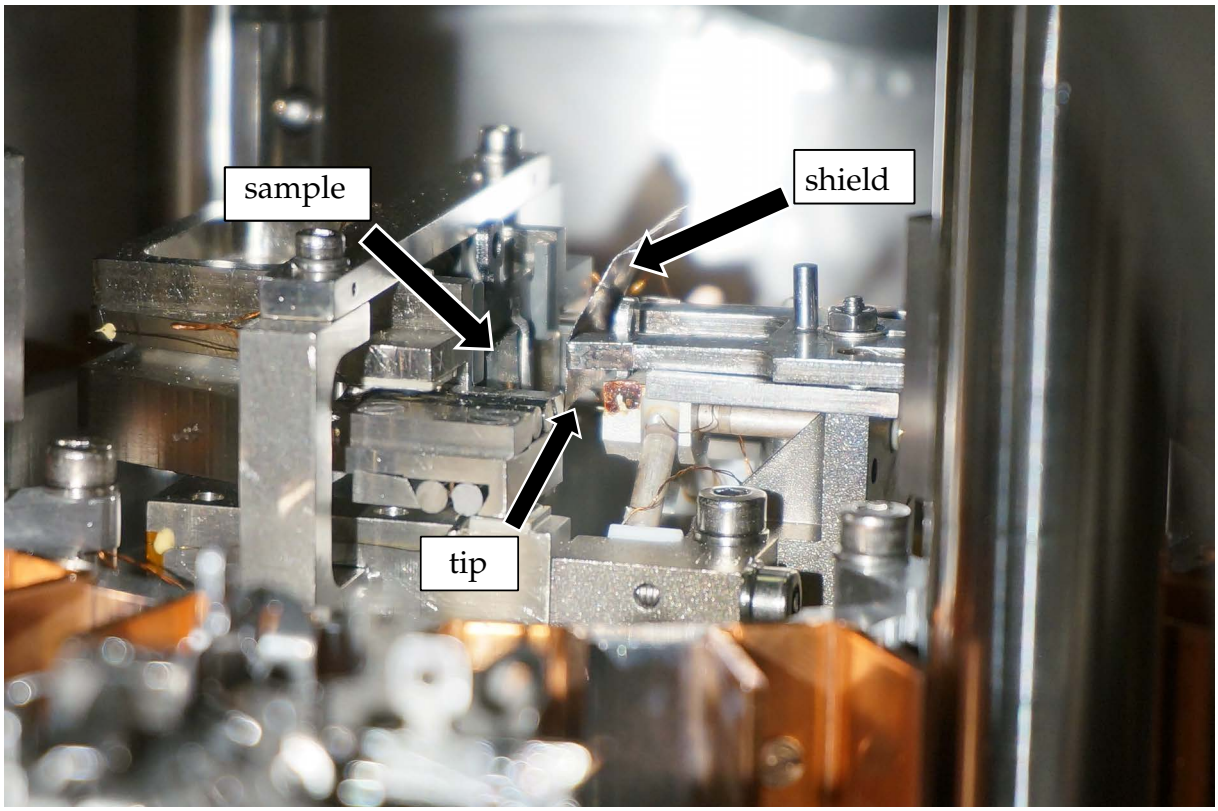


**Figure 2.2:** Omicron STM-1 stage fixed in the upper position. Only the lower part of the tip is visible.

The Omicron manual for the STM states a sensitivity in movement of the piezoelectric ceramics of 5 nm/V in Z and 9.5 nm/V in X and Y for small scan ranges. The ceramic structure consists of electric dipole moments which can be aligned by an external electric field. This leads to an extension of the material in one dimension. The STM tip is held by three piezoelectric ceramic tubes which are arranged orthogonally to each other. This allows precise movement of the tip in each direction. The lateral range for the tip is $\pm$1330 nm and the range of height variations is $\pm$750 nm with the sensitivities mentioned above. To gain a sufficient expansion of the piezoelectric ceramics a high electric field has to be applied. A grounded tantalum foil is placed between the piezoelectric tubes and the sample to prevent any perturbation of the trajectories of the electrons in SPELS mode. The shield slides towards and away from the sample to allow tip exchange. This is done with the wobble stick that can push the post in front of the screw on the right side in Figure 2.2.

The original STM-1 had a pre-amplifier attached to the STM head in order to increase the signal to noise ratio of the measurement. As the STM mode and the FE mode require different current ranges the amplifier needs to be switched between each mode. Therefore the in-situ amplifier is removed and the amplifiers are situated outside of the chamber. The power supply and the amplifier for each measurement mode are connected by coaxial cables respectively.

The damping system of the Omicron STM-1 is realised by a spring system with a low eigen frequency and a magnetic damping system where a ring of magnets which are connected to the chamber are placed between copper plates which are fixed to the STM head. Any movement of the STM head will cause an eddy current in the copper plates and moderate the initial movement. The magnetic field at the position of the sample was measured with a Hall probe to <0.01 mT which is at the resolution limit of the instrument. The STM head itself is designed to be as small and rigid as possible to

have a high eigenfrequency. The combination of components with low and high eigen frequencies leads to the suppression of most external vibrations.

The sample can be moved by inertia drive shear piezos. This is also how the tip approach works. The step size of the sample is about 100 nm. After each step the tip approaches to check if the sample is in range and then retracts before the next step. However, the lateral sample movement is restricted to the horizontal. The vertical is only covered by the tip movement which is along the diagonal scan range of maximal 3.76 µm or one can lift the sample in the STM stage by hand with the wobble stick by 2-3 mm. However, the movement by hand lacks not only in precision but the sample cannot be placed in any position as the polytetrafluorethylene (PTFE) wheel at the bottom of the STM stage forces the sample either up or down (see Figure 2.3).

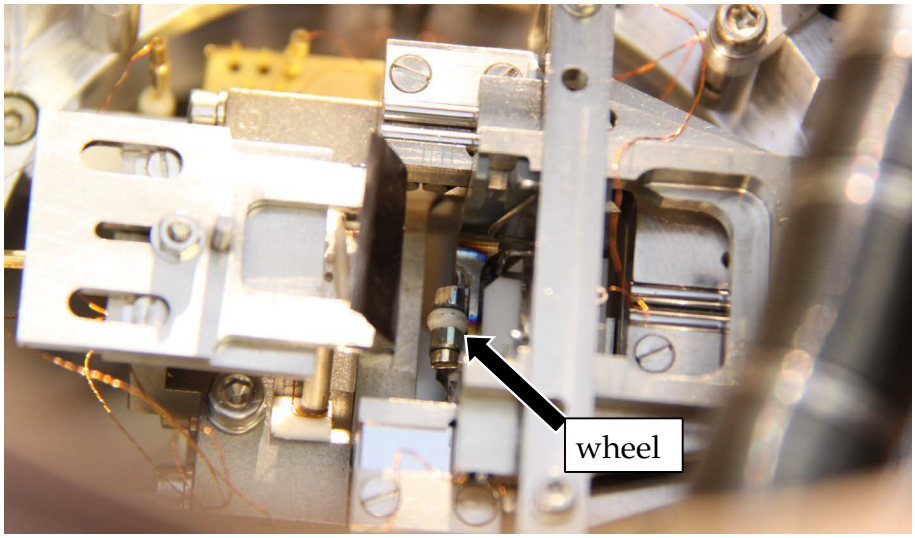


**Figure 2.3:** Omicron STM-1 stage. The wheel holding the sample at the bottom is marked. There is no tip or sample loaded.

## 2.3 Electron Energy Analyser

The electron lens system, analyser and detector are shown in Figure 2.4. The multi channel analyser (MCA) is situated in a separate chamber above the STM which is connected to the main chamber by an 8 inch wide linear drive. The distance from the sample to the analyser is bridged by a series of electron transfer lenses (E2, E1, E0). The minimum distance from the sample to the entrance of the E2 transfer lens is about 4 cm. When the detector is lowered the wobble stick is blocked by the lens system. The linear drive allows the detector to be raised by 5 cm to allow the wobble stick to pass. If the detector is lowered, the lens system focuses on the sample with an angle of 7° to the sample surface. The lens system also focuses the electron beam onto the entrance slit of the analyser (B3, B4). The electrons are separated through their energy in the 127° cylindrical sector analyser. This analyser was designed to give a direct correlation between the absolute applied voltage and the shift of the position of an electron with a certain energy. A change of 1 V in the "AN1" voltage would lead to a spatial shift of the electron position at the multichannel plates (MCPs) that corresponds to 1 eV. This can be used to calibrate the detector as described in Section 3.4.1.3.

After the detector, the electrons reach a series of five MCPs, which multiply the amount of electrons, and then arrive at a resistive anode plate. The current signals are measured at the four corners of the anode plate. The difference in the signal from each of the corners is used to determine the position of the incident electrons on the anode and therefore the energy of the electron. The resolution of the instrument depends on the dispersive effect in the cylindrical analyser which sets the energy range projected on the MCPs. An incident electron at the first MCP will lead to a wider lateral distribution of incident electrons on the resistive anode. The detector has a resolution of 1/400 along the width of the resistive anode. The maximal achievable resolution stated by the

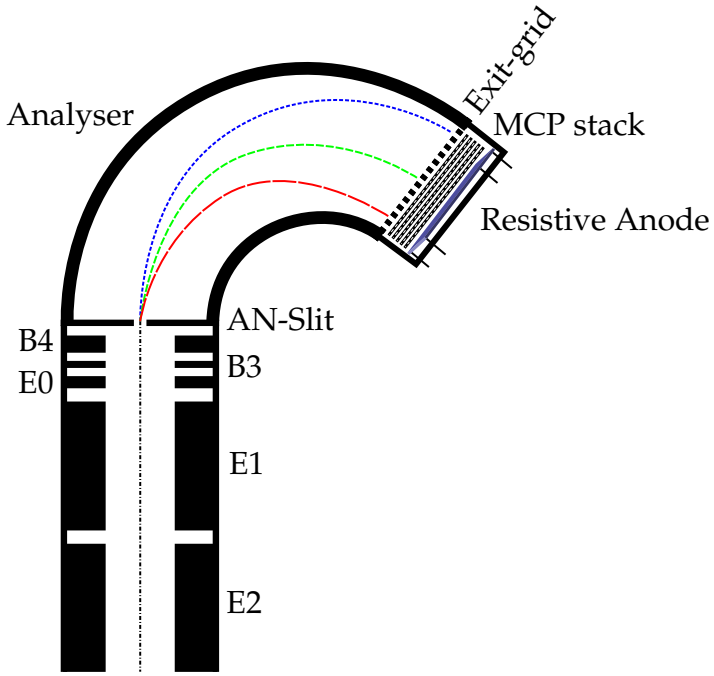


**Figure 2.4:** Schematic of the Electron Energy analyser with electron lens system (not to scale). The dotted lines represent electron trajectories for different electron energies. The actual length of the entrance lens part is 320 mm.

supplier is 2 meV at low electron energies.

## 2.4 In situ Sample Preparation

The annealing of samples in the manipulator is used for cleaning surfaces like gold and to prepare heterogeneous samples like silver on HOPG.

To produce an heterogeneous sample consisting of silver on graphite, a silver layer is evaporated onto the graphite substrate. This was performed with a basic evaporator installed in the suitcase. It consists of a crucible which is attached between two electrical

feedthroughs that are used to resistively heat it. With this simple design no reliable measurement of the evaporation rate is possible. The sample is then annealed to about 600 °C to enhance the mobility of the silver atoms on the surface. The diffusing silver atoms have a higher stability at silver islands which leads to the growth of silver islands which are separated by bare graphite. This process is called Volmer-Weber growth [76]. Examples of this are presented in Section 5.4.

The ion gun cleans a sample surface by sputtering the first atomic layers away. The preparation chamber is filled with argon up to a pressure of $1 \cdot 10^{-5}$ mbar while the ion pump is switched off and the turbo pump is connected at full speed. The ion gun ionizes the argon atoms and accelerates the ions towards the sample. The ion current to ground is measured via a thermocouple attached to the sample stage. To clean a graphite surface decorated with silver an ion energy of 500 eV and a current at the sample of 20 μA is used for 90 s.

To clean a gold surface the sample is first annealed at 620 °C for 5 minutes and then held at 420 °C for 30 minutes before being sputtered with 500 eV argon ions at 5 μA for 30 minutes. The annealing will transport impurities to the surface where they are sputtered away. This cycle is repeated several times until the surface is clean which is determined with the STM. The sample is clean when the atomic structure or, at lower resolution, step edges can be resolved.

## 2.5 SPELS Software Environment

SPELS measurements were performed using three different programs. STM and FE measurements were performed using the Nanonis program while the FE voltage is set by a LabView program "SloanSPELS_7t" written by Dr. Peter Sloan (at the University of Bath since 2010). It was initially designed for the EELS system but adopted for SPELS.

This program uses the interface of the Nanonis program to access the parameters of the STM. It also calibrates the detector. The lens voltages of the electron energy analyser are set by a Basic program written by the manufacturer LK Technologies.

To set up a SPELS measurement the LabView SPELS program was used to raise the FE-voltage and the Nanonis software was used for the automatic coarse approach of the tip in FE mode. If a count rate was seen, the lens voltages were adjusted with the LK program. The calibration of the detector was done with the LabView program by taking a spectrum and determining the position of the elastic peak for a series of FE-voltages. The position on the detector is related to the MCA-voltage. The data points ($U_{FE}$, $U_{MCA}$) are used to obtain the coefficients of a polynomial conversion formula of second degree. Then the Nanonis software performs a grid scan using the customised LabView program "Grid_SPELS_v4" which applies the conversion formula to process the data. The SPELS image is viewed with the Nanonis program "Binary File Inspector" during the scan.

The LabView program "SloanSPELS_7t" also has the possibility to perform a FE-voltage sweep to generate Fowler-Nordheim plots. As with this software version no further processing of the measured data is possible, this task was performed with the Nanonis software which allowed to save the data points and process it with a third party program like MATLAB [77].

The calibration method of changing the FE-voltage and therefore the incident electron energy to see the elastic peak in the backscattered electron spectra moving by a known energy step has the disadvantage that the electrons are influenced by different electric fields before they reach the detector. Therefore the signal intensity for FE-voltages far away from the voltage for which the lens voltages were optimised decreases due to the misalignment of the lens voltages.

# Chapter 3

# Development of SPELS Instrument

## 3.0 Perspective

At the beginning of the project there was only limited control over tip and sample preparation and detector calibration in the SPELS system. To improve the performance of the SPELS system a series of developments have been implemented.

The MCA broke in November 2013 and had not provided spectra with high signal to noise ratios. With this analyser, it was still necessary to accumulate a spectrum over one point for 1-3 seconds. To increase the signal level a new analyser that allows the detector to be positioned very close to the sample was needed. Furthermore, it is desirable to be able to withdraw the analyser into a DN35CF tube to be able to include a DN63CF viewport on the adapter flange that would support the analyser. The most compact analyser design is that of a retarding field analyser, which also allows to place a detector nearer to the sample as it would be possible with band-pass filter type analysers like an hemispherical or cylindrical sector analyser. Therefore, a new retarding field analyser was built, which potentially can utilize a much higher signal level (see Section 3.1). The analyser performance has been investigated by SIMION simulations (see Section 3.1.4).

In Section 3.2 the revised tip etching setup is explained and results of a quantitative characterisation of tips in dependence on their etching parameters are described. Also,

a new tip conditioning stage was implemented to allow several tip preparation methods to be performed *in situ*. Its design and the preparation methods are described in Section 3.3.

The SPELS software environment for the MCA was revised and extended so that the LabView SPELS program could control the analyser, making the original program redundant, and also allowing a new method of calibrating the multichannel detector (see Section 3.4.1). The software needed to work with the RFA and to process SPELS data are described in Section 3.4.2 and Section 3.4.3.

## 3.1 Retarding Field Analyser

The decision to build the RFA was made in November 2013. The size of the MCA meant most of the electrons are lost to detection because the detector has to be far away from the sample to accommodate the cylindrical sector analyser. To avoid this problem a new detector should be small enough to be placed near the sample. Also the ability to pull it into a standard DN35 UHV tube was desired to be able to accommodate the whole detector setup on a DN150 flange with a viewport for easier handling of the STM-1. The detector setup and method of operation are described in the following sections.

### 3.1.1 Method of Operation

The RFA utilises a variable electric field to analyse the energy of incoming electrons. This retarding field is essentially a barrier for incoming electrons on their way to the detector creating a high pass filter for electrons so that only electrons with sufficient energy can reach the detector.

By sweeping the retarding voltage over the desired energy range you get an integrated

spectrum – by decreasing the retarding field strength not only electrons with energies at this field strength will reach the detector but also all electrons with higher energy. The spectrum can then be calculated by differentiating over the signal. In reality one has no continuous signal but a series of sampling points with a uniform distribution over the energy range. The spectrum is then calculated by subtracting from each sample point the next higher energy sample point. The new value represents the counted electrons within the energy range between the two sample points. In this way a series of *n* sample points leads to a spectrum with *n-1* points.

### 3.1.2 Design

The detector is depicted in Figure 3.1. To create an even field distribution a series of

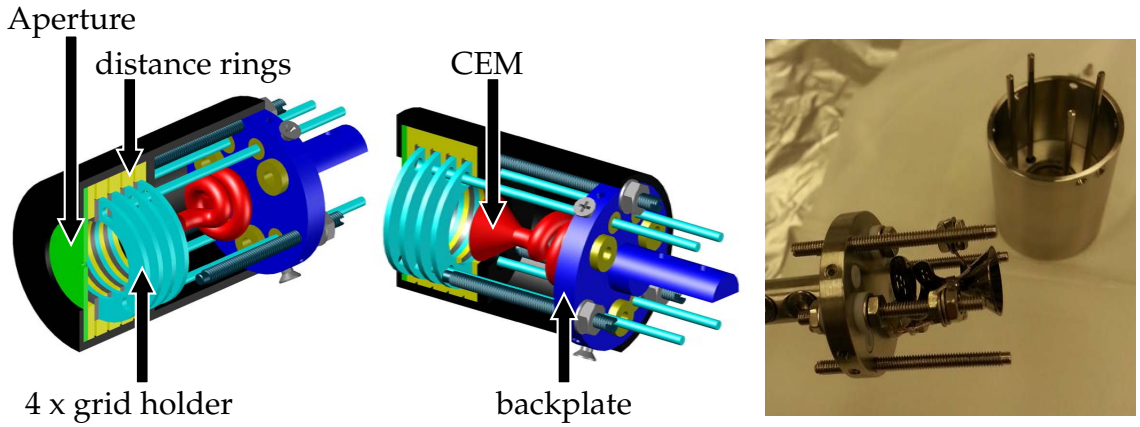


**Figure 3.1:** Sketch and Photograph of the new RFA. The rods supporting and contacting the CEM are not displayed in the sketch.

four grids is used. The first and fourth grid are grounded (sample potential) while the retarding voltage is applied to the second and third grid. The grids have been purchased from SPI[1] and are made from Au with an open area of 85% per grid. The hole size of the mesh is 234±2.5 µm and the bar width is 19.8±2.5 µm. The mesh is cut into circles and

[1]SPI grids can be purchased via Aztech Trading in the UK, SPI# 02199G-AB

hold between two stainless steel rings which are spot welded together. A stainless steel rod is welded to each of the four grid holders to act as a contact at the back of the RFA. PTFE distance rings isolate the grid holders from each other and the grounded case of the RFA. The holes in these distance rings are smaller than the holes in the grid holders to reduce the risk of shorting the grids. An aperture can be placed in front of the grids.

The case of the RFA is a hollow cylinder of 31 mm outer diameter with a wall thickness of 1.5 mm and a length of 43 mm. This allows the detector to withdraw into a 2 3/4 inch tube. The back is open while the front has a hole of 16 mm diameter. The aperture and grid holders slide from the back into the case. The inner diameter of the grid holders is 14 mm. The channel electron multiplier (CEM) is mounted on the backplate which can be fixed to the case by three screws from the side. The backplate has 7 feedthroughs isolated by PTFE washers for the 4 grids and the 3 contacts of the CEM. It also has 3 threaded holes which are used for screws that hold the stack of aperture and grid holders in place once the backplate is fixed to the case.

The aperture is a 1 mm thick stainless steel plate with the desired hole in the middle that is inserted at the front of the stack. This allows a fast and easy replacement of the aperture which is ideal to test different aperture sizes.

The backplate is connected to a rod which in turn is connected to a linear drive. The linear drive has a 4 inch stroke. This allows the detector to be moved out of the way for tip and sample transfer while it can have a minimal distance to the tip-sample junction of about 20 mm during measurements. The distance between the tip apex and the CEM entrance is 38 mm. The drive is mounted on a DN35 port on a custom DN150 flange which is shown in Figure 3.2. SHV type electrical feedthroughs are situated in the side ports of the DN35 cross before the linear drive. The DN16 ports on the flange are focussed on the sample but have not been used so far. The DN100 window has its own port opposed to being welded into the flange to allow an easy replacement in case the

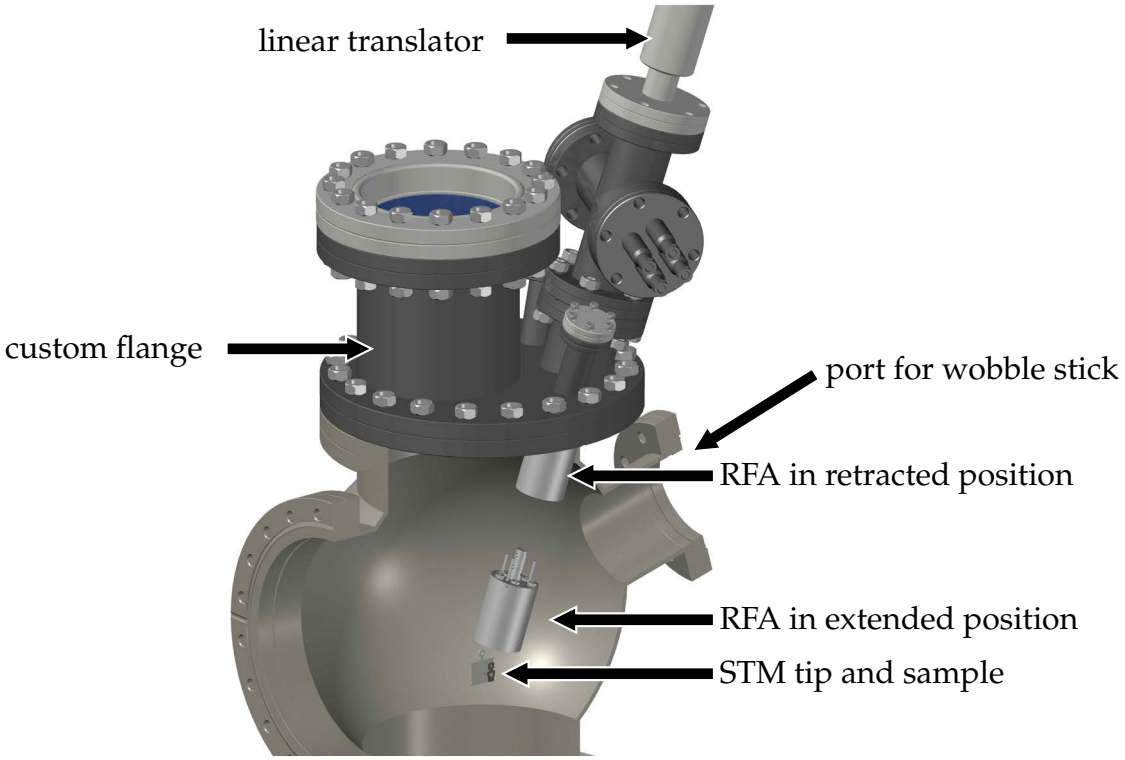


**Figure 3.2:** RFA flange mounted on the STM-1. The RFA is shown in retracted and extended position. The STM-1, the wobble stick and the support rod for the RFA in extended position is omitted for clarity. The wobble stick cannot reach the RFA while it is retracted.

window gets damaged.

### 3.1.3 Detector

The detector is a CEM from Photonis[1]. A CEM consists of a long lead silicate glass tube which has been reduced by hydrogen at high temperature resembling a continuous dynode multiplier [78]. An incoming electron produces secondary electrons at the entrance which in turn are accelerated on their way through the tube until they hit the wall and produce more free electrons. This avalanche process can produce a gain of $10^7$ in analogue mode and up to $10^8$ when saturated in pulse counting mode (see below

[1]Channeltron® CEM 4502 EIC

for details). The maximum operating voltage is 3 kV. The resistance between front and back contact is about 300 MΩ. The opening of the front funnel is 9.91 mm diameter. There are three contacts to the CEM which are front, back and collector contact. The Voltage between front and back contacts defines the working point of the CEM. The collector requires to have a positive voltage compared with the back of the CEM to attract the electrons generated at the end of the channel. This CEM can be operated in pulse counting mode and analogue mode. Both modes have been implemented. At the same count rate, the signal to noise ratio is higher for the pulse counting mode compared to the analogue mode but the pulse counting electronics saturates at 1 MHz while in analogue mode the CEM can exceed this limit.

The front of the Channeltron has to be grounded or positive with regard to the last grid so that the electrons are not repelled from it. The electron detection efficiency of the Channeltron depends on the electron energy as shown in Figure 3.3. Note that the plot

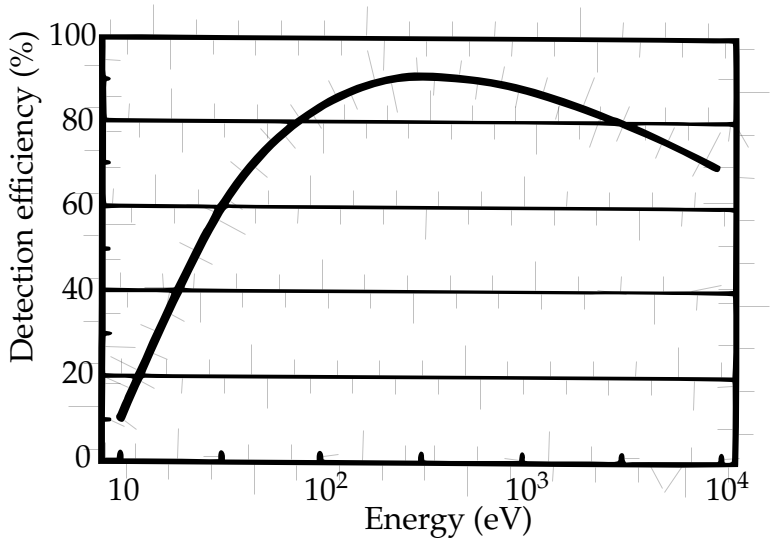


**Figure 3.3:** Electron Detection Efficiency of a CEM in pulse counting mode (taken from [78])

in Figure 3.3 has a logarithm energy axis and the detection efficiency decreases rapidly for energies below 100 eV. After the electrons pass the retarding field between grid 2

and 3 they are accelerated again to their initial energy. To measure secondary electrons with energies below 25 eV reliable a positive voltage of about 350 V (depending on CEM voltage) is applied between grid 4 and the front of the CEM. This shifts the electron impact energies back to regions with high detection efficiency. The high positive voltage at the back of the Channeltron must be raised accordingly to achieve the same electron gain through the channel.

#### 3.1.3.1 Pulse Counting Mode

In pulse counting mode the resulting charge pulse from an incoming electron is counted.

The CEM is operated in space charge saturation which means that due to positive charging of the channel walls at the end of the channel no additional free electrons are produced [78]. This leads to a Gaussian shaped pulse height distribution.

To reach space charge saturation the working point of the CEM has to be high enough. To find a sufficient value the tip is biased near the sample until a FE current is measured. Then the CEM voltage is ramped up until a plateau is reached. The CEM is chosen to a value about 50-100 V above the onset of the plateau. This ensures a stable and comparable signal output. Higher voltages are avoided to reduce ageing effects on the CEM. A typical signal-to-CEM-voltage sweep is shown in Figure 3.4.

The onset of the count rate plateau shifts to higher values over time due to ageing effects of the CEM. For the RFA the value has increased by about 180 V since its installation.

As the signal must be read out at the high voltage side of the Channeltron a high voltage capacitor is used to isolate the signal output and protect the pulse counting electronics. The ratemeter used in these experiments was kindly borrowed from Yu Chen[1] and consisted of a nuclear instrumentation module (NIM) standard ORTEC 9349 Ratemeter

[1] Dr Yu Chen, Department of Physics, University of Strathclyde

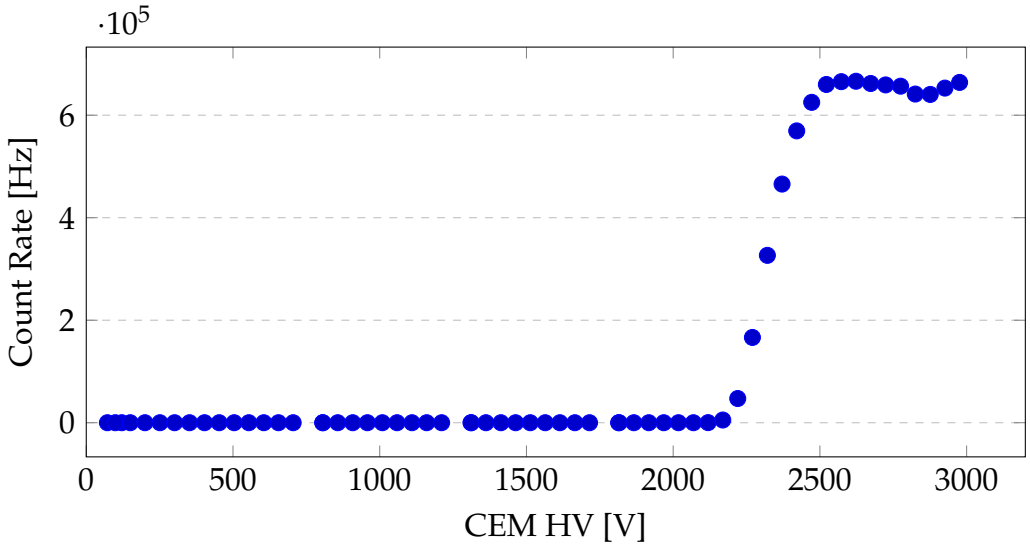


**Figure 3.4:** CEM HV sweep to find a minimum value where space charge saturation occurs in the CEM. Taken on sample HS10 while at least 5 µm tip-sample-separation with a current of 120nA and a tip voltage of 120V. The retarding field voltage was 110V.

and an ORTEC 9302 Amplifier/Disciminator. The high voltage power supply is the same which was used for the MCA. The electronic circuit to run the CEM has been built from scratch and is shown in Figure 3.5. The resistor chain R1, R2 and R4 and the inherent resistance of the CEM form a voltage divider providing the necessary outputs. The resistor R2 and capacitor C2 form a low pass filter with a cutoff frequency of 159 Hz. This is necessary to eliminate fluctuations which would interfere with the signal leading to low maximum count rate. The voltage for the CEM is provided by an Acopian HV power supply[1] (labelled as "HV (3kV)" in diagram 3.5). Table 3.1 lists two examples for voltages at relevant points in the circuit depending on the power supply voltage.

The Amplifier is connected to the back of the Channeltron through the capacitor C1. It can be set to a gain of 20 or 200. A discriminator is included in this model. The discriminator threshold can be adjusted between 50 mV and 1 V. The discriminator output produces NIM-standard fast negative logic signals which are sent to the ratemeter [79].

[1] Acopian Technical Company, model P05HP6, $V_{max} = +5\,kV$, $I_{max} = 6\,mA$

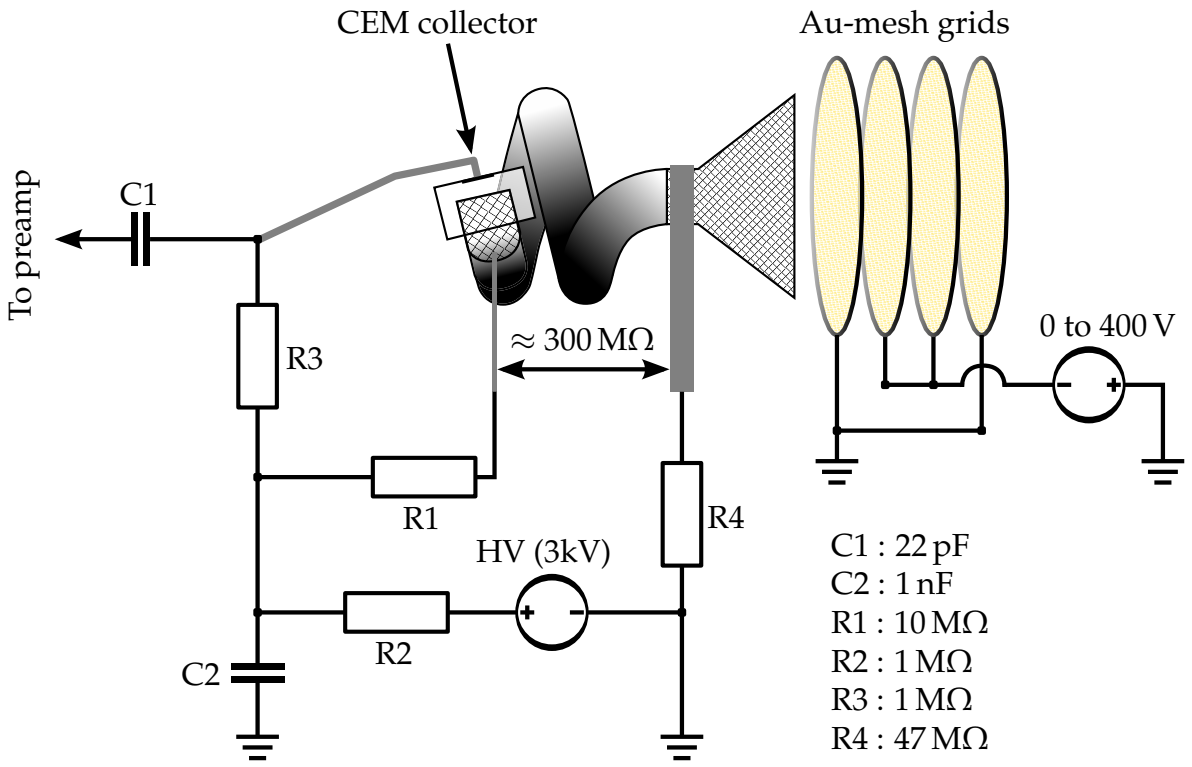


**Figure 3.5:** RFA electronics for pulse counting mode. R1, R2, R4 and the resistance of the CEM tube of about 300 MΩ acts as a voltage divider to power the CEM. R2 and C2 form a low pass filter. R4 lifts the potential at the CEM entrance to increase electron detection probability. C1 isolates the counting electronics from the high voltage applied to the CEM collector.

**Table 3.1:** Examples for applied CEM voltages. Typical values for HV are between 2.5 kV and 3.1 kV.

| Resistances used: | |
|---|---|
| R1 | 10 MΩ |
| R2 | 1 MΩ |
| R3 | 1 MΩ |
| R4 | 47 MΩ |
| CEM | 300 MΩ |

| HV = 2.5 kV | |
|---|---|
| CEM front | 328 V |
| through CEM | 2095 V |
| CEM back to EIC | 70 V |

| HV = 3.1 kV | |
|---|---|
| CEM front | 407 V |
| through CEM | 2598 V |
| CEM back to EIC | 87 V |

The ratemeter has a dynamic range up to 1 MHz and a 10 V analogue output. The time constant can be varied from 0.03 s to 30 s in 1-3-10 steps. The analogue output is read by the Nanonis controller and converted to counts per second.

#### 3.1.3.2 Analog Mode

In analogue mode the current at the collector of the CEM is measured directly. For this the working point of the CEM lies within its dynamic range and before space charge saturation is reached. The collector current is directly dependent of the incoming electron flux and is measured with a picoammeter. As mentioned before, this type of measurement has a higher background noise level compared to the pulse counting mode but also a higher count rate limit. The theoretical limit is at 10 % of the CEM current which is in the order of 5-30 μA [80].

As the back of the CEM is at high voltage, the picoammeter measuring the current needs to float at this high voltage. It is also important that the current at the picoammeter is limited. The input protection circuit replacing the high voltage capacitor is shown in Figure 3.6. The Keithley 6485 picoammeter has an input voltage burden of less than

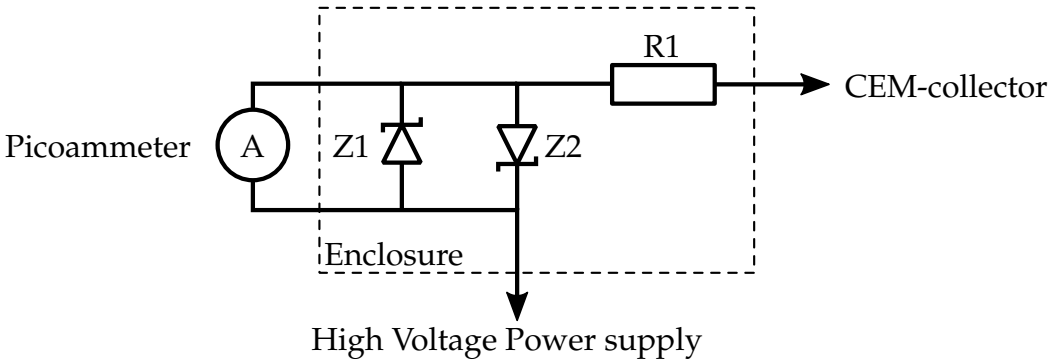


**Figure 3.6:** Input protection circuit for the picoammeter when the CEM is operated in analogue mode. Resistor R1 has a value of 1 MΩ. The small signal Zener diodes Z1 and Z2 are from type 1N3595.

200 μV for a current range of up to 2 mA [81]. The leakage current of the 1N3595 diodes at these voltage drops can be neglected. The resistor limits the current through the diodes, which are photo sensitive and are therefore enclosed in a box.

The picoammeter is contained within a custom perspex box to protect the user from the high voltage. The power and signal connections are isolated by an isolation transformer from Block[1] and an optoisolator from Scimar[2]. The connections to the CEM-collector and the high voltage are made through safe high voltage (SHV) connectors which are fitted in the back wall of the perspex box. This allows an easy switch between the pulse counting mode and the analogue mode without the need for additional wires.

### 3.1.4 SIMION simulations for the Retarding Field Analyser

The retarding field principle allows a rather straightforward and compact analyser design with a high transmittance for incoming electrons. However, this comes at the cost of energy resolution and the small design does not allow an effective use of spherical grids - a common feature of low-Energy electron diffraction (LEED) optics [82]. As a result an aperture has to be used at the entrance of the analyser to reduce effects which lead to a distortion of the energy spectrum and therefore to lower energy resolution. These effects are described below. However, a small aperture reduces the transmittance and therefore a trade-off between high signal (big aperture) and resolution (small aperture) has to be made. With SIMION the optimal aperture size can be found.

SIMION is an ion optics simulation program to calculate the electric field from a given set of electrodes and to simulate ion or electron trajectories within this field. SIMION was used to determine the resolution of the RFA in dependence of the aperture size used. The electrodes for simulation can be drawn within the program or a geometry

[1] Block TIM 100, isolation transformer 100VA
[2] SCIMAR OP232/D1, RS232 optoisolator

file (*.gem) can be written which defines the physical boundaries of the electrodes. The latter approach was used. The initial position and velocity or energy vector are defined in a fly file (*.fly2). The electric field is stored in a *.pa file. The results are stored in a text file or can be processed with a user program using the LUA programming language. This section discusses the results of SIMION simulations of the RFA.

The RFA has parallel mounted grids which can cause a distorted energy spectrum when measuring electrons from a point source as the angle of the incoming electrons influences the probability of it being detected. Assuming a rotationally symmetric detector and a centred point source in front of the detector, the calculation of electron paths in the detector can be simplified to a 2-dimensional problem as shown in Figure 3.7. The energy of an incoming electron can then be written as an on-axis component which is parallel

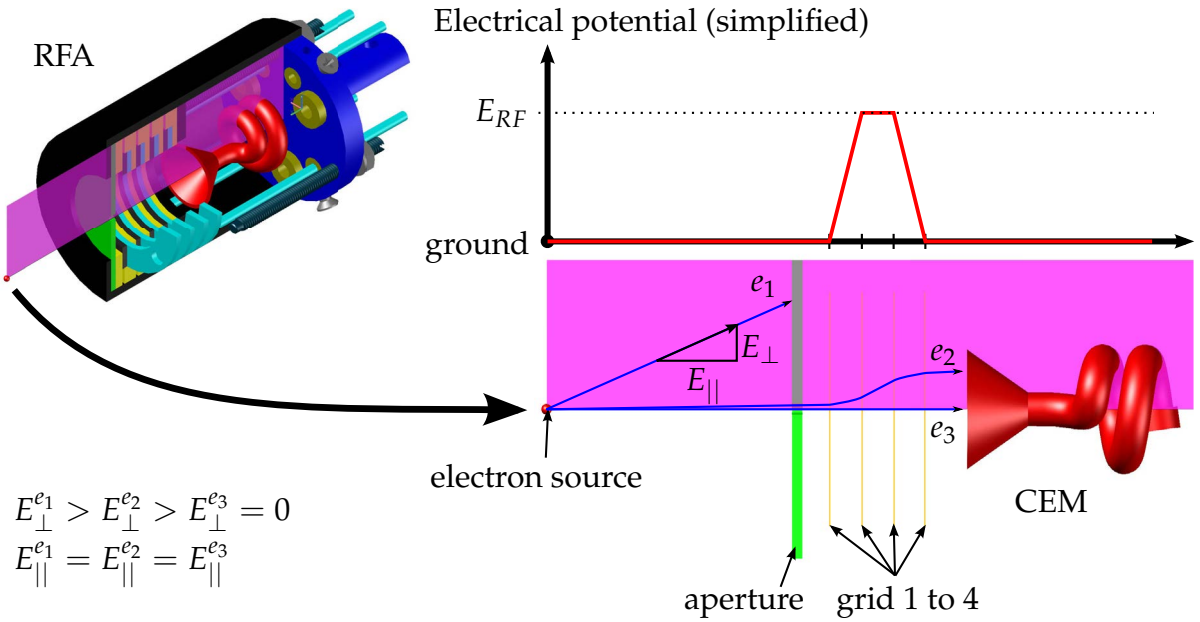


**Figure 3.7:** 2-dimensional representation of electron paths in the RFA under the presumption of a centred electron source. Electron paths are sketched as blue lines. For a given $E_{RF}$ the lateral displacement of the electrons within the retarding field depends on the $E_{||}/E_\perp$ ratio leading to a bigger displacement for a lower ratio.

to the symmetry axis of the detector ($E_{||}$) and an off-axis component perpendicular to the symmetry axis ($E_{\perp}$).

$$E = E_{||} + E_{\perp} \tag{3.1}$$

Assuming an electron with a trajectory parallel to the detector axis. To pass the barrier it needs to have an energy $E \geq eU = E_{RF}$, with $E_{RF}$ being the energy lost by the retarding field. Whether or not an electron with an arbitrary direction passes the retarding field depends only on the on-axis energy component of that electron being higher than $E_{RF}$.

$$E_{||} > E_{RF} \tag{3.2}$$

An electron passing the aperture with a non-zero off-axis energy component but a total energy exceeding $E_{RF}$ might still not reach the detector if the $(E_{||} - E_{RF})/E_{\perp}$ ratio is too small. It would then hit the detector wall. As this ratio is proportional to the retarding field the electron might then be detected at lower retarding voltage and hence as an electron with lower energy than its total energy. This leads to artificial tails on the low energy side of peaks in the energy spectrum.

To decide whether or not the energy resolution with a certain aperture size is acceptable, the simulation starts with a known spectrum (electron energy distribution) at several angles as input and builds an output spectrum by counting the electrons that arrive at the CEM for each retarding field voltage that is simulated. Of course an ideal analyser would show exactly the same spectrum just with a higher count rate. The initial spectrum originates from a SPELS measurement on a Ag/HOPG sample with the MCA. It has 500 energy channels ranging from 83.8 eV to 90.4 eV. This spectrum shows the elastic peak at 90 eV, the surface plasmon of Ag at an energy loss of 3.7 eV and a Ag interband transition below. The CEM entrance is modelled as a flat surface of 9.9 mm diameter. If an electron hits this surface it adds as many electrons to the element in the

output array that represents the current retarding field strength as electrons are in its inital energy channel. The spectrum is then generated by differentiation of this output array. In practice a point in the spectrum is the difference of two adjacent elements in the output array. The energy of this point is the mean of the energies that are represented by the involved array elements.

To realise this two user programs based on the lua programming language have been written. A simulation is started by running the first program which is called "main program". The parameters of the simulation can be set by changing variables at the beginning of the main program. This includes the start, end and step-size of the retarding field voltage and electron angle, the position of the elastic peak of the initial spectrum and the aperture size. The program then generates the geometry, fly2, pa and output files and folders, runs the refinement of the pa file and starts the simulation ("fly") for each retarding voltage. The second program contains functions which are called before and after each simulation of an electron. This program evaluates weather the individual electron hits the detector entrance or not and builds up the spectrum. It is possible to start the simulation and change the retarding voltage in this program but then no image of the result for each retarding voltage can be saved. Even though the simulation is reduced to a 2-dimensional case, the simulation with the parameters described below still takes several days for completion on a single workstation.

For this simulation the electrons in the initial spectrum are simulated with angles from $0^\circ$ to $7^\circ$ in $0.1^\circ$ steps and the simulation is repeated for retarding voltage values from 80 V to 92 V (0.1 V step). Therefore the resulting spectrum is in the energy range from 80.05 eV to 91.95 eV. Figure 3.8 shows the initial and resulting spectra for aperture sizes 1 mm to 7 mm.

Figure 3.8 shows a very good match between initial and simulated spectra for an aperture size of 1 mm and 2 mm. The simulated spectra starts to deviate from the initial

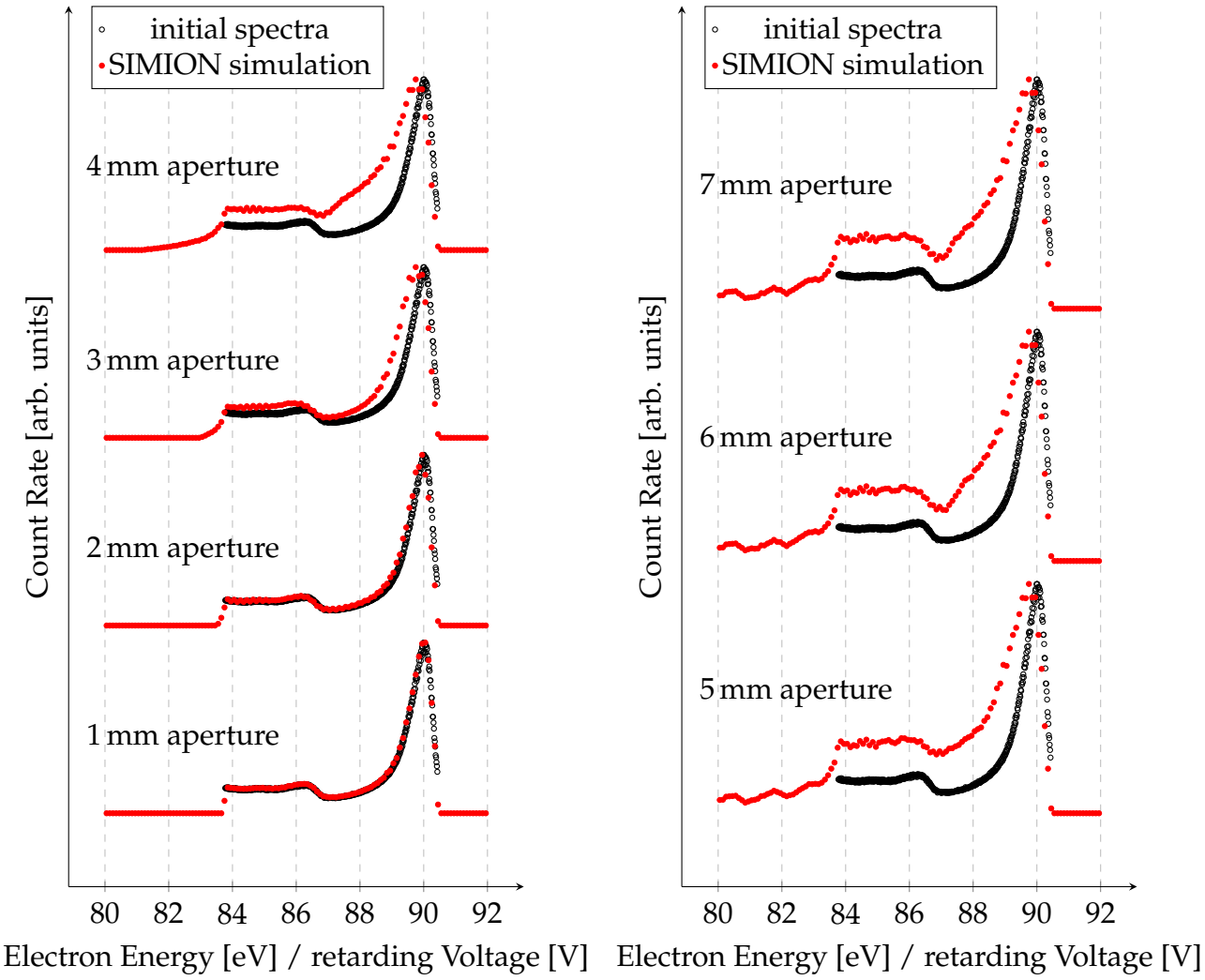


**Figure 3.8:** A comparison of the initial spectrum (black empty circle : ◦) with the simulated measured spectra (red filled circle : •) using the RFA for an aperture size of 1 mm to 7 mm. The initial spectrum has only energy values from 83.8 eV to 90.4 eV while the retarding voltage is scanned over the energy range from 80 V to 92 V.

spectrum from 3 mm aperture size but the plasmon peak is still visible at 3 mm. Note the additional peak at around 2.1 eV for aperture sizes of 4 mm and higher. With the 7 mm aperture no incoming electron is hitting the aperture (up to the simulated 7°). Therefore, the result for 7 mm will be the same for any bigger or no aperture present within the boundaries of this simulation.

In summary, the result of this simulation is that aperture sizes up to 3 mm are feasible

with the RFA. To reach the maximum input signal an aperture size of 3 mm should be ideal.

An additional result of this simulation is that the thickness of the grid holder leads to normally lost electrons being deflected back into the CEM as can be seen in the right picture of Figure 3.9. The electrons originate from one point on the left of the RFA which

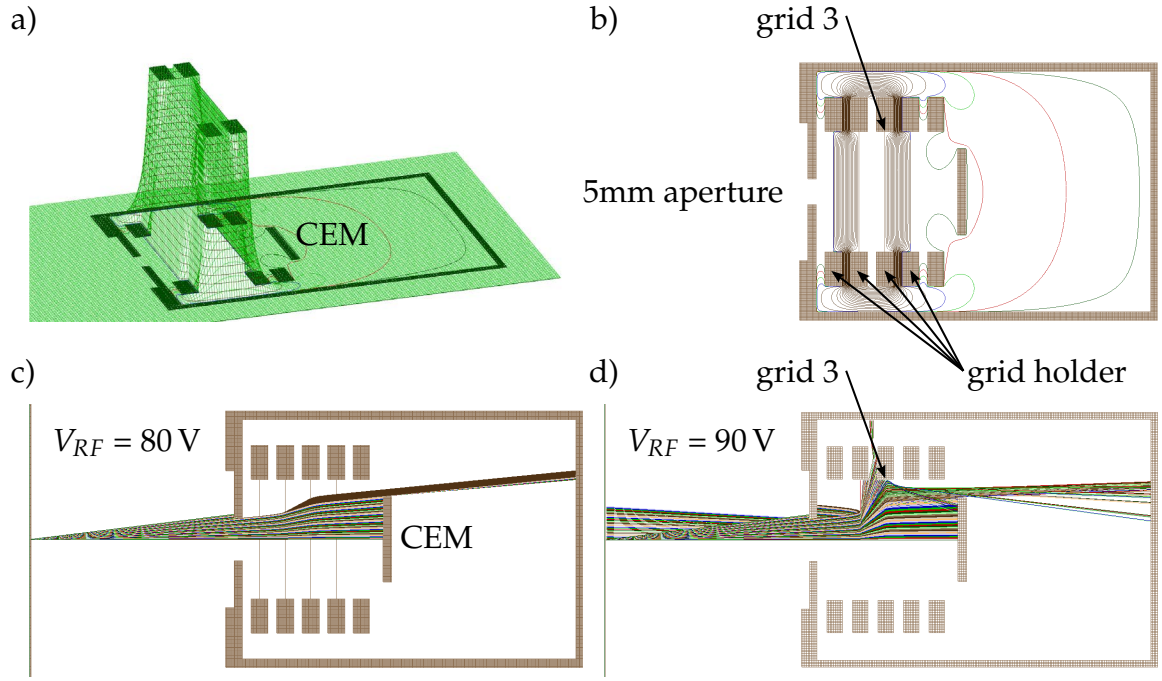


**Figure 3.9:** SIMION simulation of the RFA with a 5 mm aperture. Images a) and b) show the field distribution and equipotential lines for a retarding voltage of 100 V. Note the inhomogeneity of the field near the grid holder. Image c) and d) show the electron trajectories at retarding voltages of 80 V and 90 V. Note the electrons being deflected back towards the detector entrance in image d) due to the inhomogeneous field near grid holder 3.

lies on the symmetry axis of the detector and is 20 mm away from the detector entrance. At a retarding voltage of 80 V all electrons have enough energy to pass the retarding field although not all electrons that pass the aperture reach the CEM. Note that even though the number of measured electrons is highest at $V_{RF} = 80$ V (being the minimal retarding voltage simulated) the count rate at 80 eV is low as only the difference to

the number of measured electrons at the next retarding voltage counts towards the electron energy spectrum. At $V_{RF} = 90\,\mathrm{V}$ most of the electrons are being reflected. A small proportion of electrons that passed the retarding field with a $(E_{||} - E_{RF})/E_{\perp}$ ratio leading them to collide with the holder for grid 3 are deflected back towards the CEM. This is due to the finite thickness of 1 mm of the grid holder after grid 3 which causes an inhomogeneity in the electric field.

The results discussed in this section have been applied to SPELS measurements with the RFA which are described in Section 5.5.2.

## 3.2 Fabrication and Characterisation of Tungsten Tips

### 3.2.1 Electrochemical etching of tungsten tips

The STM tips used with SPELS are produced by electrochemical etching of a 0.25 mm tungsten wire using the Omicron W-Tek tip etching tool [83]. For electrochemical etching the tungsten wire and a silver counter electrode are dipped into a 2 Molar sodium hydroxide (NaOH) solution and a DC voltage is applied between the wire and the electrode. It is also possible to use potassium hydroxide (KOH) [84]. The NaOH is diluted with distilled water. The following reactions are taking place:

| | | | |
|---|---|---|---|
| tungsten wire (anode): | $W + 8\,OH^-$ | $\rightarrow$ | $WO_4^{2-} + 4\,H_2O + 6\,e^-$ |
| silver wire (cathode): | $6\,H_2O + 6\,e^-$ | $\rightarrow$ | $3\,H_2\,(\mathrm{g}) + 6\,OH^-$ |
| overall: | $W + 2\,OH^- + 2\,H_2O$ | $\rightarrow$ | $WO_4^{2-} + 3\,H_2\,(\mathrm{g})$ |

The $WO_4^{2-}$ sinks down and hinders the reaction at lower parts of the wire. Therefore the highest reaction rate occurs at the meniscus which weakens the strength of the wire at this point. If the diameter of the wire at the meniscus has reached the point where it cannot support the lower part of the wire any more, this lower part falls down and

a sharp tip remains. To obtain this tip, the voltage has to be switched off at this point. Otherwise the etching process will continue and will blunt the tip.

As the lower part of the wire has fallen down the available tungsten surface has decreased dramatically, which in return decreases the overall reaction rate and therefore the current which can be measured between tungsten and silver wire. There are two common modes to detect this event. In differential mode an electronic circuit reacts to a peak in the differential current by turning the voltage off. The threshold mode turns the voltage off if the current reaches a predefined threshold current.

Another method is to catch the lower part of the wire which has fallen down. As this part loses contact after the wire breaks, the etching process stops immediately and a sharp tip remains.

The tip is dipped several times into distilled water after it is removed from the etching device in order to remove any excess of NaOH which would otherwise crystallise at the tip.

It is crucial to control the overall length of the tip. If the tip is longer than 9 mm it will crash into the shield attached to the STM during tip exchange. If it is shorter than $\sim$6 mm it cannot be seen by the camera during coarse approach (with the MCA). The polycrystalline tungsten wire comes in pieces of 75 mm length. After a 15 mm long piece of tungsten wire is cut off and spot welded to a tip holder, the first 5.5-6.5 mm are etched away with a high etching rate at 9 V. This removes possible cracks in the wire which occur during the cutting of the wire. Thereafter, the etching of the final tip is performed. The immersion length of the tungsten wire in solution in the second step is 1.5 mm leading to an overall wire length of 7-8 mm which is suitable to fit in our STM.

### 3.2.2 Optimisation of the electrochemical etching setup

In the beginning of this work the polycrystalline tungsten wire and the silver cathode are placed in the same beaker using the Omicron W-Tek tip etching tool [83] as described in Section 3.2. To obtain a uniform and sharp tip, the surface of the solution has to be steady. Therefore the etching process has to be protected from vibration and air currents. The setup stands on a polystyrene block and is covered by a box. The tungsten wire can be lowered by a multimeter screw. The wire and the silver cathode are connected to a Omicron tip etching control unit which can operate in a tip adjustment mode, which gives a visual and audible signal when the tip is in solution, in differential and in threshold mode. The tips used in this work are etched in threshold mode at various etching voltages and threshold currents. This leads to different tip shapes as a lower voltage reduces the etching rate and produces a longer tip.

The $H_2$ forms bubbles at the cathode, which can ascend to the surface and produce waves. This can move the meniscus at the tip during the etching process, which produces steps in the shank of the tip. To prevent this, it is possible to place the cathode in another beaker than the tungsten tip which is connected to the first beaker over a subsurface pipe. This method has been implemented two-fold. My first approach was to use the same beaker but placing a quartz tube inside which is supported from top as shown in Figure 3.10. The inner tube separates the liquid surfaces above the two electrodes which reduced the amount of etched tips showing stepped flanks. However, the small diameter of the tube means that the liquid surface appears to be curved (concave) due to the meniscus at the inner tube wall reaching nearly to the centre.

Therefore, a glass tube was attached to a standard glass beaker[1] as shown in Figure 3.11. The silver wire is placed into the tube while the tip is lowered into the beaker. This

[1] this was done by Steve Williams from the glassblowing service in the School of Chemistry

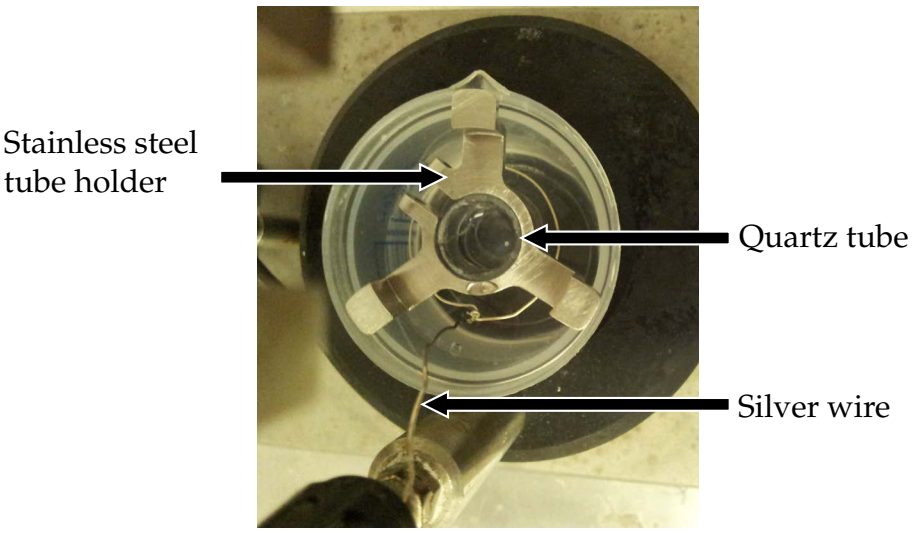


**Figure 3.10:** Modified tip etching stage using a suspended quartz glass tube to separate the liquid surfaces above the two electrodes. The tip is lowered into the solution within the quartz tube.

means that the cathode is not symmetrically located around the tip position. Therefore, the tube is attached to the lower end of the beaker and the amount of the solution was always chosen to fill the beaker at least to three quarters. With these precautions no directional etching was observed on the tips. The beaker was used with the same Omicron etching tool. It provides a bigger surface area for the tip and is much easier to handle than the inner tube holder.

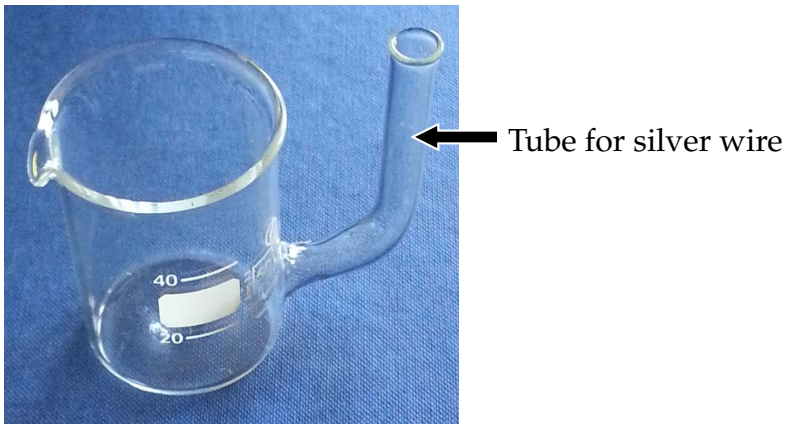


**Figure 3.11:** Tip etching beaker with attached tube for the cathode (silver wire).

### 3.2.3 Characterisation of Tips

The important influence of the macroscopic shape of the tips on the performance of the SPELS instrument makes it necessary to have a tip etching procedure which provides a high degree of control over the macroscopic shape as well as the tip apex size. The tip shape defines the electric field between tip and sample, as experienced by the outgoing low energy electrons. To produce different types of tip shapes, the etching voltage and the threshold current can be varied. The opinion at the beginning of my study was that a long, tapered tip etched at a low voltage and current (2 V, 1 mA) would be the best option, because it would generate an electric field distribution which suppressed fewer electrons and therefore yield a better SPELS signal at the detector. However, problems occurring during the SPELS measurements were unstable tip behaviour and a very small backscattered electron count rate. Often the tips produced no count rate at all and had to be replaced.

The existing tip preparation method was not optimized to produce suitable tips for SPELS measurements. Therefore a series of tips with different tip etching parameters were produced and characterised by scanning electron microscopy (SEM)[1]. The characterisation of the tips by SEM is described in the next section while the results are presented in Section 3.2.3.2.

#### 3.2.3.1 Scanning Electron Microscopy of Tips

The tungsten tips are characterized in a Philips XL 30 SEM housed in the NPRL clean room [85]. The SEM allows the examination of the macroscopic tip shape as well as the tip apex diameter, as shown in Figure 3.12. The typical imaging conditions are an electron energy of 5 keV and an emission current of 202 μA. The SEM has three different

[1] this work was partly done by Caroline Willis during her summer project 2011 under my supervision

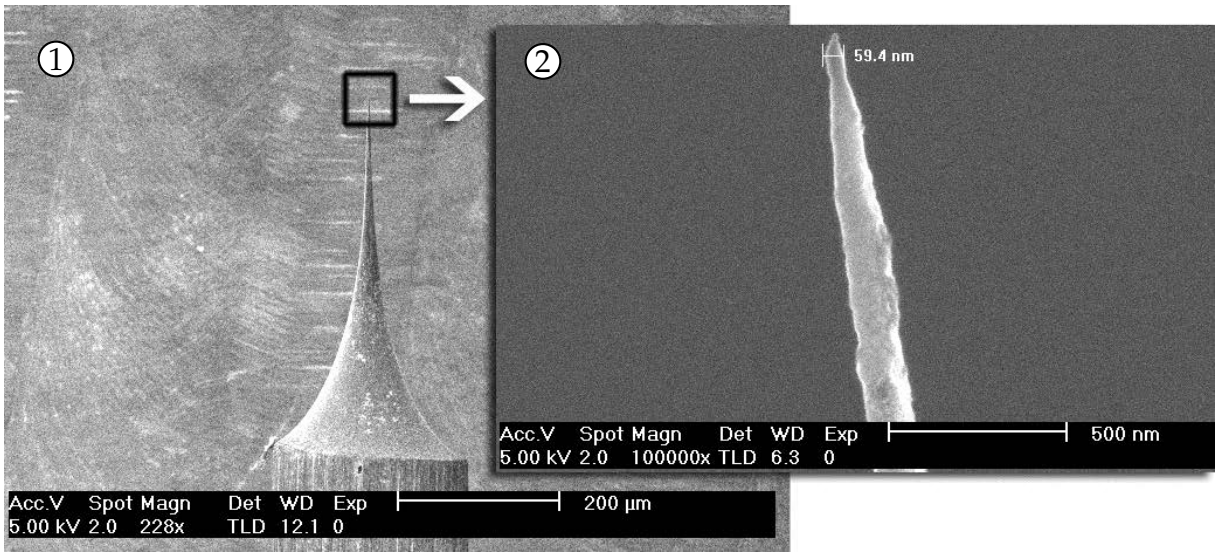


**Figure 3.12:** The macroscopic shape of a STM tip for SPELS is shown in the SEM image ① while ② shows the tip apex with the determined tip diameter of 59.4 nm.

detectors with different resolution limits. The secondary electron detector is used for a wide range of magnifications but has a lower maximum resolution than the inline detector which can only be used for magnifications higher than 3200. The backscattered electron detector does not provide clear images and was therefore not used.

The electron beam produces a contamination layer on top of any sample during imaging which was first discovered by Broers [86]. The removal of this contamination layer in an oxygen plasma cleaner has been tried, assuming that the tungsten oxide layer on the tip would prevent it from further oxidation. However, the tips treated this way had a apex diameter of less than 50 nm in the SEM images, but proved to be blunt in SPELS measurements after the usual annealing process. Hence, this cleaning step was not repeated.

It is possible that the exposure to air during the tip transfer between the SEM and the SPELS system alters the tip. Although care was taken to avoid any contamination some tips have been imaged twice without preparation steps in between as a reference. These tips show no change by the tip transfer as can be seen in Figure 3.13. This demonstrates

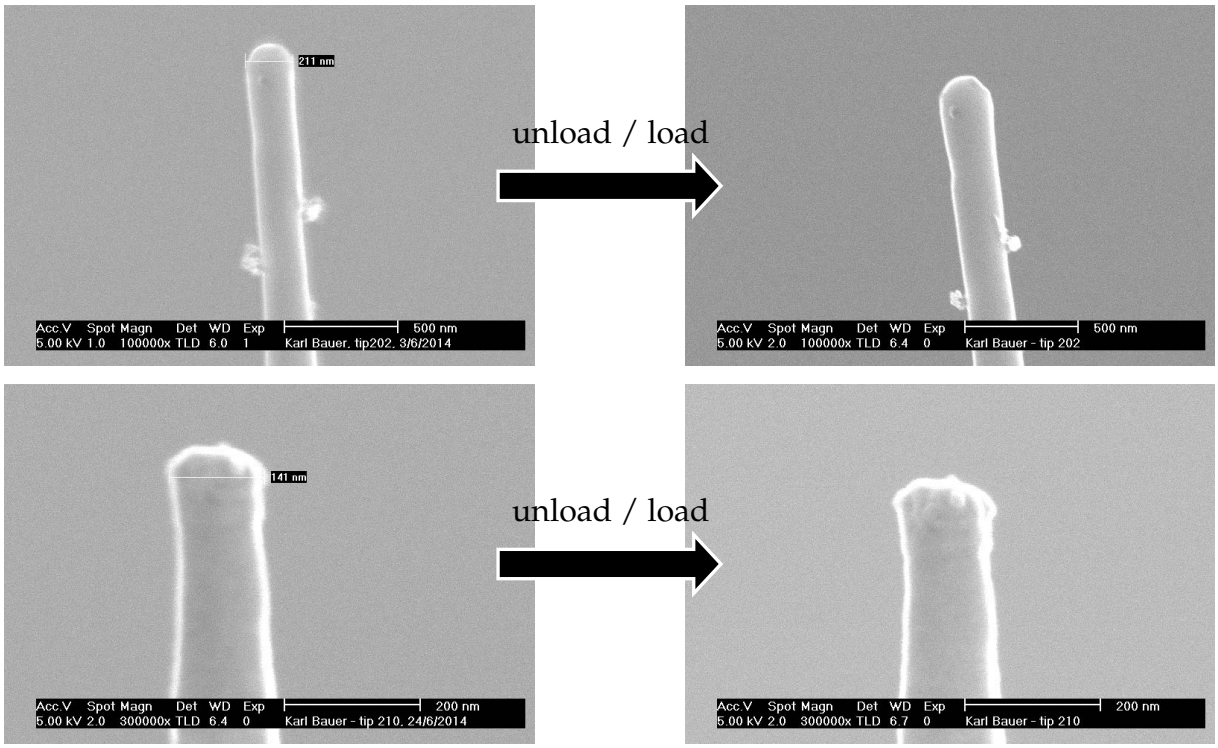


**Figure 3.13:** Reference tips for SEM characterisation. The tips have been unloaded from the SEM, stored in air and the SPELS system for 21 days (upper images) and 45 days (lower images) respectively and loaded again in the SEM. No tip preparation was done within this time.

the validity of SEM characterisation regarding tip shape and apex diameter. However, the last cleaning step of a tip should be done *in situ* before a measurement as the SEM will not show changes on the atomic level of the tip or the deposition of a water layer.

#### 3.2.3.2 Tip dependence on etching parameters

The main properties of a tip are the aspect ratio, which is the tip length divided by the wire diameter, and the tip apex diameter which are illustrated in Figure 3.14. It is also important that the tip is etched evenly to avoid additional field emitters and to improve tip stability. The tip length can be varied between the wire diameter of 0.25 mm and more than 1 mm by varying the etching voltage. Lower etching voltages lead to longer tips but also tend to produce tips with a higher apex diameter as can be seen from

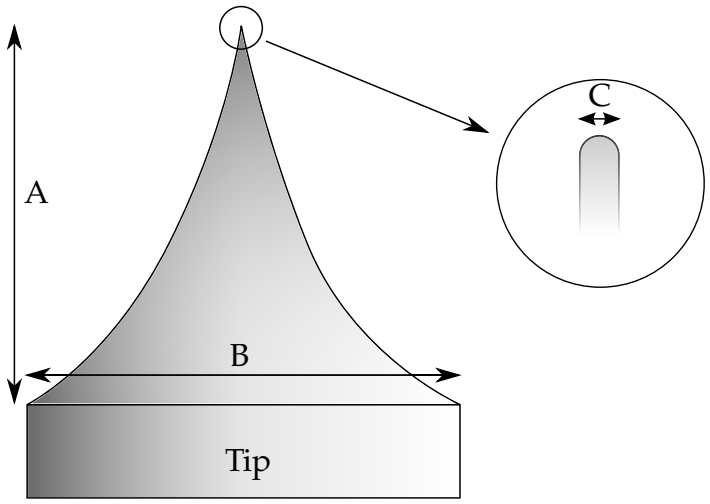


**Figure 3.14:** Schematic of tip geometry. The aspect ratio is the length of the tip A divided by the wire diameter B. The tip apex diameter is C.

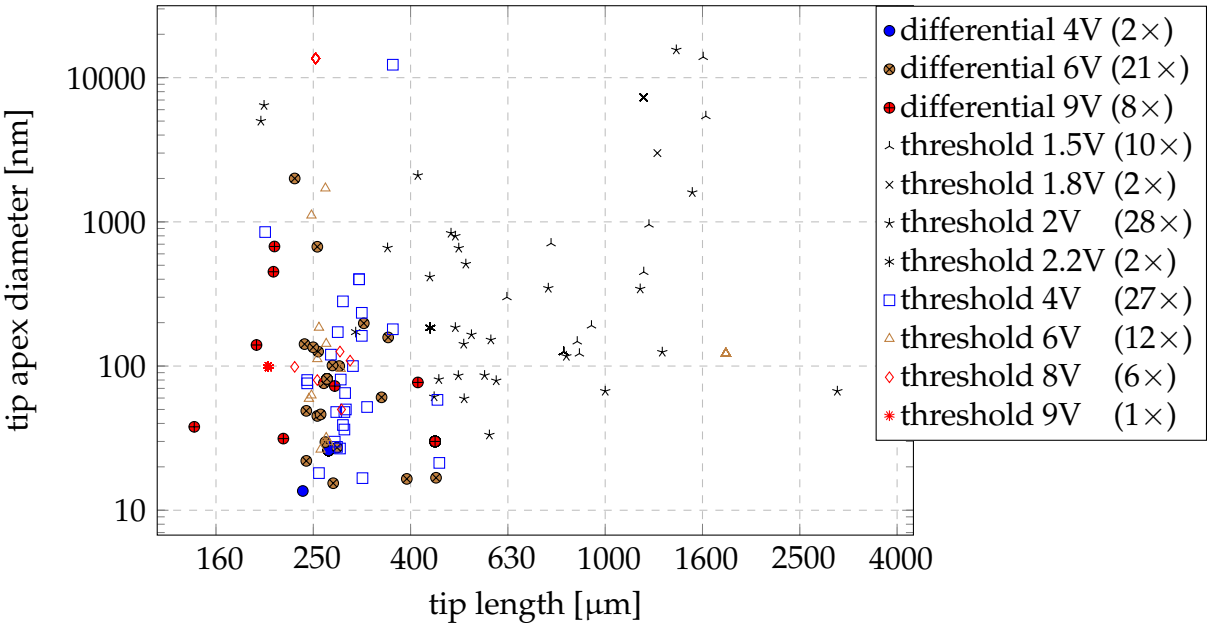


**Figure 3.15:** Tip apex diameter versus tip length for different etching modes and voltages. Higher etching voltages ($\geq$ 4 V) tend to produce shorter and sharper tips.

Figure 3.15.

The fractions of tips from Figure 3.15 with a apex diameter below 100 nm are listed in Table 3.2 for different etching voltages. Tips which are etched at 4 V and above have a

higher probability to be sharp than tips at lower voltages.

**Table 3.2:** Summary of the influence of the etching voltage on the tip apex diameter. The etching voltages 1.8 V, 2.2 V and 9 V for threshold mode etching are not included in this table as only 2, 2 and 1 tip was imaged by SEM respectively. Only tips that have been characterised with SEM are included in this table.

| etching mode and voltage | number of tips | fraction of tips with an apex diameter below 100 nm |
|---|---|---|
| threshold 1.5 V | 10 | 0 % |
| threshold 2 V | 28 | 32 % |
| threshold 4 V | 27 | 63 % |
| threshold 6 V | 12 | 50 % |
| threshold 8 V | 6 | 50 % |
| differential 4 V | 2 | 100 % |
| differential 6 V | 21 | 57 % |
| differential 9 V | 8 | 63 % |

However, the probabilities in Table 3.2 are only based on the tips that have been characterised by the SEM which are 119 of the 329 tips made in total during this study. For about every eight tip it could be seen by eye or optical microscope that the tip etching failed and these tips have been sorted out before any further characterisation was done. But this also depends on the etching setup. With the new beaker used as described in Section 3.2 none of the 20 tips etched failed this test. But not all tips that have passed this optical test have been tested by SEM due to limited access to the instrument. These tips have been characterised by the field emission test described in Section 3.3.3.1 or directly in the SPELS instrument.

### 3.2.4 Cleaning of etched tungsten tips

The sublimation of $WO_2$ starts at 1075 K [87] while tungsten melts at 3695 K. The annealing of a freshly etched tip is therefore a simple way to remove the tungsten oxide. At the beginning of my project, this has been done by the resistive heating method in a tip holder in the suitcase of the SPELS system. The tip holder allowed contact between the wire of the tip and a 0.5 mm tungsten wire to be made. A constant current between this point of the wire and the base of the tip holder can be applied. The heat produced by the current dissipates to the tip apex and removes the tungsten oxide. The duration of annealing and the amount of current used are crucial for this preparation method as the tip apex can become blunt at high temperatures [88]. After the annealing step, the suitcase has been vented, the tip was removed and loaded into the load-lock of the SPELS system.

## 3.3 *In situ* Tip Conditioning Stage

When this project started, tips were etched, annealed by resistive heating as described in the previous section and tested in the SPELS instrument. As mentioned earlier, this approach often led to unstable and blunt tips. Unstable tips have high fluctuations in the FE current during a SPELS measurement which can lead to height variations that exceed the range of the Z piezoelectric scanner. Adsorbed molecules and atoms on the tip surface can move towards the tip apex and change the overall work function of the tip. The tip preparation method of annealing the tip in the vacuum suitcase and transferring it into the load lock through air is one likely source of contamination. To avoid contact with air after annealing and to allow additional cleaning procedures, a new *in situ* tip conditioning stage was designed and installed in the preparation chamber.

### 3.3.1 Design of the tip conditioning stage

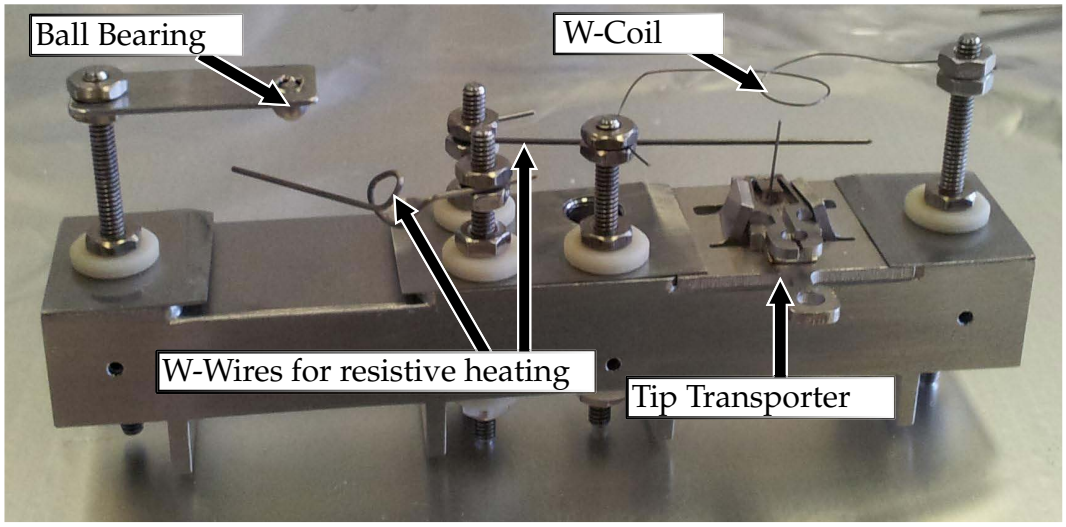


**Figure 3.16:** Tip conditioning stage with installed tip transporter. The stage is mounted to the chamber via a rod which is attached at the right side of the stage and electrically isolated by ceramic spacers.

The tip conditioning stage is shown in Figure 3.16. To be able to prepare a tip and transfer it to the STM head *in situ*, the stage was designed to accommodate Omicron style tip transporters which have the same dimensions as the Omicron style sample plates.

The stage has two slots for tips or samples. The possibility to park tips and samples in the second slot proved to be very useful. The tip transporter can be moved by the magnetic transfer arms in the preparation and the analysis chambers. Both slots have wires for direct heating. One slot has an additional ball above the tip while the other has a tungsten coil. The stage is isolated from the chamber and can be held at high voltage. The ball, the two wires for direct heating, both sides of the coil and the stage can be contacted directly from the outside. The high voltage is provided by a MicroLab dual channel power supply which can apply up to $\pm 6\,\mathrm{kV}$ with two channels.

### 3.3.2 Software controller for the tip conditioning stage

A LabView software has been written to control the MicroLab dual channel 6 kV power supply remotely and to analyse tip preparation parameters. The front panel of the control software is displayed in Figure 3.17. The software can set the current limit and

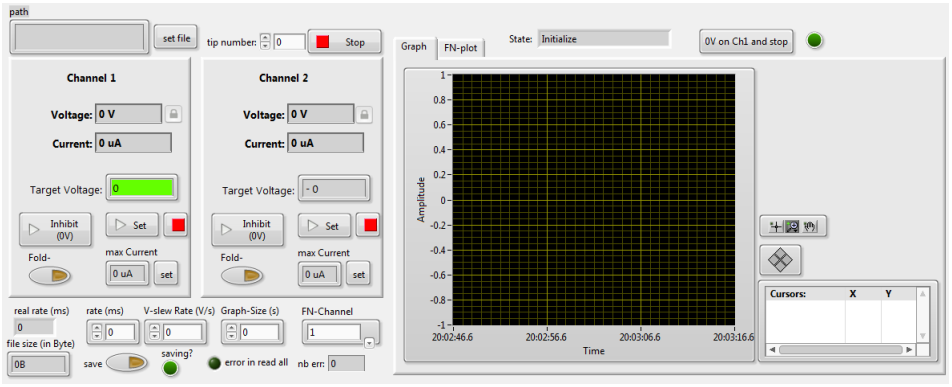


**Figure 3.17:** Front panel of the tip conditioning stage controller TPSControl v7.

voltage of the power supply as well as inhibit and foldback switches for both channels. To avoid unwanted tip changes the high voltage slew rate is limited in the program. The tips can be characterised using Fowler Nordheim plots as described in Section 3.4.1.2. Conditioning of the tips is done by raising the HV at the ball in front of the tip. The voltage plot time length can be adjusted. The data is also written into an output file to track improvements of the tips field emission capabilities. Such a plot is shown in Figure 3.20.

### 3.3.3 Tip preparation methods

The tip conditioning stage provides five different types of tip preparation techniques including the resistive heating method described in Chapter 3.2. It also allows e-beam heating, self-sputtering, field emission and field-surface-melting. Now follows a short summary of how these techniques are applied before their results are presented.

Resistive heating of a tip can be done in both slots of the stage. Tungsten wire with a diameter of 0.5 mm was used to contact the tip. After some initial adjustments to the wire touching the tip, the contact to the tips proved to be reproducible. The tips were flash annealed for 1-2 s while they glow with a bright orange colour using a direct current of 6 A. This step was repeated 4 times before the tip was degassed for 10 min using 3.5 A.

For e-beam heating, a coil is placed above the tip in one of the slots. The coil is made of 0.25 mm tungsten wire and produces thermally emitted electrons by resistive heating of the wire. The tip is then biased with a high positive field with respect to the coil. The thermal electrons accelerate towards the tip. As the strength of the field is largest at the tip apex, this region is heated maximally which removes the tungsten oxide.

The self-sputtering method is performed in the second slot where a ball bearing is placed above the tip. The uniform shape of the ball is used to apply a uniform field at the tip apex. The preparation chamber is then filled with argon and a high electric field is applied between ball and tip. The strong field at the tip apex can ionise argon atoms which are then accelerated towards the tip leading to a sputtering effect. This can lead to sharper tips, but an annealing step is necessary after the self-sputtering to heal the damage caused by sputtering [87]. The current induced by the positively charged argon ions can be used to monitor the evolution of the tip apex as a sharper tip would lead to a higher field, and therefore higher FE current, between tip and ball bearing.

Field emission as described in Section 1.3 can be done in both slots relative to either the ball or the coil. However, all field emission tests have been done using the ball as only it was connected to a SHV feedthrough.

If the tip is heated by direct current heating the surface atoms become mobile, an effect which is enhanced by an applied electric field and this is then called field-surface-

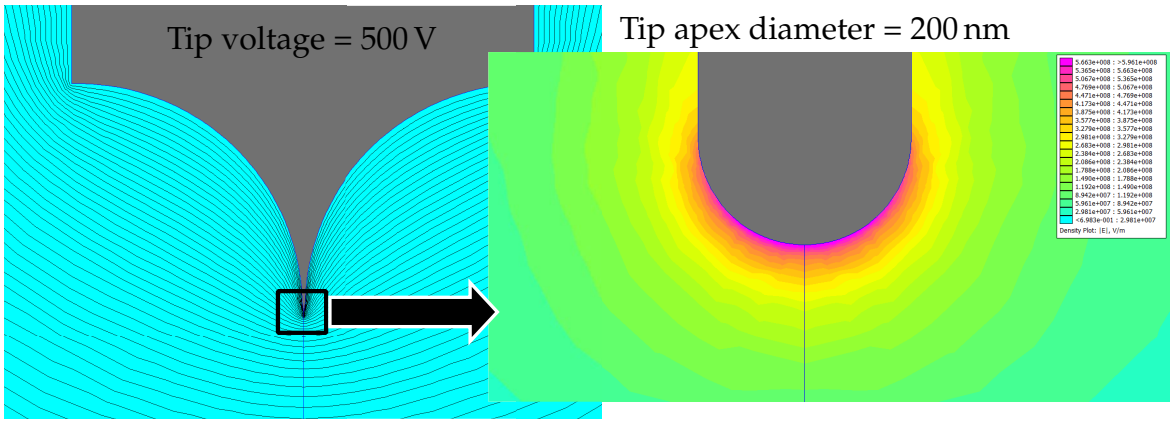


**Figure 3.18:** FEMM simulation of an STM tip made of 0.25 mm tungsten wire with an tip apex of 200 nm and an aspect ratio of 1. The tip was 5 mm away from the cathode and at a 500 V potential. The black lines in the left image are equipotential lines.

melting [89, 90]. This can be done by applying a high negative voltage to the ball above the tip at the same time as the tip is heated. This can cause surface atoms to move towards the strong field at protrusions on the tip, effectively building up a new sharp tip.

#### 3.3.3.1 Field emission

As SPELS works with an STM tip in the field emission regime it seems obvious to test the FE capabilities in the tip conditioning stage prior to SPELS measurements. To be able to assess how such a treatment could change the tip, electrostatic simulations were performed using the free software FEMM[1]. In this simulation the tip is 5 mm away from the cathode. Figure 3.18 shows the setup with an applied voltage of 500 V and a tip apex diameter of 200 nm. The highest field intensity of 0.06 V/Å is reached at the tip apex as expected. As mentioned in Section 1.3, field emission starts around 0.3 V/Å. Another mechanism that can happen is field evaporation where surface atoms are removed due to a high electric field. Field evaporation begins from 1 V/Å [91]. Other papers

[1]Finite Element Method Magnetics (FEMM) by David Meeker, version 4.2, see www.femm.info

suggest a more conservative value of 5.7 V/Å [92]. Figure 3.19 shows the maximum field intensity |E| for different tip voltages and apex sizes and a histogram of tip apex diameters of the tips characterised by SEM.

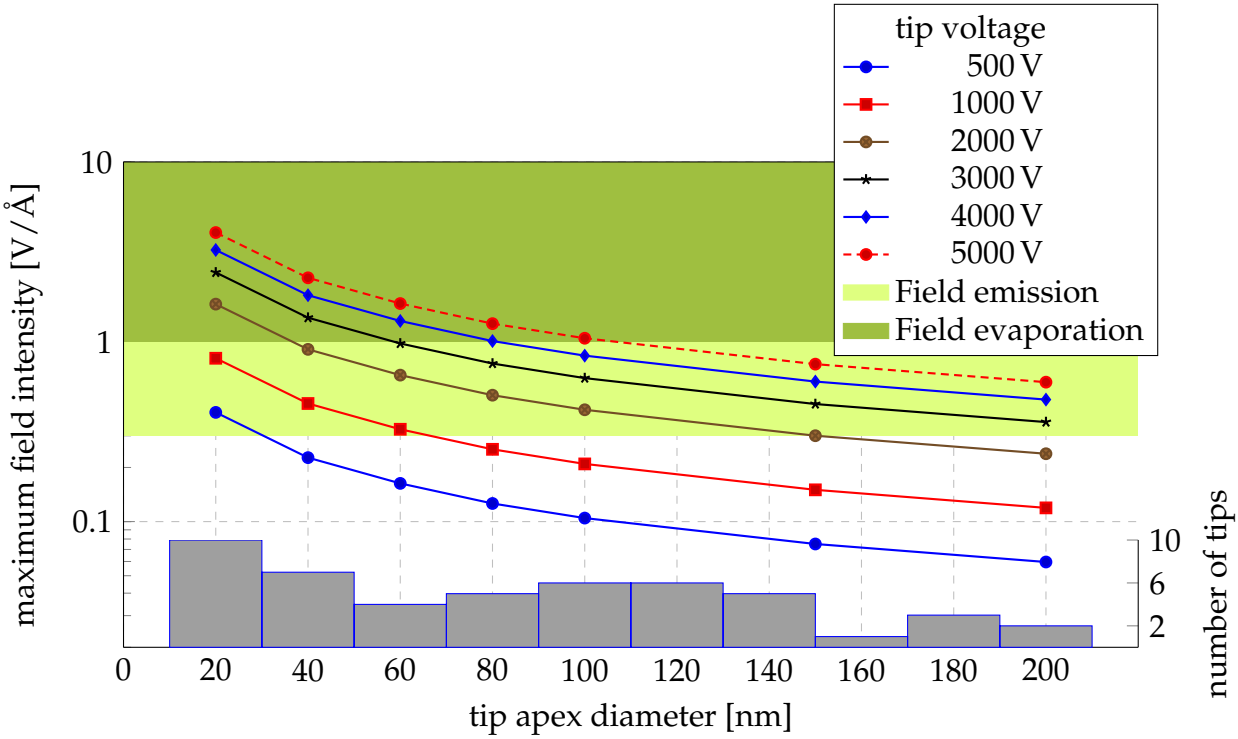


**Figure 3.19:** Maximum field intensities as simulated with FIMM for apex diameters from 20 nm to 200 nm are displayed for tip voltages of 500 V to 5000 V. The regions where field emission and field evaporation are possible are marked in the background. At the bottom of the graph is a histogram for tip apex diameters for all tips included in Figure 3.15 minus 15 tips which have apex diameters above 210 nm. The bar width is 20 nm.

The histogram in Figure 3.19 suggest that depending on the applied voltage it is possible that a freshly etched tip is not only field emitting but field evaporating.

However, one has to keep in mind that a freshly etched tip is still surrounded by a layer of tungsten oxide. transmission electron microscopy (TEM) pictures of the tungsten oxide layer can be found in reference [93]. Furthermore, the simplification of the tip being modelled by a hemisphere does not reflect the complicated structure some tips exhibit.

Field emission in the tip conditioning stage with freshly etched tungsten tips was usually performed in constant current mode. This can be done with the Microlab power supply by limiting the current and setting the voltage to maximum. Two examples of tips treated in this manner are presented below. Both tips (tip208 and tip209) have been etched from 0.25 mm tungsten wire with the differential etching method at 6 V at the same day using the same solution and the beaker described in Section 3.2.

Figure 3.20 shows the results of field emission on tip208. The tip was treated for 6 hours with emission currents of 1 μA to 5 μA. The voltage needed for 1 μA of emission current decreased from 4424 V to about 1000 V over this period indicating the improved field emission capability of tip208. Furthermore, the SEM images show a more compact tip but with a top that appears to have a rough surface.

Figure 3.21 shows a similar treatment for tip209. Here the field emission current maximum was set to 1 μA. The voltage decreased from 2271 V to about 600 V. The voltage graph shows short drops to zero at random intervals. These are are due to a bug in the communication interface of the power supply which enables channel inhibition at random times. The control software for this measurement (see Section 3.3.2) detects these drops and resends the voltage settings automatically. The SEM images show a reduction of the tip apex diameter from 174 nm to 80.3 nm. In this case the tip apex does not appear to be rough but the very top appears to be bend to one side.

#### 3.3.3.2 Field-surface-melting

Direct current heating has to be applied cautiously as a tip tends to become blunt when the tip begins to melt as described in Section 3.2.4. But if the tip is under the presence of an high electric field by applying a positive voltage to the tip the surface atoms are attracted by the local field gradient at protrusions on the tip [90].

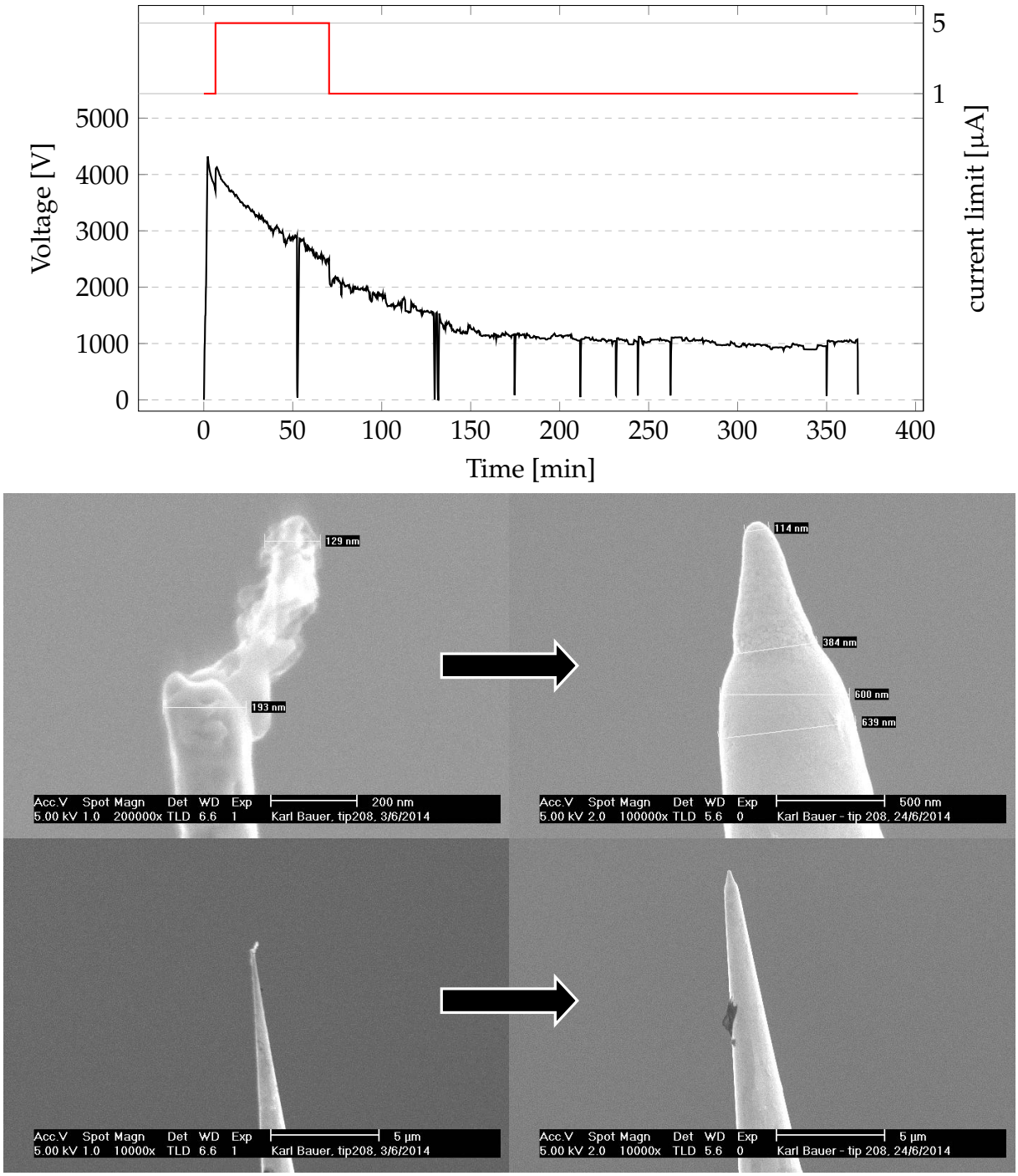


**Figure 3.20:** Applied voltage during the field emission of tip208. The current limit is displayed above the graph. The result on the tip is shown in the SEM images below the graph for two magnifications.

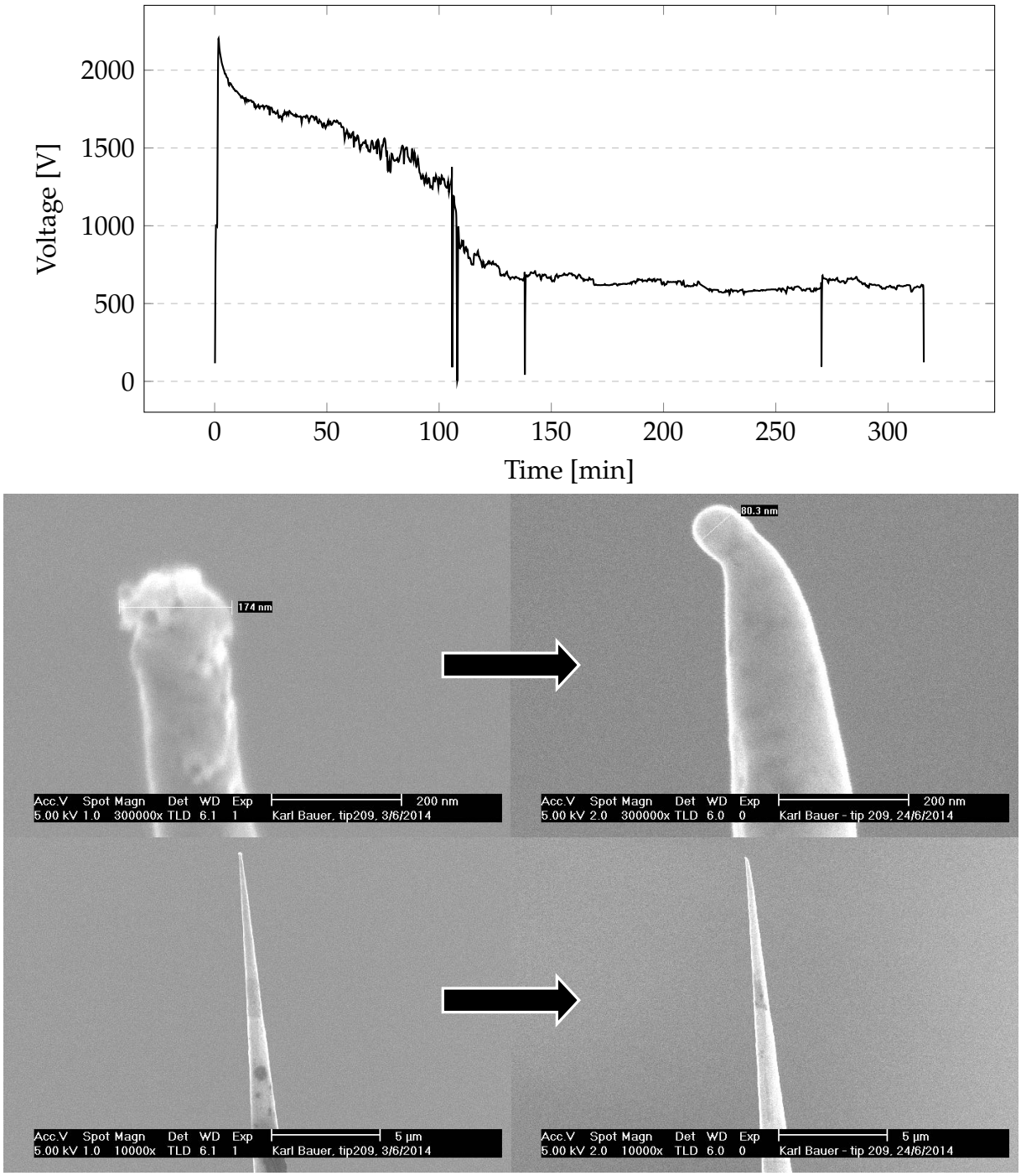


**Figure 3.21:** Applied voltage during the field emission of tip209. The current limit was set to 1 µA. The result on the tip is shown in the SEM images below the graph for two magnifications.

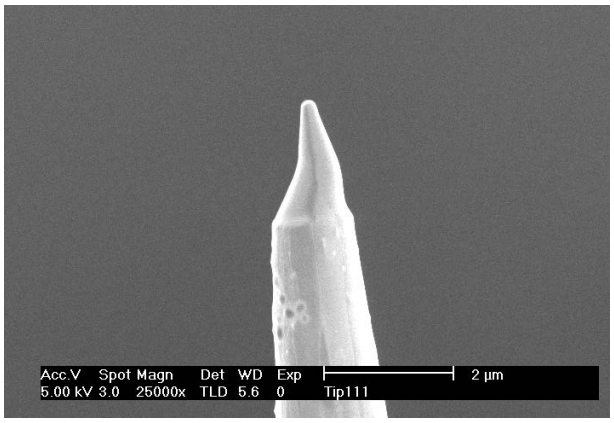


**Figure 3.22:** SEM image of a tungsten tip before it was used for field-surface-melting

The tip shown in Figure 3.22 has been treated in this manner. The first SEM image of this tip after etching showed a sharp but fragile tip with a diameter of 27.2 nm. Then it was treated at an emission current of 10 µA at 6 kV. The subsequent SEM image (see Figure 3.22) shows a smooth tip apex with a 226 nm apex diameter.

This tip showed only poor field emission of 0.12 µA at 6 kV applied to the ball. The voltage polarity at the ball was then changed by switching to channel 2 of the power supply and -2 kV were applied. This of course resulted in no field emission current. The tip was then annealed by direct current heating with 5 A and 3.7 V for 2 seconds. After this the field emission current at 6 kV at the ball measured again. Figure 3.23 shows the result of repeated annealing and field emission testing steps with increasing annealing time. Only the two first annealing steps of 2 and 5 seconds were performed at -2 kV. Thereafter the voltage was -4 kV. After the last annealing step of 60 s another 5 min of annealing at -4 kV was performed. After this step the current at 6 kV would have exceeded the safety limit and the power supply reduced the voltage accordingly. The current was limited to avoid tip melting during the characterisation process. The measured field emission current was 10.7 µA at 5.7 kV or 1.8 µA at 5 kV. The next annealing step of 5 min lead to 6.8 µA at 5 kV. As the last two steps are not directly comparable to the previous field emission tests at 6 kV they are not included in Figure

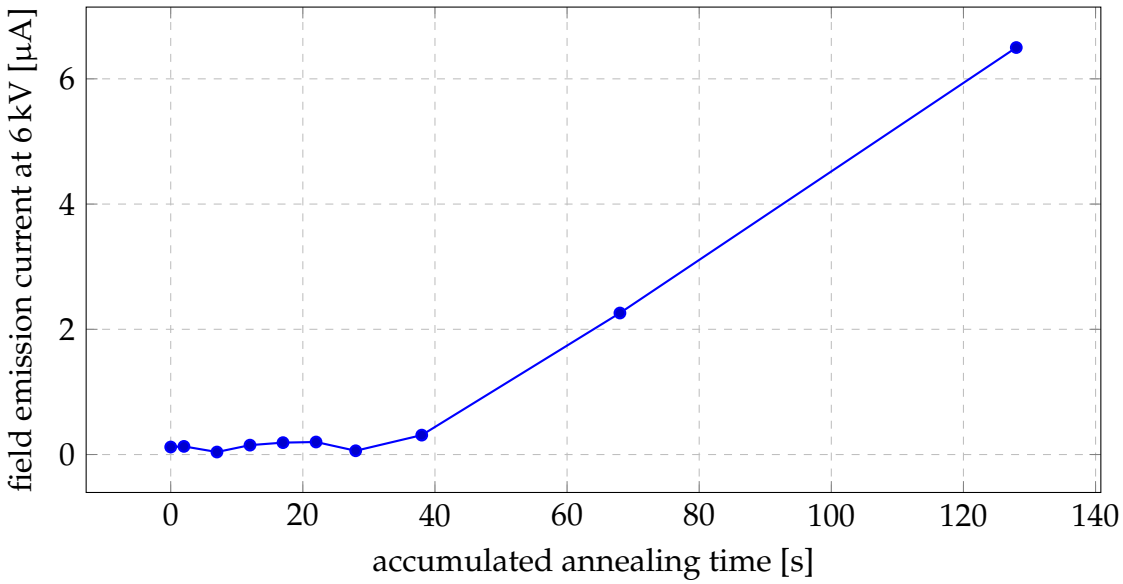


**Figure 3.23:** Field emission current tests at 6 kV between steps of field-surface-melting. The annealing time was increased for the last steps.

3.23.

In conclusion the field-surface-melting technique for build-up tips has been applied successfully. The exposure to annealing currents of 5 A for several minutes without an applied field would normally render the tip blunt but improves the field emission characteristics with the field. However, the process is time consuming and has not been used regularly in favour of the field emission treatment.

#### 3.3.3.3 Self sputtering

Self sputtering has the advantage that a characterisation of the tip can be done by field emission at the same time. However, the Argon used as the sputtering gas has to be pumped out of the system before the tip can be transferred to the analysis chamber. The sputtering ions create a neck below the tip apex which after sufficient time will decapitate the tip [94]. This event should be visible as a drop in the FE voltage needed for 1 µA. This method has been applied at an Argon pressure of $1.3 \cdot 10^{-6}$ mbar and

a fixed current of 1 μA. However, the method increased the applied voltage needed for 1 μA (e.g. from 800 V to 1520 V) and no decapitation of the tip was observed. It is possible that the tip shape of the tips used with this method was not ideal (e.g. bent). The success of the field emission method, which allows to load a tip directly into the STM after preparation has finished, meant that this method has not been tested with a great number of tips.

#### 3.3.3.4 E-beam heating

E-beam heating was used with a filament current of 3 A to produce thermally emitted electrons above the tip. The high voltage had to be applied to the tip and therefore the whole stage. It was set to maintain a constant current of 1 μA and reached 2-2.5 kV producing a heating power of 2-2.5 mW. The tip was characterised by the field emission test before and after e-beam heating. The voltage needed for 1 μA decreased from 1600 V to 1100 V.

### 3.3.4 Summary

In summary, it has been demonstrated that the tip conditioning stage can be used for a variety of tip preparation methods. The characterisation of tips by the field emission test has been very useful and time-saving. Not all preparation methods have been optimised and applied to a great number of tips. Field emission has been used as the standard method for tip preparation and characterisation before SPELS measurements with great success. Tips with a stable FE voltage below 1000 V at 1 μA in the tip conditioning stage generally show a high count rate in SPELS.

## 3.4 Software Developments

At the beginning of this project, the electron analyser and optics could not be controlled by the SPELS imaging program, which was written in LabView. Therefore the program was updated. A new method for setting the lens voltages of the MCA was added which is explained in the following section. The Fowler Nordheim part was extended and a new segment for detector calibration was written. The data handling was revised to allow high count rates with the MCA to be measured. Additionally, a data processing software package specifically for SPELS data was written in Matlab[1] and in LabView. These programs are discussed in Section 3.4.3.

### 3.4.1 MCA controller

#### 3.4.1.1 Setting up Lens Voltages

The Nanonis program suite provides LabView programs for reading and setting all available parameters including the FE-voltage, FE-current and piezo voltages but has no access to the electron lens voltages since they are set by the proprietary LK program. In order to control the lens voltages from the LabView SPELS program, the electronic signals which are generated by the LK program had to be analysed. Therefore the analogue signals generated by the program and the installed Keithley KPCI-3140 DAC-card are monitored by a National Instrument PCI-6602 DAC-card and a LabView program has been written to record and interpret the signal as a bit stream. The signal was monitored in parallel by an oscilloscope to get accurate readings of the time intervals of the signal. The diagrams of the LK electronics show that the signal is processed by three 8-bit shift registers in series indicating a 24-bit long serial signal which is transformed to a parallel signal in the B17 and A15 cards. This was confirmed by the

[1] by the summer student Carl Branbury under my supervision

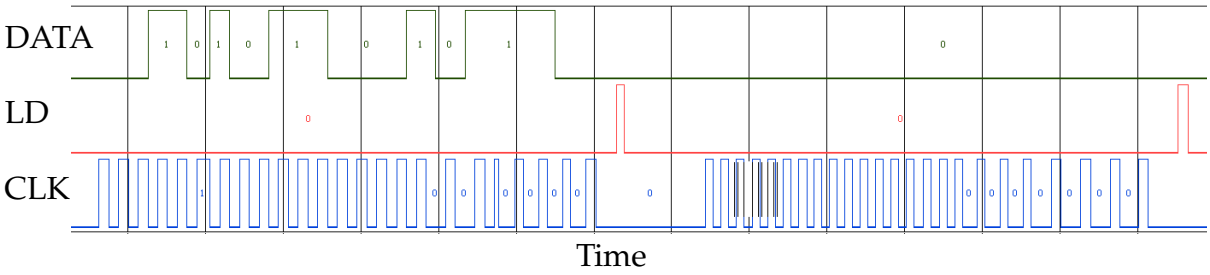


**Figure 3.24:** Serial signals consisting of the DATA, LD and CLK signal. This signal sets one virtual voltage.

structure of the clock (CLK) and load (LD) signal which is shown in Figure 3.24. After 24 raising edges in the CLK signal, an LD signal sends the information to the next parts of the electronics. This signal is followed by a signal of the same length which sets the shift register values to zero.

The LK signal sets 18 virtual lens voltages rather than the actual lens voltages. The voltage is represented by an integer number called "DAC". The DAC value can be calculated from the virtual voltage by a linear equation. The coefficients of the equation for each of the virtual lens voltages are stored in the file DCAL.INI. The virtual lenses are identified by an ID number. The range of values for DAC numbers and lens voltages, and the IDs of the virtual lenses, as well as the coefficients of the conversion formula are listed in appendix B. The conversion formulae for the 18 virtual voltages to the 12 actual voltages are also in the appendix.

By changing the values of different virtual lens voltages in the LK program and recording the signals, the first 16 bits could be identified as the binary representation of the DAC number starting with the least-significant bit. The last 8 bits represent the ID of a virtual voltage and therefore determine which virtual voltage is changed.

The existing LabView SPELS program was extended by a subroutine to set the lens voltages which is shown in Figure 3.25. This program was tested successfully and replaced the LK program. It gives the user the possibility of quickly changing the lens

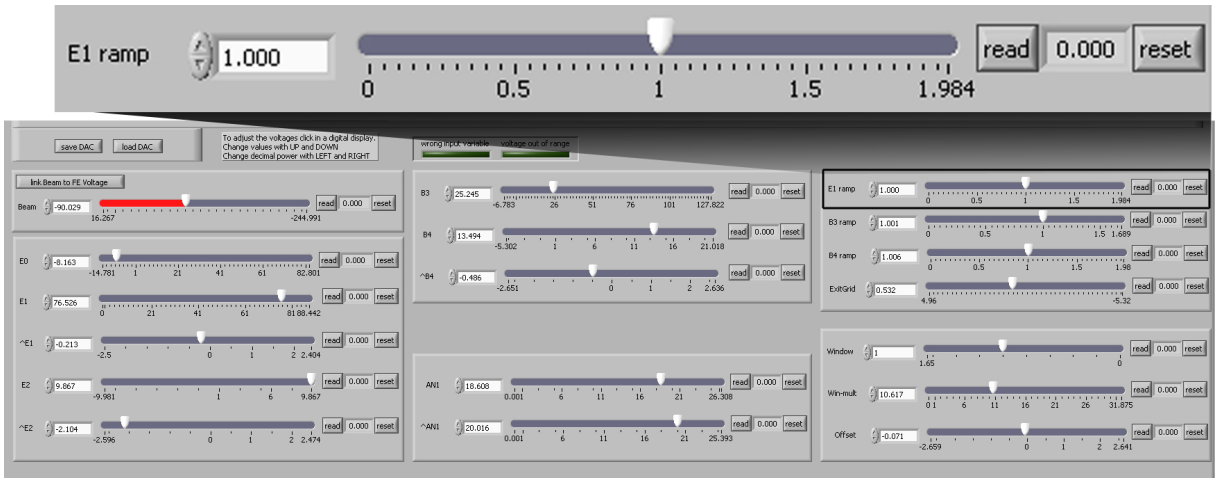


**Figure 3.25:** LabView front panel for the electron lens voltage setup. Each slider represents a virtual lens voltage.

voltage settings and saving and loading DAC files which store a complete lens voltage set-up. One disadvantage with the LK program was that the speed with which the lens voltages could be changed was quite slow. To find the optimum parameters faster, the new subroutine presents a slider for each virtual lens voltage which represents the full energy range of the lens. Fine tuning can be done by adjusting the numerical values with the arrow keys on the keyboard. For each voltage a quick store and reset function is implemented. The "Beam" voltage also has a function which locks it to the FE-voltage as this is the standard value. The lens voltages are stored internally in a global variable and are therefore accessible from any other part of the LabView program.

#### 3.4.1.2 Fowler Nordheim Plot

The Fowler Nordheim plot, as described in Section 1.3, gives a rough estimation of the tip apex radius and is used to perform a first characterisation of the quality of the tip. The existing subroutines for recording a Fowler Nordheim plot have been extended by the possibility to directly calculate the estimated radius from the slope of the plot. All values of Equation (1.22) can be set manually. The typical value used for the effective

work function of tungsten tips is 4.5 eV which takes into account the three different work functions for the three facets of tungsten occurring at the tip in favour of the lowest work function as the field emission increases exponentially with the work function [87]. The image correction factor is normally set to unity. Two values can be set for the field reduction factor which leads to an upper and lower estimation of the tip apex radius.

#### 3.4.1.3 Detector Calibration

A new subprogram, called by the existing LabView SPELS program, uses the analyser voltage "AN1" to calibrate the detector. The "AN1" voltage shifts the electron position at the detector by the same amount as the analyser separates the electron trajectories (as explained in Section 2.3). The previously calibration method using the FE-voltage is also implemented in a subprogram, and the main program includes the front panel of one of these subprograms in its own front panel, as shown in Figure 3.26. This allows the SPELS program to switch between the calibration methods with a minimum of redundancy in the code. The settings for the calibration method are the voltage shift (either in the FE voltage or in the "AN1" voltage), the number of spectra to be taken, the acquisition time for each spectrum, and the latency time for setting the voltage. The spectra are sequentially displayed as a point graph and the ($V_{FE}$, $V_{MCP}$) or ($V_{AN1}$, $V_{MCP}$) data points are drawn. After the last spectrum, the coefficients of the polynomial fit are calculated. The user can decide if these values should be used by copying them into the global variables for the coefficients which are used by the program Grid_SPELS.

Both calibration methods are applied to a measurement with a sharp tungsten tip on an electrically contacted thick gold layer evaporated on mica. The results are shown in Figure 3.27. The calibration "FE - 1" and "AN1 - 1" are taken before a tip change occurred leading to a reduced effective work function for the "FE - 2", "AN1 - 2" and "AN1 - 3" calibration.

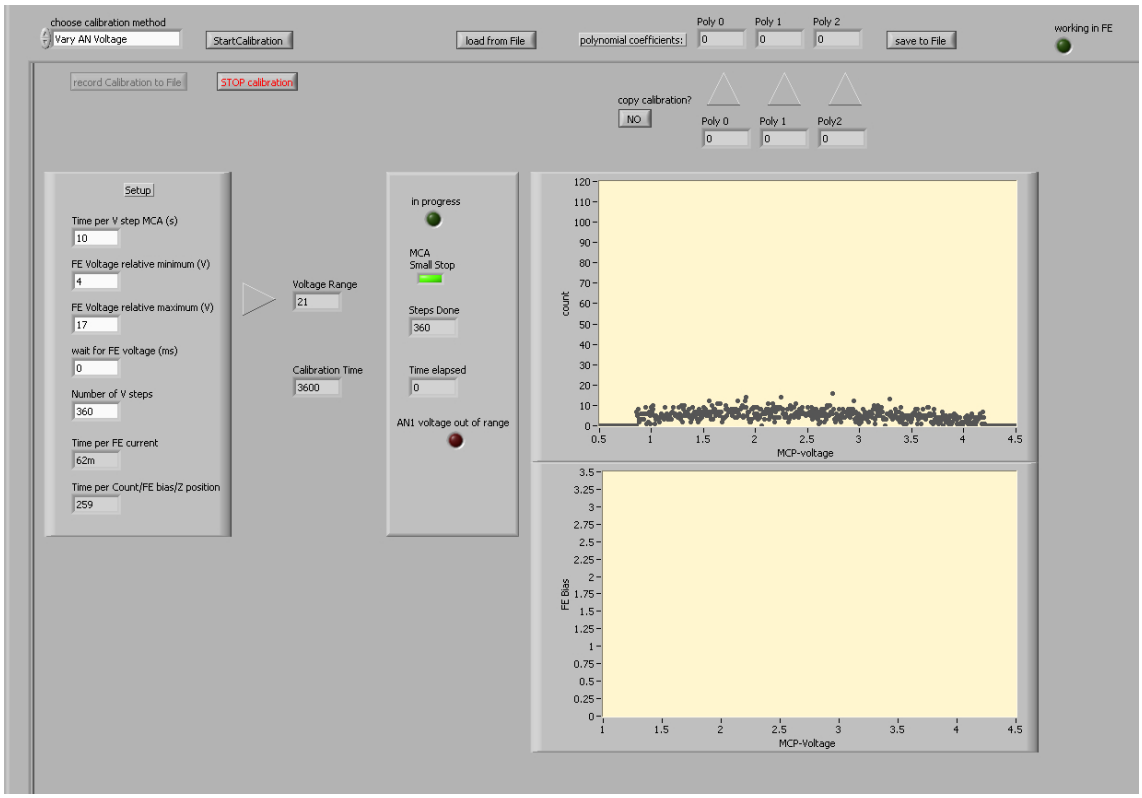


**Figure 3.26:** LabView front panel for the calibration of the detector using the "AN1" voltage of the analyser.

### 3.4.2 RFA controller

The difference in the working principle between the MCA and the RFA requires a new fork of the SPELS control software. The RFA measures the total energy of the electrons directly by producing a known energy barrier before the detector. Therefore it is not necessary to calibrate the RFA as it was for the MCA. However, a method to find the best working point for the RFA had to be added. For this a remote control of the high voltage power supply has been set up and a sweep function for this voltage has been written (see Figure 3.4).

Spectra are recorded by sweeping the retarding voltage over the desired energy window and then differentiating the resulting count rate plot (see also Section 3.1.1). The energy loss range, position and step size and time can be set. The first 3 eV below the tip

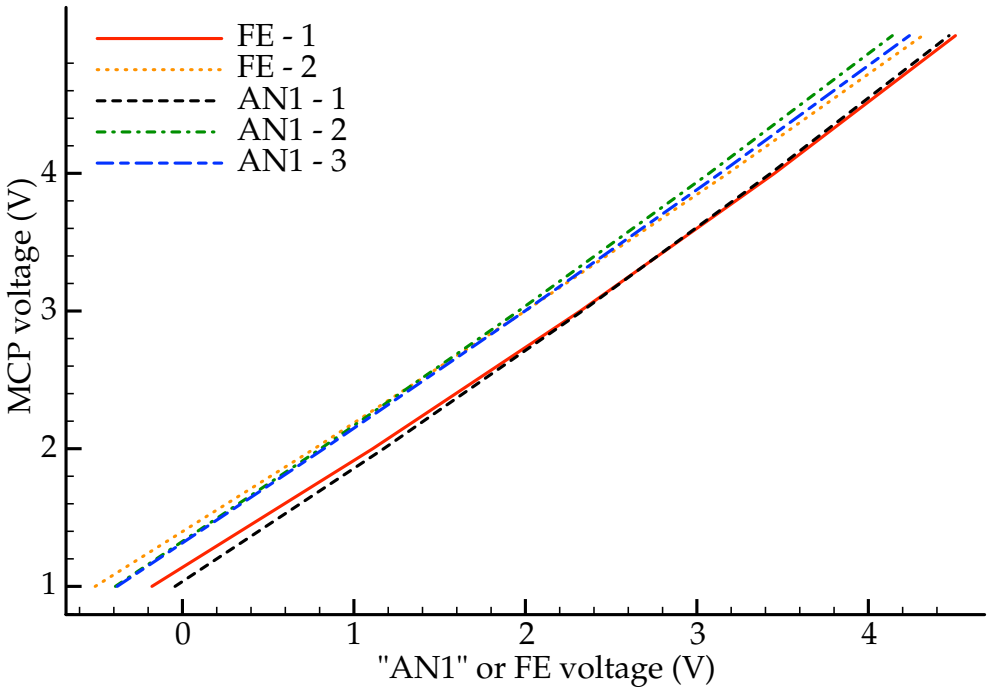


**Figure 3.27:** Direct comparison of the polynomial conversion formula for the calibration methods using the "AN1" or FE voltage. The coefficients of these formulae were obtained using the new calibration method. Note that a tip change occured between the calibrations "FE - 1", "AN1 - 1" and the rest of the data.

potential are usually skipped as the maximum electron energy is reduced by the work function of the tip. The software automatically calculates the differential spectrum for each energy point. It is also possible to apply a Butterworth or Savitzky Golay filter to the spectrum in real time. A spectrum can be saved to a text and XML file and also copied to a separate graph in the software to analyse and compare it with other spectra.

The RFA can be operated in pulse counting mode and analogue mode which are explained in Sections 3.1.3.1 and 3.1.3.2 respectively. The software allows to use both modes with the same frontend by a central “CR electronic” switch. The software either takes the signal from the analogue output signal from the ratemeter (pulse counting mode), the RS232 interface of the picoammeter (analogue mode) or from a simulation (for testing and presentation purposes).

New experiments can be integrated into the software by using the SubPanel container in LabView. This has been used to plot the count rate against time or sample movement and the analogue mode output current against CEM high voltage, retarding field voltage or sample movement. The plot of the signal against sample movement was used to find structures on the sample by laterally moving the sample and looking for signal changes due to the chemical contrast of SPELS. The movement is stopped when the FE current exceeds a threshold value. The Omicron MSCU controller which is moving the sample has only one remote channel. Therefore the two possible dimensions of sample movement (lateral or approach/retract) can only be chosen manually.

The CEM is exposed to all electrons with energies higher than the retarding field strength. To avoid reducing the lifetime of the CEM unnecessarily by a high input signal the retarding voltage of the RFA is linked to the FE voltage of the tip and only changed by means of changing the difference between these two voltages. Without this safety measure the CEM might easily be exposed to high input signals when the tip voltage is ramped up or changed between measurements.

#### Grid SPELS program

The SPELS images are created by the Nanonis program using a custom LabView user program called "Grid_SPELS". This program had to be rewritten for the RFA. The energy window, scan step size and timings can be chosen. The program calculates the differential spectra and saves the data using the same Nanonis sxm file framework.

### 3.4.3 SPELS Image Processing

One SPELS measurement produces a set of parameters such as FE current, count rate and spectrum for each point of a two-dimensional virtual grid on the surface of the

sample. It is not possible to provide a single representation of all of this data, but it is instead necessary to extract different kinds of spatial maps and spectra. To reduce the noise in images of the spatial distribution of energy loss features, the average over an energy range around the expected loss feature for each point of the grid should be calculated and assembled into an image. To increase the dataset for a characterisation of a certain energy loss peak in the spectra, the sum of the spectra in a certain subarea should be taken and presented as a spectrum. Also further data processing techniques, such as background subtraction, are desirable.

The data generated by the Nanonis program, using a LabView subprogram called Grid_SPELS, for a typical image of 30 by 30 pixels consists of 900 data arrays and general information about the measurement, such as the used FE voltage and the date. One of these data arrays stores the position of the pixel, the measured FE current, the total count rate and the count rate for 500 energy loss ranges. The data is stored in a proprietary binary file format called 3ds (not to be confused with the Autodesk file format).

The Nanonis program "Binary File Inspector" opens the file and shows spatial images for each of the 500 energy loss ranges, the current, the integrated count rate and the topography map. It also shows the individual spectrum for each pixel. It can not calculate averages of energies, spectra or regions. The Nanotec program WSxM, which was used to process the AFM and STM images shown in this thesis, opens the file format but shows only count rate maps for 60 non-user-definable energies [95, 96]. Gwyddion cannot open the file format [97]. SPIP opens the file but shows only two images with no information about the displayed data [98]. The lack of existing editor programs regarding SPELS data led to the decision to start the implementation of a new program which should satisfy the requirements mentioned above.

To improve the data processing after SPELS measurements, a Matlab program was

written[1]. This program allows the production of spatial maps of the count rate of backscattered electrons in a certain energy range. This provides spatial plasmon loss images of higher quality because it also averages over noise in the channels included in that energy range and therefore increases the signal to noise ratio. In turn, the spectrum from single pixels or averaged spectra from certain areas can be taken. The spectra can also be normalised against the maximal value in each of the spectra respectively. Images taken from normalised spectra consider the variations of the total backscattering probability from different materials. Also the subtraction of spectra from different regions and image processing techniques like a Gaussian blurring are possible. The ability to generate images of various energy ranges in seconds makes this program a valuable tool for SPELS data processing. Before this program was developed, plasmon images were produced by exporting the spectra for each pixel individually into Matlab and combining the relevant information into a matrix. This time consuming task can now be done in seconds.

With the new RFA analyser the dataset included in the 3ds files changed and the program needed to be amended. As the main SPELS program also uses LabView, additional LabView programs have been written to display the data contained in 3ds and sxm data files. The 3ds viewer also produces count rate maps within a selectable energy window, and displays all measurement parameters. The images can be normalised by linear and polynomial fitting and exported as an image. Furthermore, programs to display and process energy loss spectra from both the MCA and the RFA have been written.

[1]written by Carl Banbury under my supervision as part of the summer student programme 2011 at the University of Birmingham.

# Chapter 4

# Creation of Nanostructured Surfaces

## 4.0 Perspective

SPELS can provide spatial maps of EELS spectra and therefore of surface excitations like surface plasmons. Of course, there is little gain in this compared to traditional EELS spectra if only homogeneous samples would be used. It is necessary to have a structured sample on the nano-scale to evaluate the performance of the instrument. Nano-plasmonics and metamaterials are research topics of considerable interest [99, 100]. The possibility of SPELS to compare EELS maps with STM data is interesting and can potentially add valuable information to these fields of research like the dependency of plasmon properties on thickness and surface structure.

The first results taken with this instrument were on Ag on HOPG samples as described in Section 2.4 with a rather random distribution of Ag islands and island sizes. The possibilities of *in situ* sample preparation were limited by the lack of control of the evaporation rate with the existing evaporator design. Therefore a new evaporator was assembled and installed in the preparation chamber as described in Section 4.1. The new evaporator improved control over evaporation rate and therefore sample properties. However, it is desirable to have the ability to fabricate reproducible nanostructures for SPELS measurements.

It is also necessary to have these nanostructures cover a macroscopic area as the lateral sample movement is restricted to the horizontal axis (see 2.2). The distance between two structures should not exceed the image size but be within 1-2 μm. Therefore, electron beam lithography (EBL) was employed to produce Ag and Au nanostructures as described in Section 4.2. EBL utilizes a focused electron beam to chemically alter a resist, changing the solubility of the exposed resist in a developer. The metal deposition of the developed sample was done using the evaporator described in Section 4.1. Although it is not a standard substrate for EBL, HOPG was chosen as the substrate for all nanostructured samples, as it was used in previous studies of SPELS.

## 4.1 Evaporator

The EBL technique described in Section 4.2 requires precise control over the evaporation rate of metals as not only the thickness of the resist is limited but also the morphology of the structures depend on it [101, 102]. Therefore a new evaporator as shown in Figure 4.1 was built. The parts were manufactured by the mechanical workshop of the Physics and Astronomy School and Scanwel Ltd[1]. The evaporator has been assembled and installed in the preparation chamber. The evaporator consists of a DN40 flange with four electrical feedthroughs, two stainless steel tube feedthroughs and a connected stainless steel tube which holds a DN16 flange at the air side. The stainless steel tubes support a copper cooling cylinder which is connected to ground through the tubes. The evaporation material is placed in a tantalum crucible which is situated in the copper cylinder below a 5 mm wide and 25 mm long aperture. Assuming a 3 mm wide crucible 5 mm below the aperture then the width of the evaporation spot is

$$d_{spot}(l) = 2\,(18.75 + l)\tan\left(7.5946^{\circ}\right) \tag{4.1}$$

[1]Scanwel Ltd, Llandderfel, Bala, Gwynedd, UK LL23 7HW; www.scanwel.co.uk

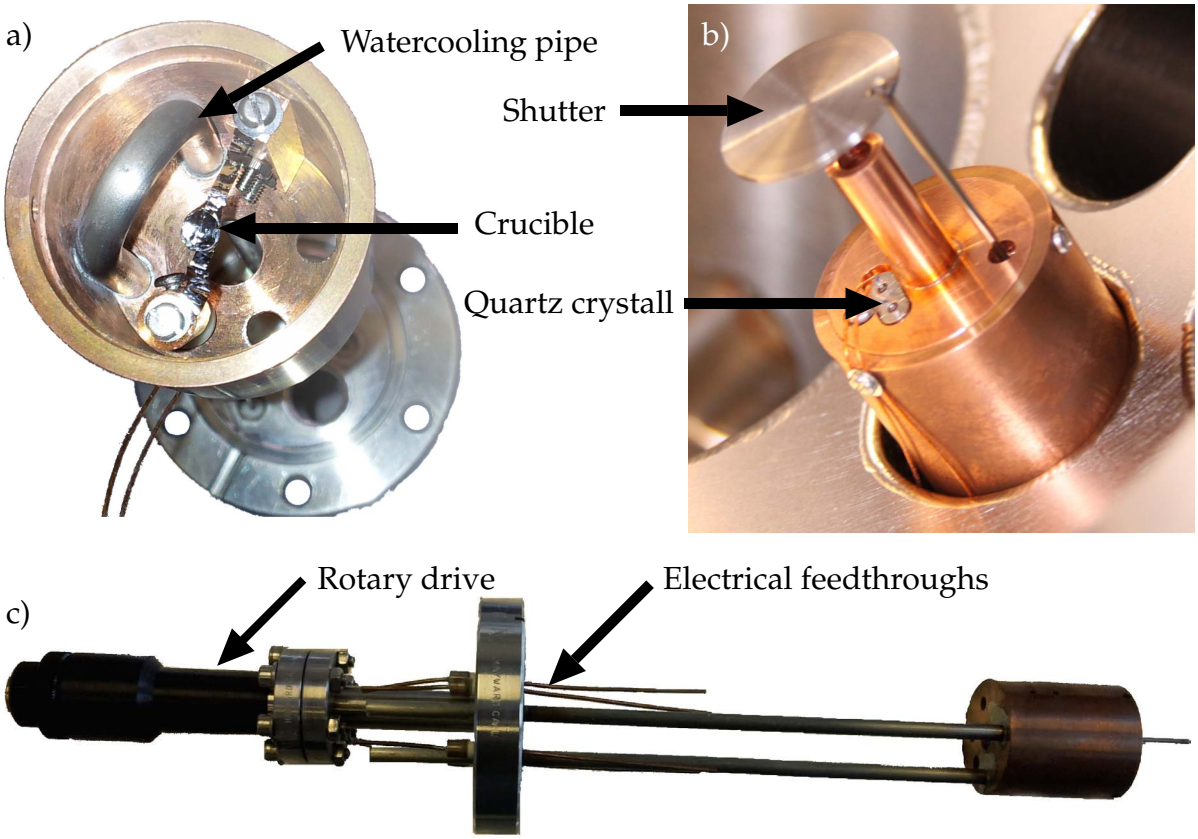


**Figure 4.1:** Photographs of the new evaporator without detached nozzle (a), installed in the preparation chamber (b) and in side view without wiring or shutter (c). The crucible is placed inside a copper shield which is held by the watercooling pipes. The shutter is controlled by the rotary drive.

where $l$ is the distance between aperture and sample in mm. The derivation of this equation can be found in the appendix A. The sample is about 50 mm away from the aperture. The expected diameter of the evaporated area at the sample using equation 4.1 is about 18.3 mm.

The material is evaporated by resistive heating of the crucible. The copper cylinder also contains a window for a quartz crystal which is used to monitor the material flux from the crucible by measuring the film thickness on the quartz crystal. The crystal is connected to two of the four electrical feedthroughs. The copper crucible is cooled by water which flows in the stainless steel tubes. This is necessary to have

a stable monitoring from the quartz crystal, a reproducible crucible temperature and to reduce outgassing of the evaporator parts. To control the evaporation rate at the sample a shutter is placed above the aperture, which is moved by a manual rotary drive connected to the DN16 flange. The crucible is supported by a small copper cylinder which is connected to one of the four electrical feedthroughs and by a small copper block which is directly attached to the inner wall of the hollow copper cylinder and therefore connected to ground.

The evaporation rate at a current of 7 A and a voltage of 2.2 V is 2 ML/min[1] at the sample. This rate was determined with the method described in [103] and the help of Dr. Lin Tang.

The spare electrical feedthrough can be used to change the heating method to e-beam heating by installing a metallic coil. This coil produces thermal electrons by resistive heating. A high voltage is then applied between the coil and a rod of the target material or a crucible with the target material. The thermal electrons are accelerated towards the target material and heat it up.

This new evaporator allows precise control of the deposition rate and the amount of deposited material on the sample. This is not only necessary for the EBL samples but also for the deposition through a mask such as a quantifoil grid. This could potentially produce a regular pattern of silver islands on any substrate over a large area. The initial attempt was done using the old evaporator described in Section 2.4. It was used to evaporate silver through a quantifoil grid on HOPG. An AFM image of the sample and a SEM image of the grid after evaporation are displayed in Figure 4.2. The lack of control over the evaporation rate makes it difficult to produce samples with a regular structure showing both substrate and metal layer using TEM grids as a mask. In this case, the amount of evaporated silver was too high. On the other hand, the feature size

[1] ML = monolayer

① AFM image of HOPG sample after Ag evaporation

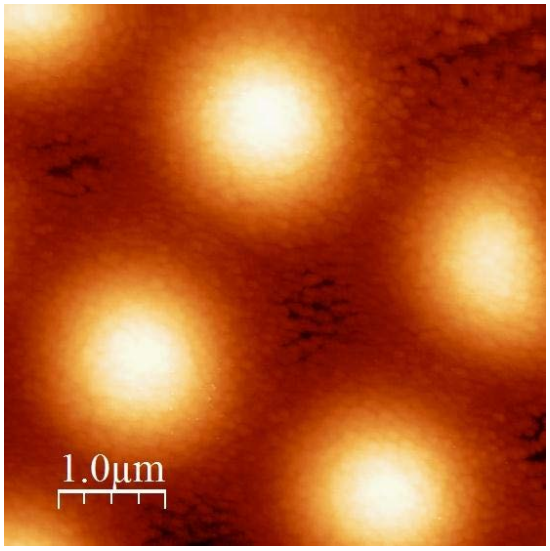


② SEM image of quantifoil grid

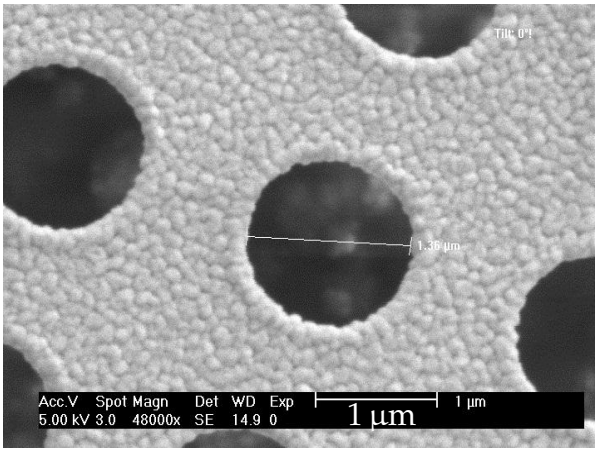


**Figure 4.2:** ① AFM image (tapping mode) of Ag evaporated through a quantifoil grid on HOPG by the old evaporator. The silver spreads underneath the grid due to the high amount of evaporated material. ② SEM image at 5 keV of the grid after evaporation. The holes in the quantifoil are still open which allows the grid to be re-used.

has to be similar to the scan range of the STM, limiting the maximal hole size and the maximal gap between the holes in the grid. Therefore, it is necessary to have more control over the evaporation process in order to reduce the amount of evaporated silver.

The new evaporator was used to repeat the evaporation through a quantifoil grid. An AFM image of the sample is shown in Figure 4.3. The sample was evaporated for 15 min at an evaporation rate of 2 ML/min. At this evaporation rate the HOPG substrate is still visible between the Ag islands.

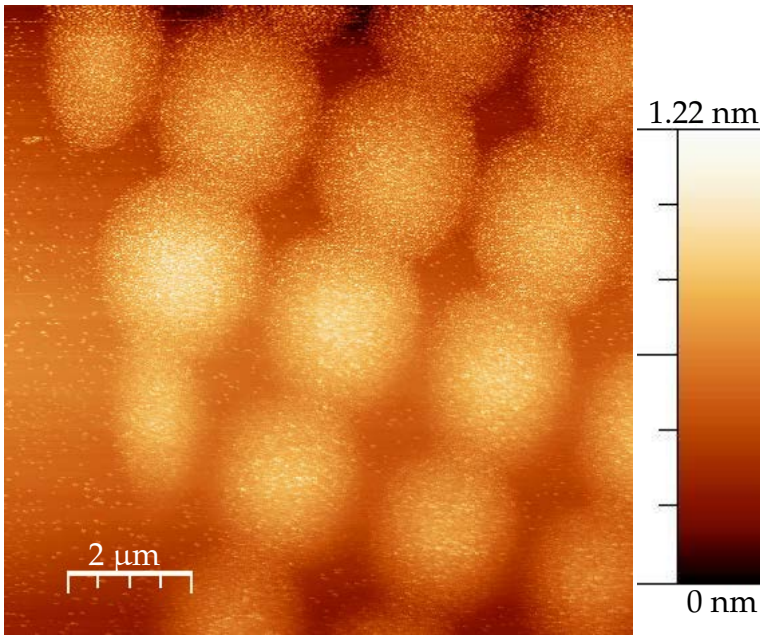


**Figure 4.3:** AFM image of silver islands on HOPG evaporated through a quantifoil grid using the new evaporator. The evaporation time was 15 min at a current of 7 A and a voltage of 2.2 V with an expected evaporation rate at the sample of 2 ML/min. The sample was not annealed.

## 4.2 Electron Beam Lithography

### 4.2.1 Method

There are a number of EBL resists, with or without photosensitivity, available on the market. The positive resist SML-100 from EM Resist Ltd [104] has been used with a (1:3) mixture of methyl isobutyl ketone (MIBK) and isopropyl alcohol (IPA) as the developer. The substrate was HOPG and a two-step spin coating process was used. The HOPG blocks had a size of (12x12) $mm^2$. SML-100 is tailored to produce a 100 nm thick layer at a spin speed of 5000 rpm and 125 nm at 3000 rpm. Before the application of the resist a fresh layer of graphite was exposed by using scotch tape to peel the top layers away. After 20 µL SML-100 was applied on the surface the spin-coater program was started with 500 rpm for 5 s and then 3000 rpm for 30 s. The sample was subsequently baked at

160 °C on a pre-heated hotplate for 3 min.

After the sample has cooled down, a scratch is made from an appropriate writing area near the middle of the sample to the lower left corner of it. This scratch has three functions. It produces debris near the middle of the sample which can be used to refocus the electron beam just before writing starts. Furthermore, it is an easy way to place the structures on the sample - for example on a particular flat area. It also helps to find flat structures later in a microscope like the atomic force microscopy (AFM), SEM or an optical microscope.

The HOPG sample and a Si calibration sample are then loaded on a sample holder and into the SEM. The calibration sample consists of a "chessboard" grating and nanospheres. The sample holder has a Faraday cup integrated in its rim. The SEM was described in Section 3.2.3.1. For lithography it is controlled with an EBL controller and software (ELPHY Quantum) from Raith[1]. After the SEM chamber was pumped down the electron beam current $I_{beam}$ was measured with the Faraday cup at the beam voltage of 30 kV for lithography. A typical value is 0.04 nA. There is no laser alignment or similar for the sample stage which means that there are stitching errors on the order of several µm when multiple writefields are written next to each other as shown in Figure 4.4. The bandwidth of the Raith controller is 16 bit or 65536 points for both dimensions. A 200 µm writefield has been used as a trade-off between minimal structure size with a minimal digital step size of 3 nm and less stitching boundaries. The 200 µm writefield must be aligned using the chessboard through a standard routine in the Raith software. Then the beam is focussed and astigmatism and beam shape are corrected using the nanospheres mentioned above.

In the next step, the working coordinate system is aligned using the lower right and left corner of the sample. This could in principle be used to find the middle of the sample

[1]Raith GmBH, http://www.raith.com

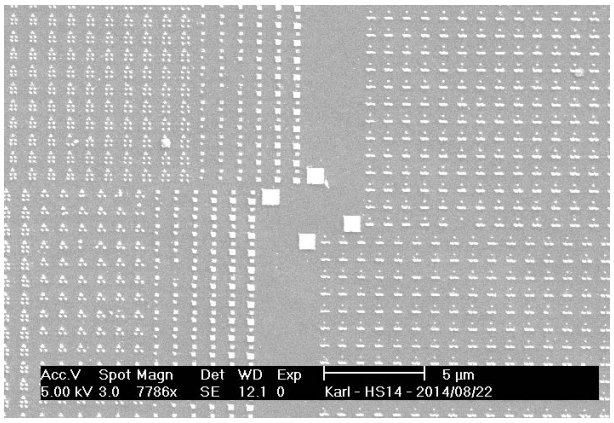


**Figure 4.4:** SEM image of sample HS14 showing stitching errors of 2-3 µm between four writefields. The big squares are 1 µm tall but should be aligned.

for writing but the middle is not always the best position on the sample. The next step is to trace the scratch from the corner of the sample to the end and focus the electron beam there again. During the whole time any exposure of the sample with the electron beam is kept to a minimum along the sample edges and the scratch. Then the array of writefields is set to start 500 µm above and to the right of the end of the scratch.

The exposure time depends on the structures, the exposure parameters (dose and step size) and the beam current measured at the beginning. The software then calculates the dwell time on each point. A step size of 15.3 nm was used throughout this work. The dose varied from 125 $\mu C/cm^2$ for smaller structures and 300 $\mu C/cm^2$ for larger areas at the beginning to 750 $\mu C/cm^2$ for the most recent samples. Each time the EBL pattern has changed a dose test with the new layout was performed to choose the best dose. The best dose is the smallest dose that reliably produces the structures. The test consists of a series of exposures with different doses, followed by subsequent development and assessment of the exposed areas in the SEM. Figure 4.5 shows an example of a dose test with under and over dosed areas.

After the exposure has finished the sample is removed, put into the MIBK/IPA developer for 30 s, rinsed in IPA and dried in a clean nitrogen gas flow. The HOPG samples

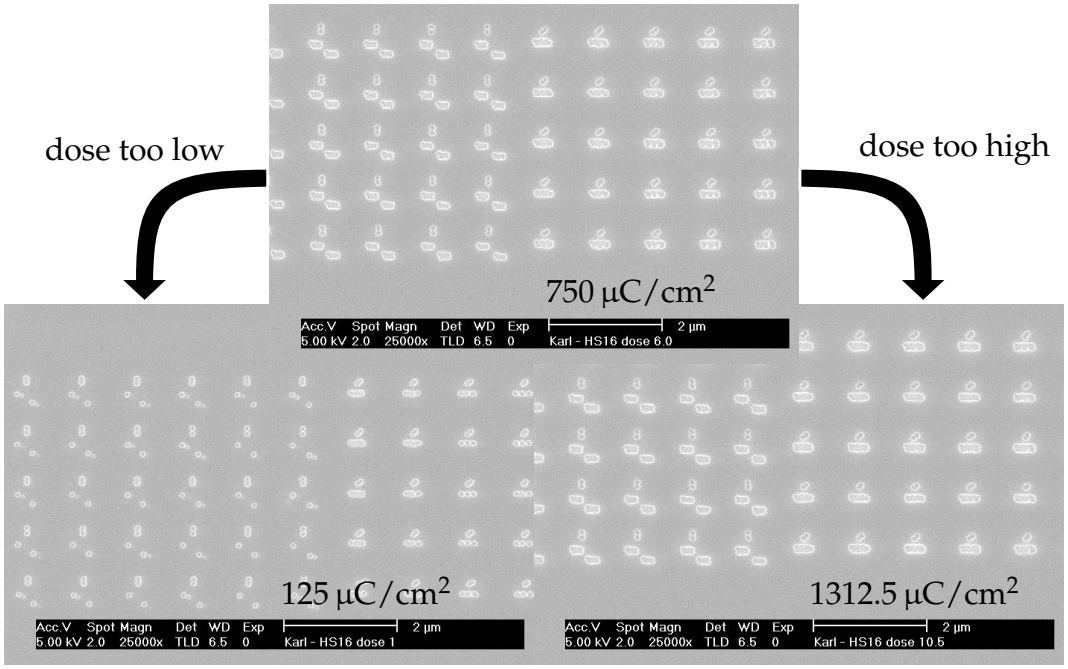


**Figure 4.5:** SEM dosetest with sample HS16. The structures are part of group ③ and ④ in Figure 4.12. The lower SEM images show examples of too low a dose (125 $\mu C/cm^2$) and too high a dose (1312.5 $\mu C/cm^2$).

are then fixed on standard stainless steel sample plates using two tantalum strips that are spot-welded on the sample plate.

Silver deposition was performed in the SPELS system using the evaporator described in Section 4.1. An external thermal evaporator from Edwards was used for gold deposition. Both evaporators use crucibles to heat the metal by direct current heating. The directional flow of this kind of evaporators is necessary to prevent deposition onto the hole walls which would hinder lift-off. Therefore, sputter coating was not used for EBL.

After metal deposition the samples are immersed in Acetone and held up side down as shown in Figure 4.6. The beaker is then covered and the sample is kept overnight in Acetone. In some cases the metal film did not come off and the samples were treated in an ultrasonic bath. The ultrasonic bath seems to have no effect on the silver or gold structures on HOPG. The sample holder for lift-off was made by the workshop. It was

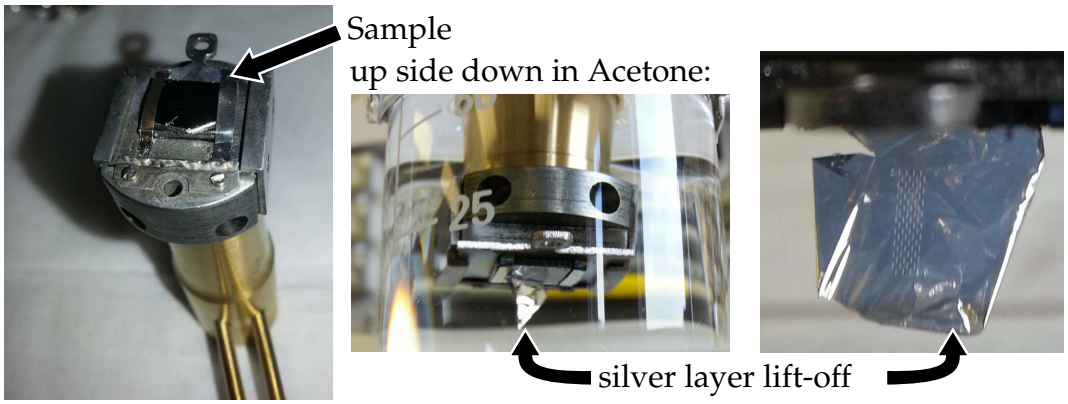


**Figure 4.6:** Lift-off of a silver film deposited on a poly(methyl methacrylate) (PMMA) resist patterned by EBL. The individual writefields of 200 µm height are visible as holes in the film in the right image. This sample consists of 72 writefields in 18 rows with 4 writefields in each row and with one "marker" structure on the start and the end of the patterned area.

necessary to support the sample up side down because the metal film can float back to the surface after the resist was dissolved as shown in Figure 4.7.

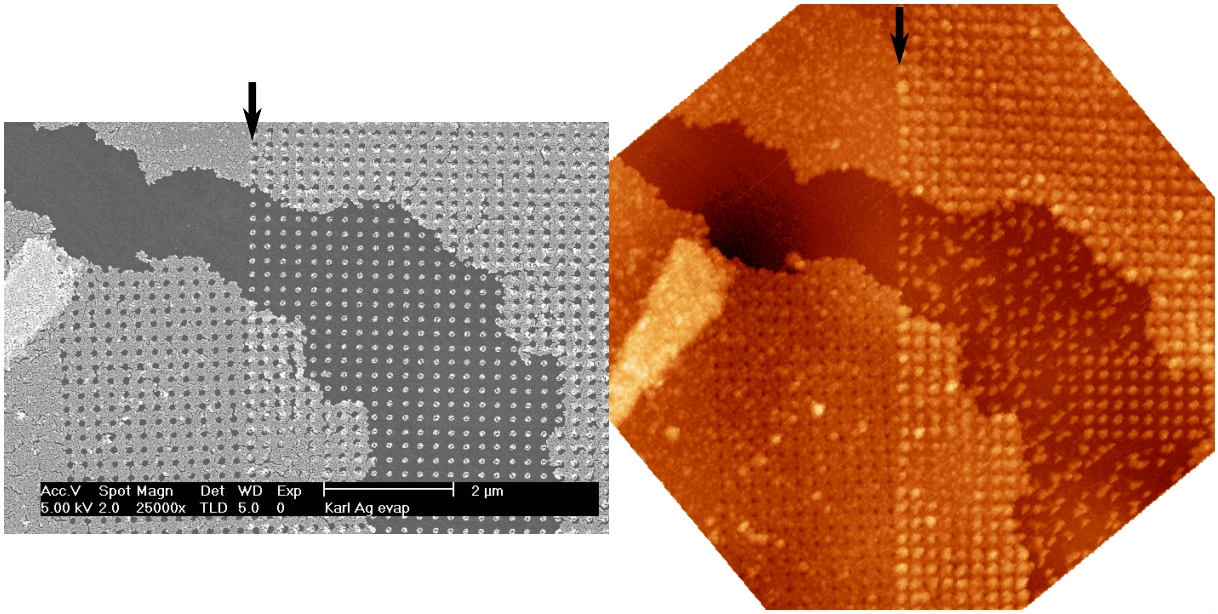


**Figure 4.7:** SEM (left) and AFM (right, tapping mode) images of the same area on sample HS1. The barrier of the patterned area is visible in the middle of the images and marked by the arrows. The left Ag layer has broken off and lies displaced on the sample by more than 2 µm. The right Ag layer is also displaced but only by 100 nm. PMMA was used as resist for HS1.

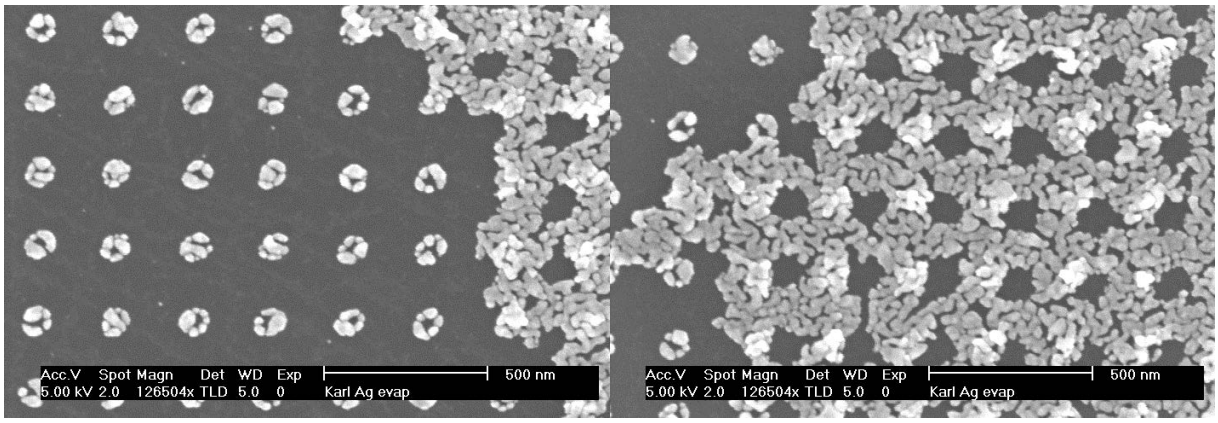


**Figure 4.8:** SEM images of silver structures on sample HS1 near the border of the displaced lift-off layer. The silver structures have a diameter of $100 \pm 10$ nm with a hight of 30 nm but consist of individual or attached islands.

To find the structures on the sample more easily in the microscope additional scratches which point to the edges of the patterned area are made. The scratches are not placed above the patterned area to avoid blocking the electrons on their way to the detector.

Samples prepared by EBL are given names for identification starting with "HS" and an ascending number. The first results using EBL (sample HS1) are shown in Figure 4.7 and 4.8. PMMA instead of SML was used for this sample. The EBL pattern consisted of $(50 \times 50)$ nm squares in a single writefield but was overexposed and instead resulted in circles with a diameter of 122 nm. Silver was evaporated on the sample at a rate of 2 ML/min for 25 min with the new evaporator using 7 A direct current to heat the crucible. A film thickness of 4.4 kÅ was measured at the quartz crystal monitor of the evaporator (as described in Section 4.1). The sample was not annealed prior to or during the metal deposition. The pressure in the preparation chamber was $2.2 \cdot 10^{-9}$ mbar. Apart from the overexposure and the failed lift-off the silver islands show an interesting structure. They seem to consist of several smaller silver islands that may be separated. If they are separated this would lead to several plasmonic "hot spots" within each structure that would increase plasmon resonance [105].

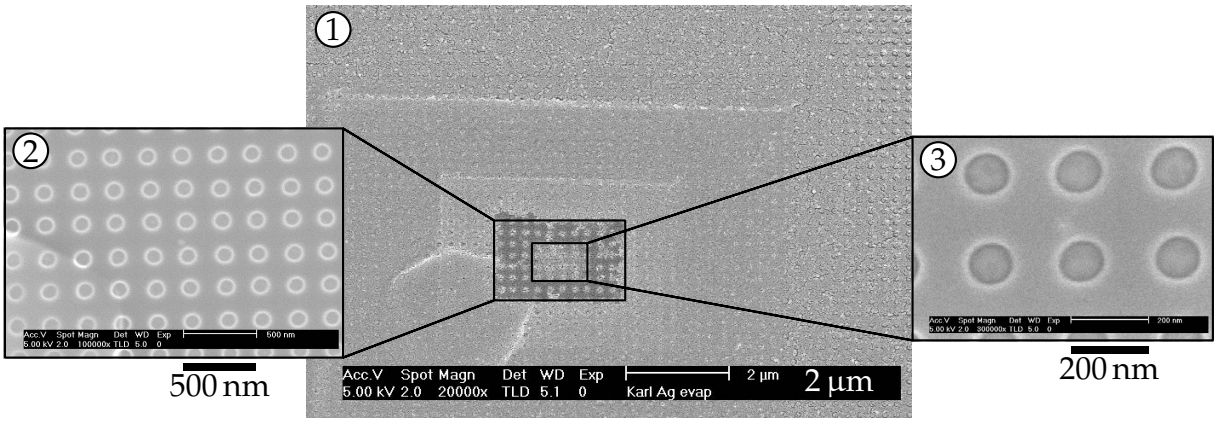


**Figure 4.9:** Image ① shows an area of the sample were the Ag layer was not removed during lift-off. Image ② and ③ have been taken on the marked area after developing and before Ag evaporation.

The part of sample HS1 that was imaged before the attempted lift-off is shown in Figure 4.9. The SEM images taken after the sample was in the developer are shown in ② and ③. After the sample was in Acetone image ① was taken. There is a perfect match between the images as indicated and the surrounding area was prevented from lift-off as no displacement of the silver layer is present.

### 4.2.2 Reduction of structure size

After the change to the resist SML100 and with an adjusted dose of 125 $\mu C/cm^2$ a structure size of 50 nm has been obtained as shown in Figure 4.10 for sample HS5. The islands are not clustered as were the structures shown in Figure 4.8. The amount of silver evaporated on this sample corresponds to a film thickness of 4.2 kÅ measured with the quartz crystal of the evaporator.

The field of silver structures is not visible when the sample is loaded into SPELS as with the MCA the only way to see the sample is with an optical camera from the viewport through which the picture in Figure 2.2 was made. The tip is positioned within the area marked by scratches which requires a large exposed area. To pattern a macroscopic

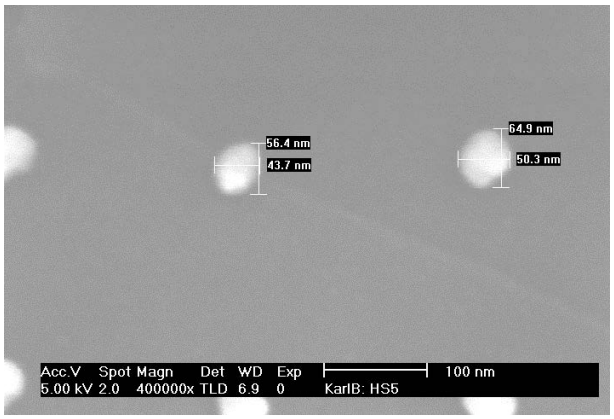


**Figure 4.10:** This SEM image shows Ag islands on HOPG with a diameter of about 50 nm.

area with EBL several writefields are written next to each other with a gap between the writefields to avoid overlapping structures due to the stitching error mentioned above. The height of the covered area is at least 3 mm or 15 writefields. The width depends on the time available but consists of at least 4 writefields. The pattern determines the time needed to write one writefield. By avoiding large structures the time needed for one writefield can be reduced. The total time required to expose one sample can take up to 10 hours.

### 4.2.3 EBL Pattern Layout Optimisation

To reduce patterning time the 200 µm×200 µm writefield has only been partially filled with a 200 µm×40 µm area. The writefields are placed in a chessboard pattern leaving 360 µm of free area between the pattern in the horizontal while covering the whole vertical axis as shown in Figure 4.11. The pattern consists of a 200 µm high structure on the left and a series of squares from 1 µm to 50 nm. When scanning this sample in SPELS the patterned area should be found ideally within 10 images which are separated by 40 µm. However, as the sample movement over such a distance is not exact a smaller step size is used in reality. Moreover, the scan range has to be at least 1 µm to make sure

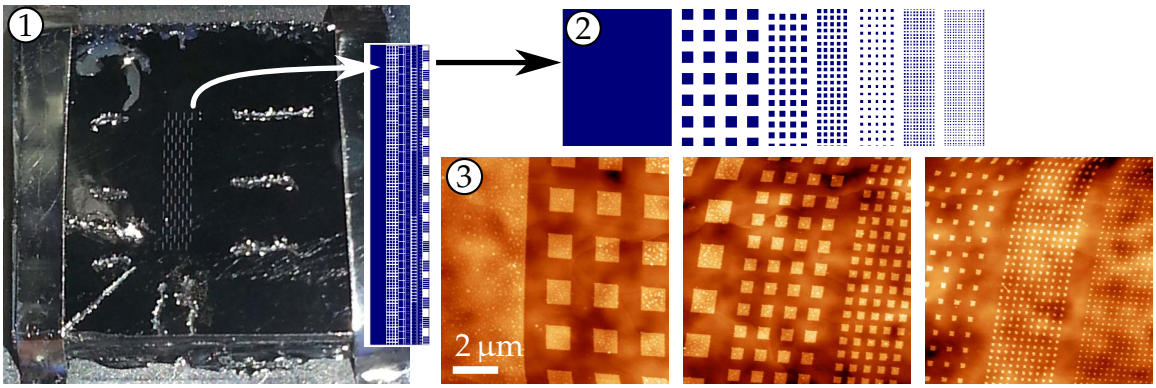


**Figure 4.11:** ① shows a photograph of a sample after lift-off. ② illustrates the pattern of one writefield. ③ shows 3 AFM images of the sample with a scan range of 10 µm each. The thickness of the Ag film is about 30 nm.

that an Ag area is within the image.

To avoid searching for the patterned area the 200 µm high structure has been omitted and the full writefield used for the pattern. This EBL layout is segmented in 1 µm squares which consist of a marker structure indicating the type of structure and the structure itself. Most structures have a width of 200 nm and a height of 100 nm. By limiting the structure size the time needed to write one writefield has been reduced to 13 min. The structures are squares, rectangles and triangles with varying distance and orientation to each other. A subset of the range of structures is shown in Figure 4.12.

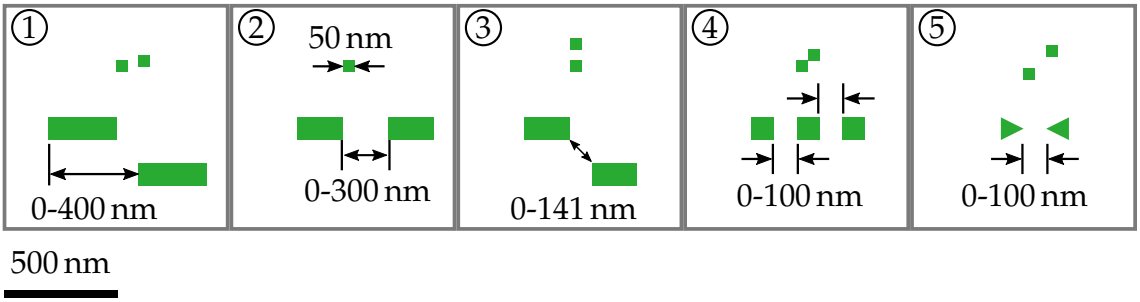


**Figure 4.12:** These structures (green areas) present a part of the EBL layout groups which were used to fill the writefield. The grey boxes mark 1 µm segments.

The distance between two structures in one segment is varied in 5 nm or 10 nm steps from zero to 100 nm and more depending on the structure. The step size is smaller than

the expected minimal hole size achievable by this instrument to ensure that a connected structure as well as a structure with a small gap exist. It also allows to measure the plasmon coupling dependence of the gap width. Segments within one column of the pattern are the same to ensure that every structure can be found by SPELS.

### 4.2.4 Silver structures on HOPG by EBL

Figure 4.13 shows two SEM images of the same sample. The sample was prepared

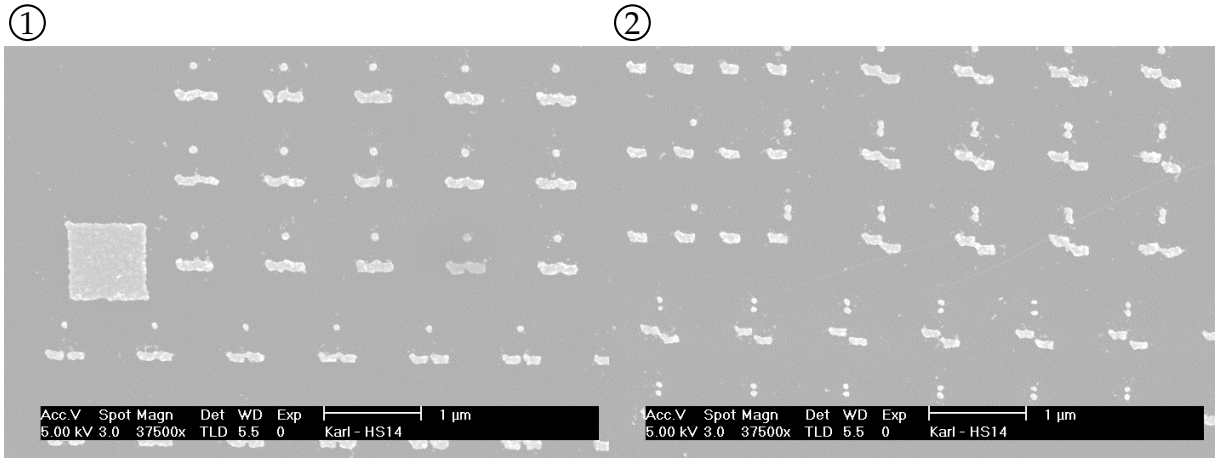


**Figure 4.13:** These SEM images show Ag nanostructures on HOPG prepared by EBL. The Ag film thickness was 35 nm. The 1 µm square in image ① marks the lower left corner of a writefield. Image ② shows the end of the structure group (group ② in Figure 4.12) which begins in Image ①.

using the EBL pattern as described in the previous section. The Ag film thickness in HOPG is 35 nm. The square with a side length of 1 µm marks the lower left corner of a 200 µm×200 µm writefield. The structures below this square are from a different writefield which is shifted to the left by a stitching error of 2.4 µm. The structures in Image ① show the beginning of group ② in Figure 4.12, starting at a gap of 0 nm. The structure itself consists of two rectangles, which are 200 nm wide and 100 nm high. The step size for the gap between two structures for this group is 5 nm. Image ② shows the end of this structure group with a gap of 300 nm and the beginning of the next group

(group ③ in Figure 4.12). The size of the structures is near the resolution limit of the instrument with this resist, which is the reason why the edges of the rectangles appear rounded.

### 4.2.5 Gold structures on HOPG by EBL

Figure 4.14 shows Au structures on HOPG using the pattern described in Figure 4.12. The change in distance between the structures is visible along the direction of the

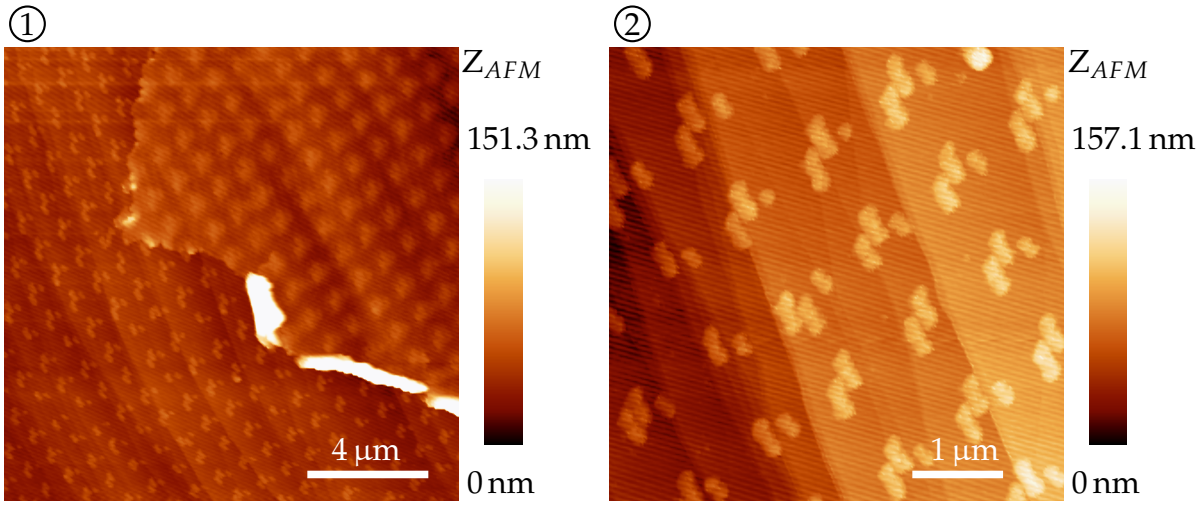


**Figure 4.14:** These tapping mode AFM images show Au nanostructures on HOPG prepared by EBL. The structure height is 35 nm. The structures are part of group ① in Figure 4.12.

diagonal from top left to bottom right. In image ① a part of the sample is covered with a Au film after an incomplete lift-off. Image ② shows the nanostructures in detail. The imaged structure is part of the pattern group ① in Figure 4.12. The lateral structure size appears bigger due to the width of the AFM tip similar to the effect described in Figure 1.3. The height of the Au film is 35 nm.

## 4.3 Summary

In summary, Ag and Au nanostructures have been prepared by EBL covering an area up to 3.4 mm high on HOPG. The preparation parameters and pattern layout have been optimised to achieve an accurate result and to maximise the covered area per hour. The pattern layout consists of a variety of geometries for different degrees of plasmon coupling. Groups of similar geometries can be identified by the relative position of one to three 50 nm squares next to the structures. SPELS measurements on these samples are discussed in Chapter 5.

# Chapter 5

# SPELS Performance and Images of Nanostructured Surfaces

## 5.0 Perspective

This chapter will discuss the performance and present the results of measurements using SPELS with the MCA and the RFA. The next section describes the behaviour of the instrument when key measurement parameters, like FE voltage and current, are changed. Section 5.2 describes SIMION simulations of the tip-sample junction during a SPELS measurement and discusses the shift of the analysed area with respect to the tip-sample separation. In Section 5.3 the performance of the two detectors used in this project is discussed. The SPELS images described in Section 5.4 were obtained using the MCA at a low count rate (4-21 kcps). Section 5.5 shows electron reflectivity images obtained with the RFA at high count rates of up to 295 kcps. Preliminary results demonstrating enhanced inelastic scattering at high FE voltages are presented in Section 5.6. The detector is situated at the lower left corner in all FE and SPELS images presented in this thesis.

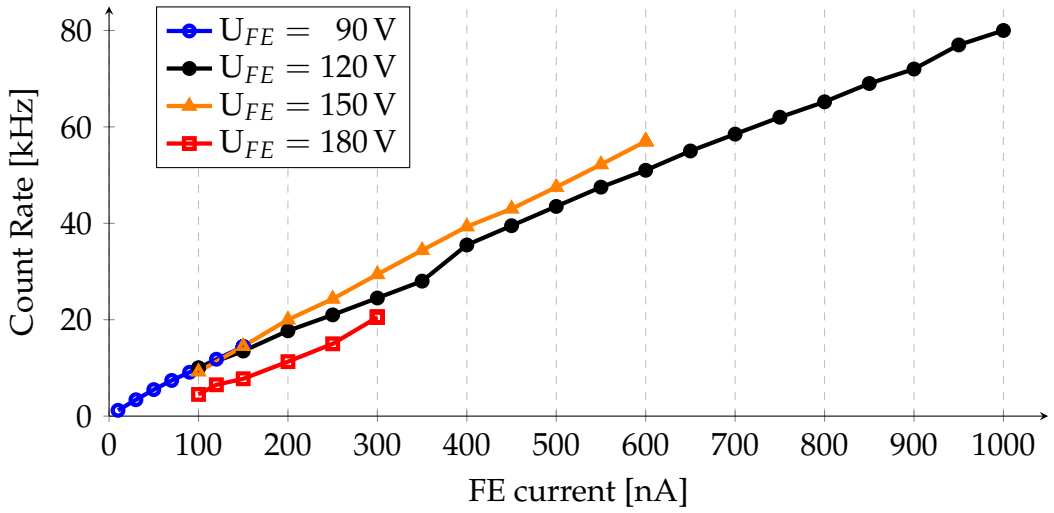


**Figure 5.1:** Backscattered electron count rate versus FE current for FE voltages from 90 V to 180 V. The count rate increases linear with the FE current. The measurement was performed on Au(111) with the MCA.

## 5.1 Field emission performance

This section describes the behaviour of the tip in the field emission regime. The following measurements show different influences on the count rate. They were made using a 267 µm long tungsten tip with an apex diameter of 31.8 nm on a single crystal Au(111) sample. The count rate has a linear dependency on the FE current over a wide range, as demonstrated in Figure 5.1. The influence of the FE voltage and therefore the tip-sample separation on the count rate can be seen in Figure 5.2. Note that the FE current ranges are different for different FE voltages in Figure 5.2. In this case the count rate at 100 nA was smaller at 180 V (4.5 kcps) than at 150 V (9.2 kcps), 120 V (10.0 kcps) or 90 V (10.0 kcps). The optimum FE voltage, regarding count rate only, is different for each tip shape and apex size. The FE voltage has a bigger influence on the tip-sample separation than the FE current.

Figure 5.3 demonstrates the importance of the annealing step described in Section 3.2.4. Note that here the logarithm of the count rate is displayed and that it increased by

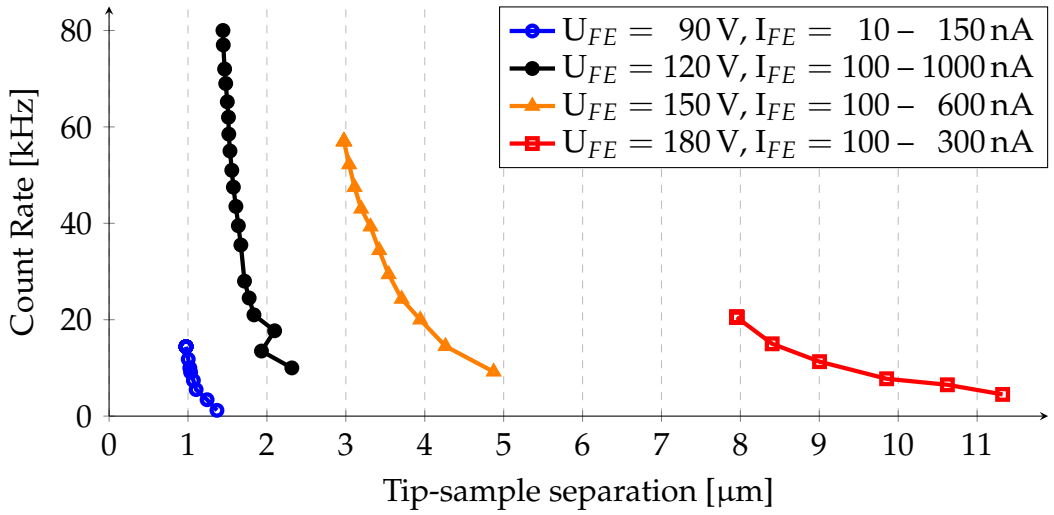


**Figure 5.2:** Influence of the tip-sample separation on the count rate. Note the different FE current ranges for different FE voltages. A higher FE voltage increases the tip-sample-separation while it is reduced by a higher FE current. The measurement was performed on Au(111) with the MCA.

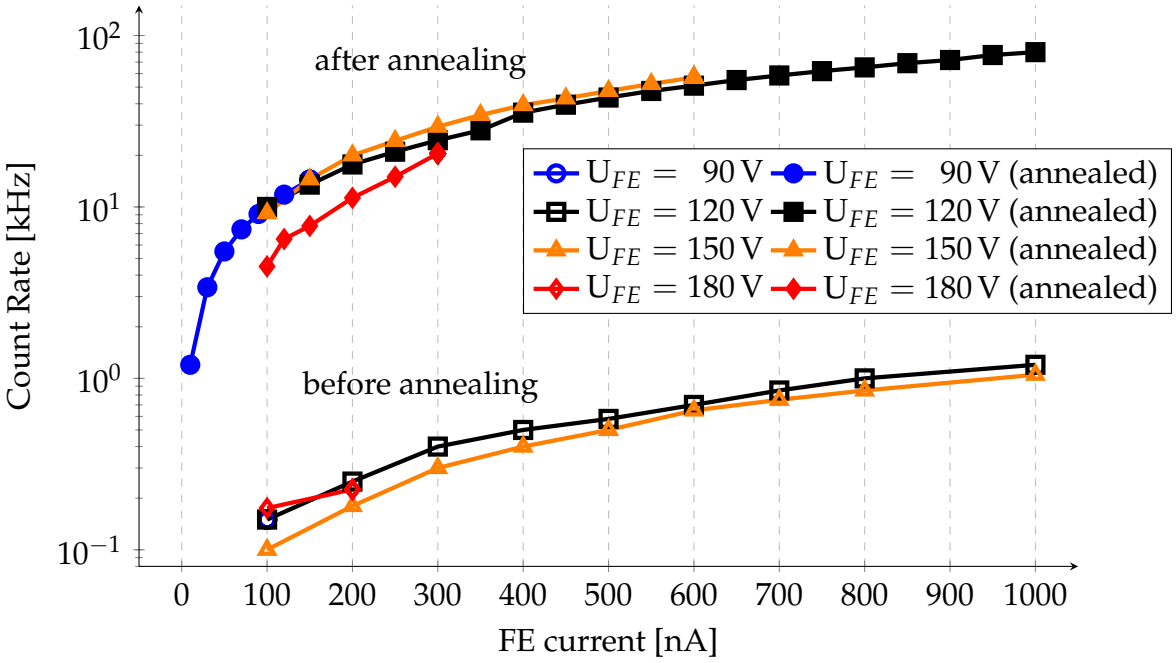


**Figure 5.3:** Backscattered electron count rate against FE current for different FE voltages for a tip before and after annealing. The count rate was increased substantially after the annealing process. The measurement was performed on Au(111) with the MCA.

nearly two orders of magnitude through the annealing step.

In conclusion, a high count rate can be obtained at a high FE current. The FE voltage increases tip-sample separation. Therefore, the voltage has to be decreased in some cases to gain sufficient lateral resolution.

## 5.2 SIMION simulations of SPELS

SIMION (see Section 3.1.4) has been used to shed light on electron paths within the tip-sample gap region. The following simulation of the electron trajectories near the tip-sample gap give a qualitative picture of the probed area during SPELS measurements. They simulate the path of backscattered electrons from the sample around the tip position but not the field emission of the tip. The results therefore show only an upper boundary for the probing area which would have to be multiplied with the field emitted electron distribution and scattering probabilities. The field emitted electron distribution resembles a Gaussian profile with a FWHM of the order of the tip-sample separation (see Figure 1.11 and [4]). To illustrate electron paths near the tip apex, a simulation of electrons with initial trajectories normal to the sample surface is shown in Figure 5.4. It can be seen that electrons originating near the tip position soon hit the sample again and that electrons originating further away from the tip have a higher elevation when leaving the simulation box. However, electrons further away are part of the tail section of the field emitted electron distribution.

To calculate which electrons are detected, a linear electron trajectory outside of the simulation box is assumed. This can be achieved by a co-axial tip which would neutralise the electric field in the outer regions [44]. However, even with a non-shielded tip, electrons that have a similar direction when they leave the simulation box will undergo a similar deflection on their way to the detector as the field in the outer regions is much smaller

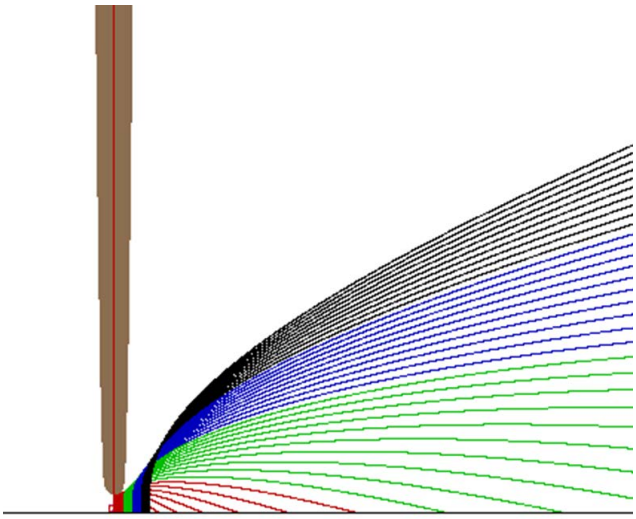

**Figure 5.4:** SIMION simulation for backscattered electrons along the normal to the surface for one direction. It can be seen that backscattered electrons near the tip position are bend back towards the sample (red lines). The tip-sample separation is 100 nm and the voltage applied to the tip is -90 V.

than the field near the tip (see Figure 3.18).

The simulation box is 700 nm high and includes 1 μm around the tip position. The tip voltage is -90 V while the sample is grounded. The detector entrance aperture is circular with a diameter of 5 mm and with a 7°angle towards the surface. The detector distance to the tip is 10 mm. The energy of the backscattered electrons is 85.5 eV assuming a 4.5 eV work function. The starting positions of the electrons are separated by 1 nm in both lateral dimensions. For each position a cone with a half angle of 0.05°around the surface normal is filled with electron trajectories. The output files have been analysed using a custom Java program.

Figure 5.5 illustrates a top-down view on the sample. The probing area (PA) is the area where the detected electrons originate. The change in colour illustrates the higher electron density nearer to the tip position due to the field emitted electron distribution. The position of the PA in respect to the tip depends on the applied voltage and the tip-sample separation. The minimum and maximum displacement of the PA as labelled

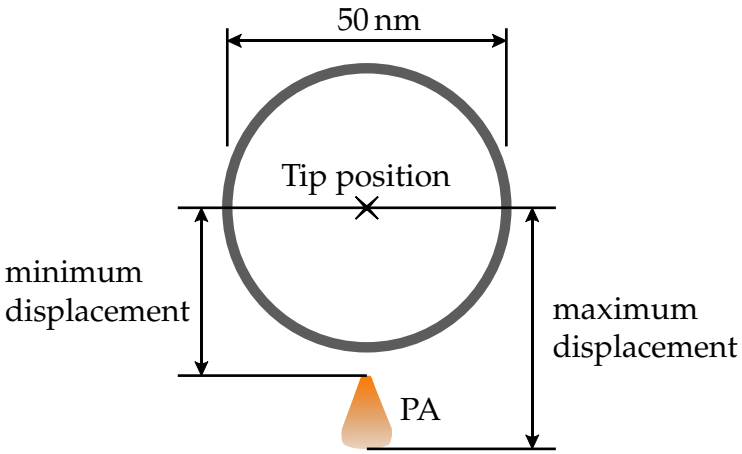


**Figure 5.5:** Backscattered electrons that reach the detector originate from the PA which is displaced from the tip position. The grey circle marks the size of the simulated tip with a tip apex diameter of 50 nm. The position of the PA displayed is calculated using a tip-sample separation of 50 nm and a detector at the bottom of the image. The colour variation illustrates the field emitted electron distribution which was not part of the simulation.

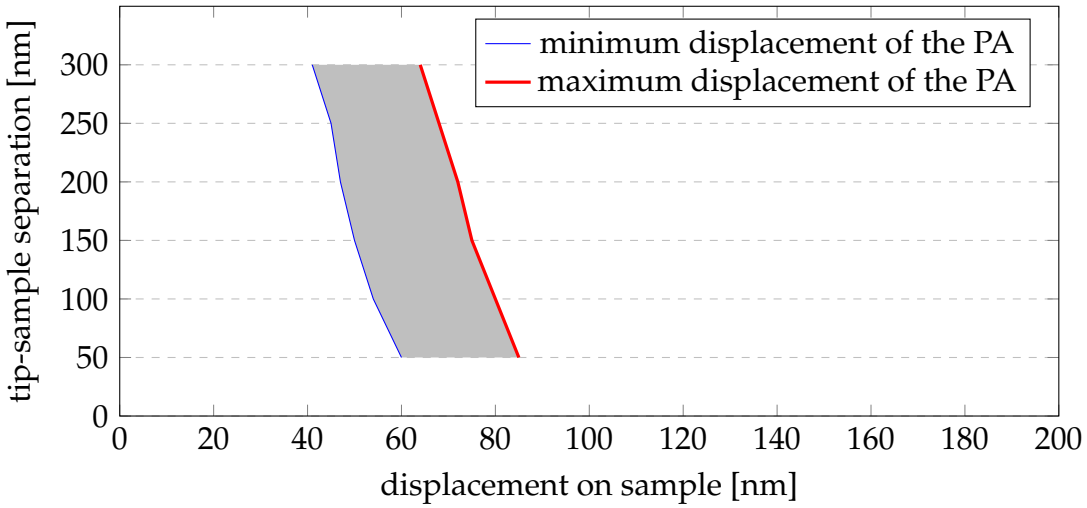


**Figure 5.6:** PA displacement as a function of tip-sample separation. A description of the minimum and maximum displacements is shown in Figure 5.5. This effect explains the loss in backscattered electron count rate at low tip-sample-separations as the electron beam intensity is lower at higher PA displacements.

in Figure 5.5 is plotted against the tip-sample separation in Figure 5.6.

The size and position of the PA does also depend on the size and distance to the detector

entrance which is kept constant in the present simulation. The position of the PA shifts away from the tip position with smaller tip-sample separation. This means that the backscattered electron image obtained with the electron detector is offset to the height image obtained with the current feedback loop. The direction of the offset is the direction of the detector.

Not only does this effect cause an offset in SPELS images but it will also influence the signal intensity as the electron flux reaching the sample is smaller further away from the tip position. Therefore fewer electrons will be reflected in a direction favourable for detection. The tip-sample separation can be varied for a given FE voltage by changing the set point current of the feedback loop. A higher FE current will lead to a higher signal as more electrons reach the surface but above a tip, voltage and detector dependent threshold the signal will decrease with increasing current as the displacement of the PA increases.

Although the results of the present simulation can only be applied in a qualitative manner, the effect described above is necessary to understand part of the results presented in Section 5.5.

## 5.3 Comparison of Detectors: Energy resolution and signal to noise

The performance of the two detectors used in this study is demonstrated in the following two subsections. For the MCA, spectra from an Au(111) single crystal, a thick (tens of μm) Ag layer on mica and HOPG are shown. For the RFA, spectra from HOPG are presented for different operating settings.

### 5.3.1 SPELS with the MCA

The MCA analyser was originally designed for HREELS experiments and is capable of achieving an energy resolution of a few meV [106]. The energy resolution of SPELS is limited by the energy distribution of field emitted electrons which can be determined by the FWHM of the elastic peak in electron energy loss spectra. It is typically 0.5 eV although the exact value is tip dependent. The main challenge of SPELS with the MCA is to achieve high enough signal levels as the distance between the sample and the entrance aperture of the analyser is large (about 340 mm) due to the size of the detector. Transfer lenses are used to increase the signal level as described in Section 2.3

Electron energy loss spectra obtained from a Au(111) single crystal and a thick Ag layer on mica are shown in Figure 5.7. Both metal surfaces have been cleaned *in situ* by Ar ion

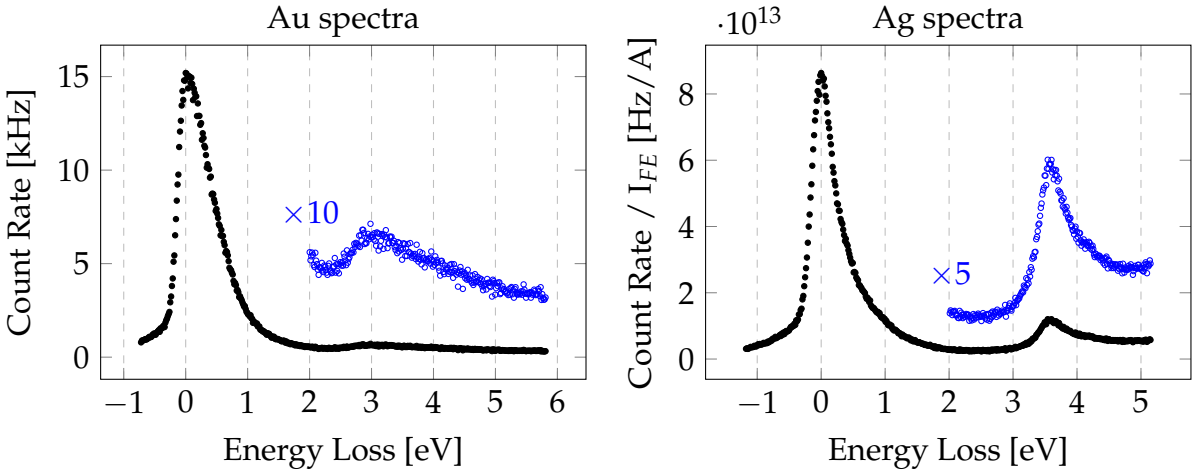


**Figure 5.7:** These energy loss spectra have been obtained from an Au(111) crystal and a thick Ag film on mica using the MCA. For the Au spectrum a tip voltage of 90 V at a FE current of 35 nA was used while the Ag spectrum was obtained at 150 V with 7.6 nA.

sputtering and annealing. The spectra show characteristic plasmon energies of 2.9 eV for Au and 3.6 eV for Ag. The spectra has been obtained using the full energy window of the MCA. The energy window can be shifted to measure surface excitations with

energies exceeding 6 eV. This is shown in Figure 5.8 for graphite. The measurement

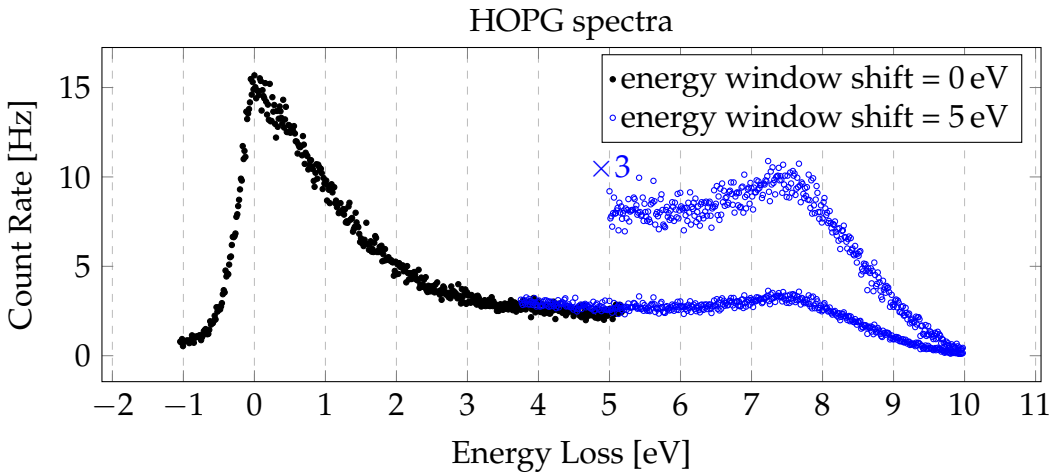


**Figure 5.8:** Spectra taken with the MCA on HOPG using a FE voltage of 35 V and a current set point of 150 nA. The energy window was shifted by 5 eV between the spectra using the lens voltage AN1. The HOPG plasmon is visible in the spectra with the shifted energy window.

parameters for the two spectra in Figure 5.8 have been the same apart from the AN1 voltage, which was used to shift the energy window by 5 eV.

The MCA voltages have to be chosen carefully as they can alter the measured spectra significantly. By changing the high voltages at the electron lenses while keeping all other measurement parameters (and therefore the electron source) constant, a variety of spectra can be produced. An example of this using a thick silver layer and a high tip-sample separation is shown in Figure 5.9. All spectra have been obtained at a tip voltage of 90 V and a FE current of 50 nA. The blue arrow on the left side of each spectra marks the maximum height of spectrum ② to illustrate the change in the elastic peak count rate. The integrated count rates of spectra ① to ④ were 7.4 kcps, 7.8 kcps, 4.0 kcps and 6.6 kcps as marked above the graphs. By choosing unsuitable lens voltages the Ag plasmon peak intensity (compare spectrum ① with ③) and position (compare spectrum ② with ③) can be varied. Moreover, additional peaks can occur (see spectrum ④). The count rate alone is therefore not sufficient to tune the MCA. The spectra from

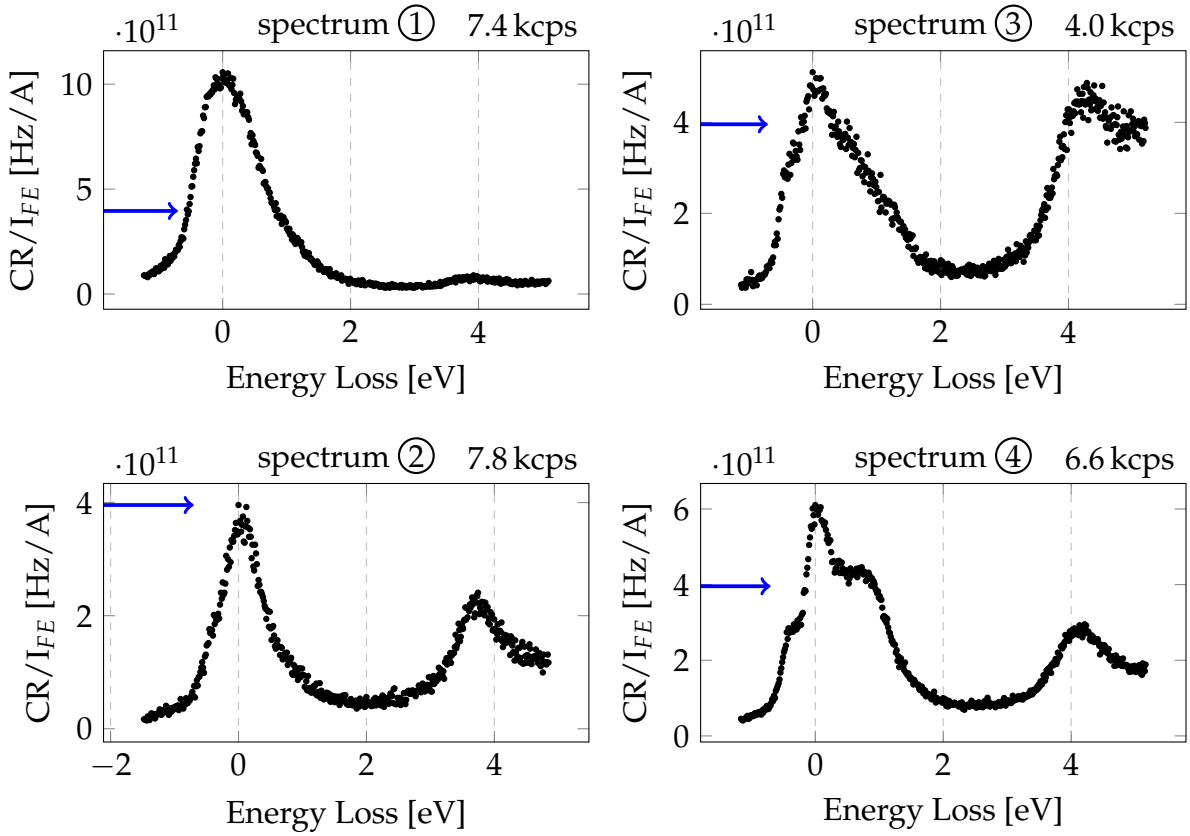


**Figure 5.9:** These spectra have been obtained consecutively using the MCA with the same tip on the same sample (a thick Ag layer on mica) position with the same imaging parameters. The tip voltage was 90 V, the FE current setpoint was 50 nA and the tip-sample separation was between 2174 nm and 2575 nm. The maximum count rate from spectrum ② is marked in all graphs by an arrow.

Figure 5.9 are part of a lens setting library, that was made for different tip voltages and current set points. To validate measured spectra an oscilloscope was used to image the 2-dimensional detector plane while tuning the analyser as shown in Figure 5.10. Each electron impact is converted to a 2-dimensional position by the counting electronics of the detector. Each dot on the screen of the oscilloscope represents one impact event. The energy dispersion of the electrons is imaged along the horizontal. The count rates are integrated along the vertical axis as they correspond to the same electron energy. The impact position on the detector can be moved and defocused along the vertical

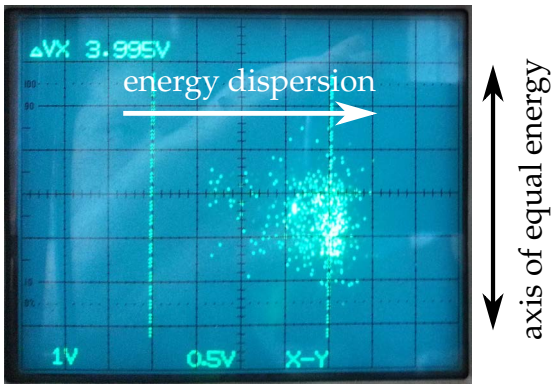


**Figure 5.10:** This picture of an oscilloscope screen shows the place of electron impact events on the resistive anode of the MCA detector plane.

axis. Moreover, the area can be aligned diagonally over the detector plane if the beam is defocussed. This means that the elastic peak can be cut off by the edge of the detector while the area representing the plasmon energy is still on the detector.

### 5.3.2 SPELS with the RFA

The RFA is, in contrast to the MCA, located near the sample at a distance of 20 mm to the entrance aperture and 38 mm to the CEM. This allows up to two orders of magnitude higher count rate. In pulse counting mode the signal level is limited by the Ratemeter to 1 Mcps. Higher count rates can be measured with the analogue mode but at the sacrifice of additional noise due to the variance in pulse height from different electron impact events.

The results acquired in Section 3.1.4 by SIMION simulations show an aperture with a size of up to 3 mm should be used for the RFA. The RFA has been tested with an aperture of 1 mm and 3 mm using the CEM in pulse counting mode. A spectrum taken with a 3 mm aperture on HOPG is shown in Figure 5.11. The graph also includes the raw count rate, on top of which the signal is measured, and the current during the sweep of the retarding voltage. As the signal intensity rises with lower retarding voltage

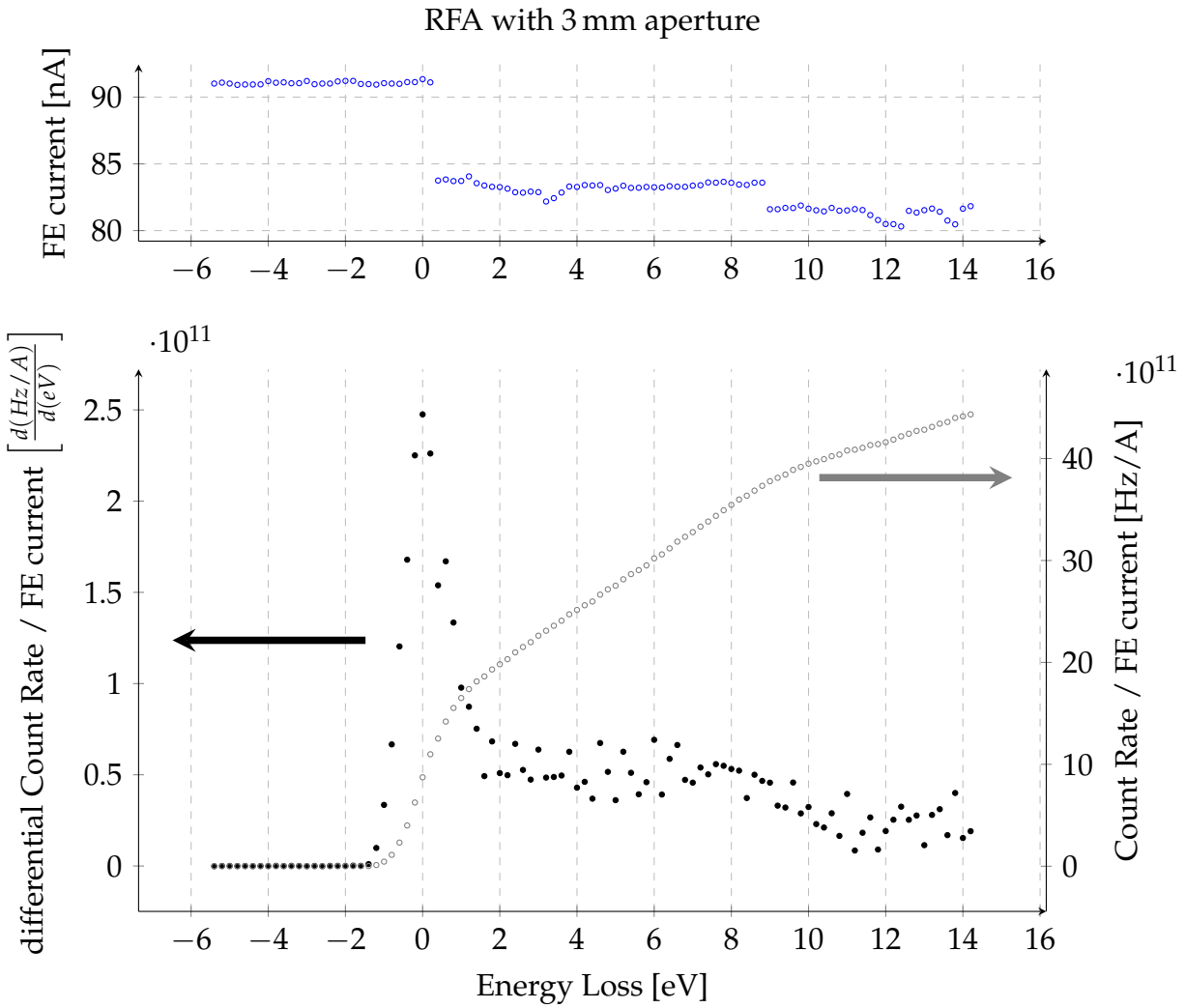


**Figure 5.11:** Total count rate and derived spectra of HOPG using the RFA with a 3 mm aperture are shown in the lower graph. The current during the sweep of the retarding voltage is shown in the upper graph. The current variations during the measurement are compensated by dividing the count rate by the FE current. The FE voltage was 100 V and the elastic peak maximum is at a retarding voltage of 94.4 V. The maximum count rate is 362.8 kcps. The FWHM of the elastic peak of 1.4 eV demonstrates the energy resolution of the RFA. However, the signal to noise ratio after the elastic peak is too small to measure the HOPG plasmon peak at 7 eV.

the signal-to-noise ratio drops significantly after the elastic peak. Any plasmon peak is measured on top of the signal from the elastic peak. This noise obscures the graphite plasmon peak which is expected at 7 eV in Figure 5.11. The current variations, caused

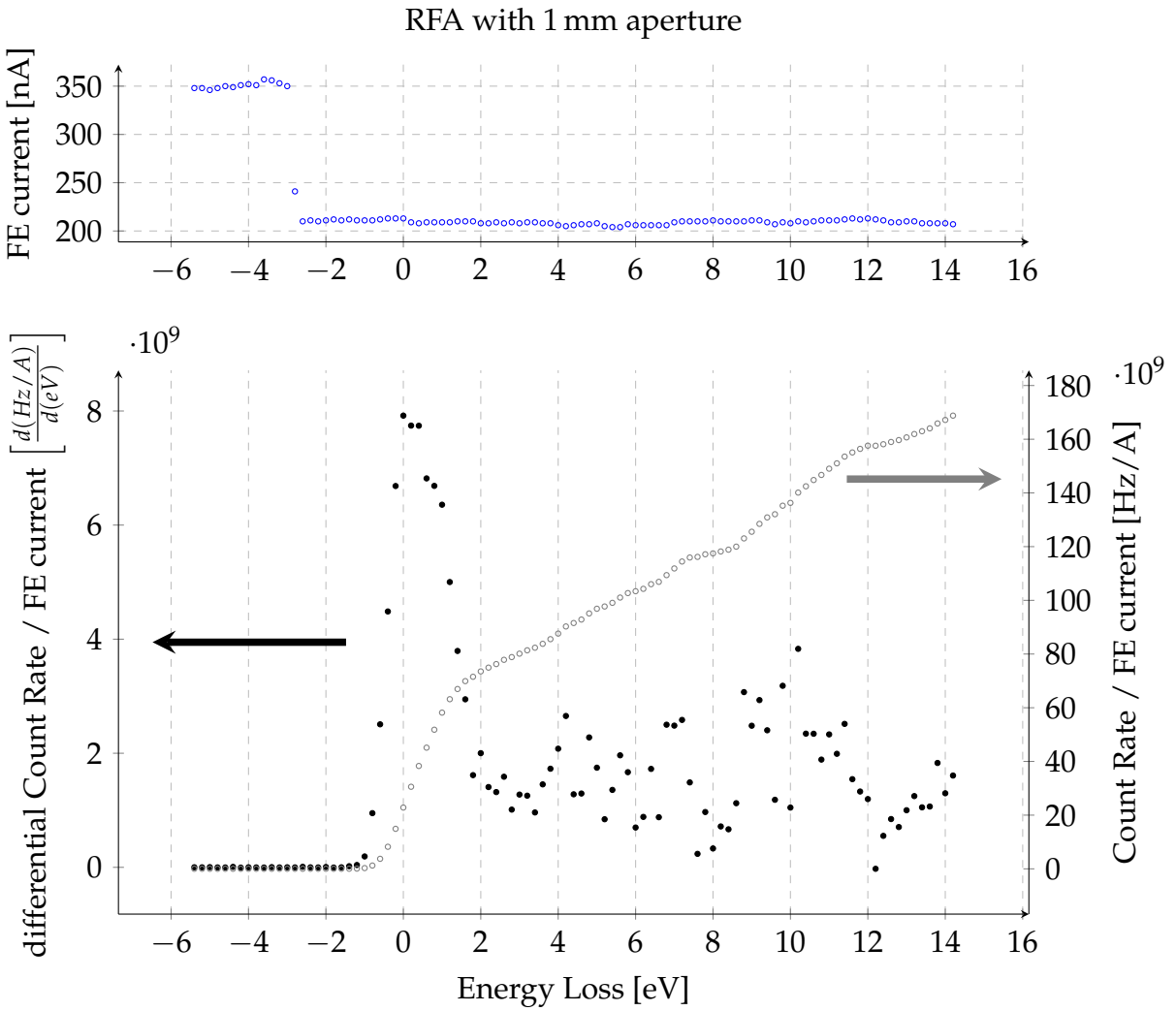


**Figure 5.12:** Total count rate and derived spectrum of HOPG using the RFA with a 1 mm aperture is shown in the lower graph. The current variations during the measurement are compensated by dividing the count rate by the FE current. The FE voltage was 85 V and the elastic peak maximum is at a retarding voltage of 79.4 V. The maximum count rate is 34.99 kcps.

by tip changes, are compensated by taking the ratio of count rate and FE current.

A spectrum taken with a 1 mm aperture is shown in Figure 5.12. The noise after the elastic peak is again too high to resolve the graphite plasmon peak.

While the plasmon peak is usually much smaller than the elastic peak, the secondary electron peak is of similar intensity even though the electric field suppresses low energy

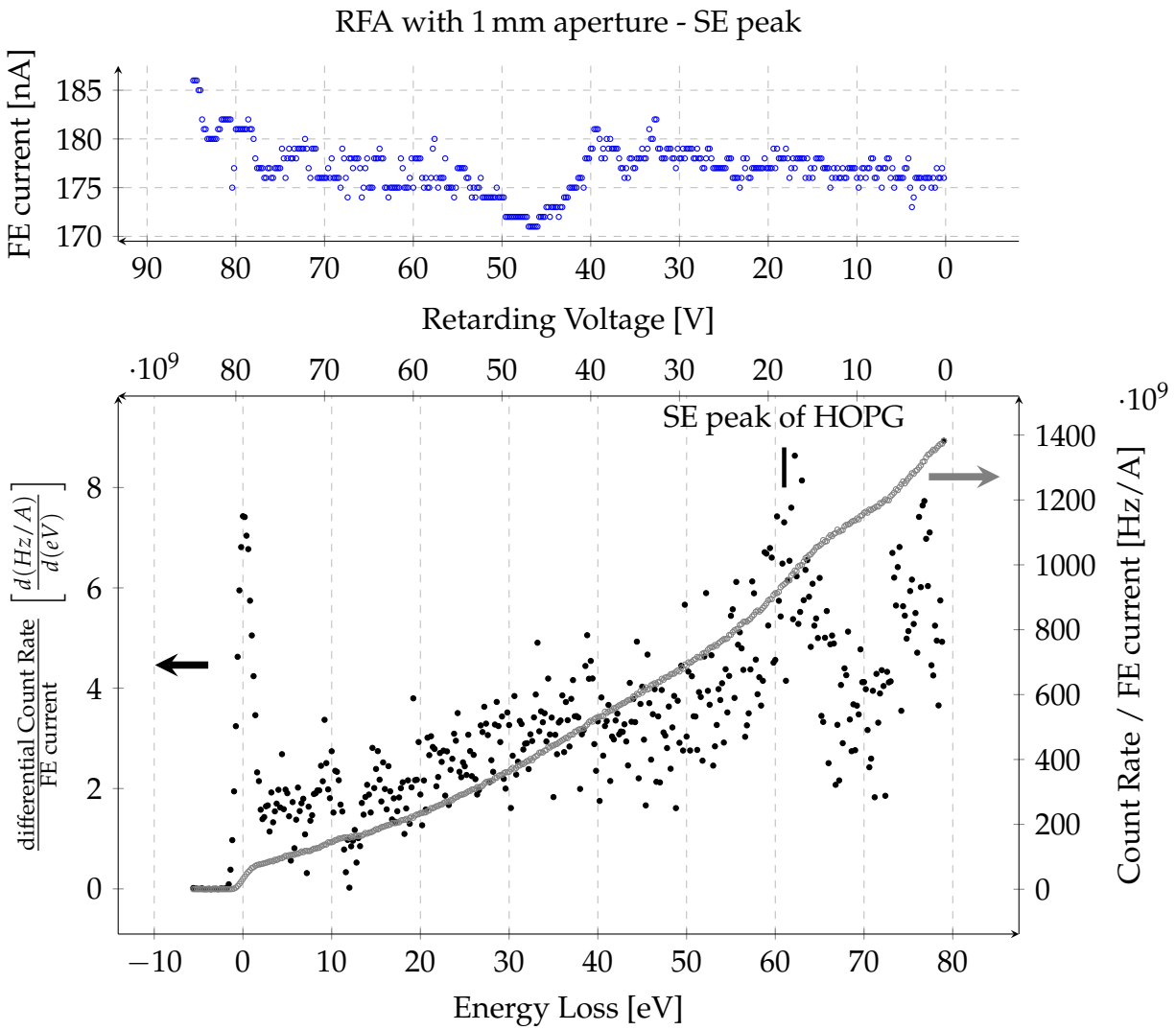


**Figure 5.13:** Total count rate and derived spectrum of HOPG using the RFA with a 1 mm aperture is shown in the lower graph. The current variations during the measurement are compensated by dividing the count rate by the FE current and the differentiated data is smoothed using a moving average filter with a span of 5. The FE voltage was 85 V and the elastic peak maximum is at a retarding voltage of 79.2 V. The maximum count rate is 243.8 kcps. The position of the secondary electron peak of HOPG at 19 eV is marked in the spectra.

electrons. Figure 5.13 shows a full HOPG spectrum down to a retarding voltage of zero. The spectrum has been processed by a moving average filter with a span of 5. The broad feature at a retarding voltage of 19 V (which is at 19 eV relative to the vacuum level of

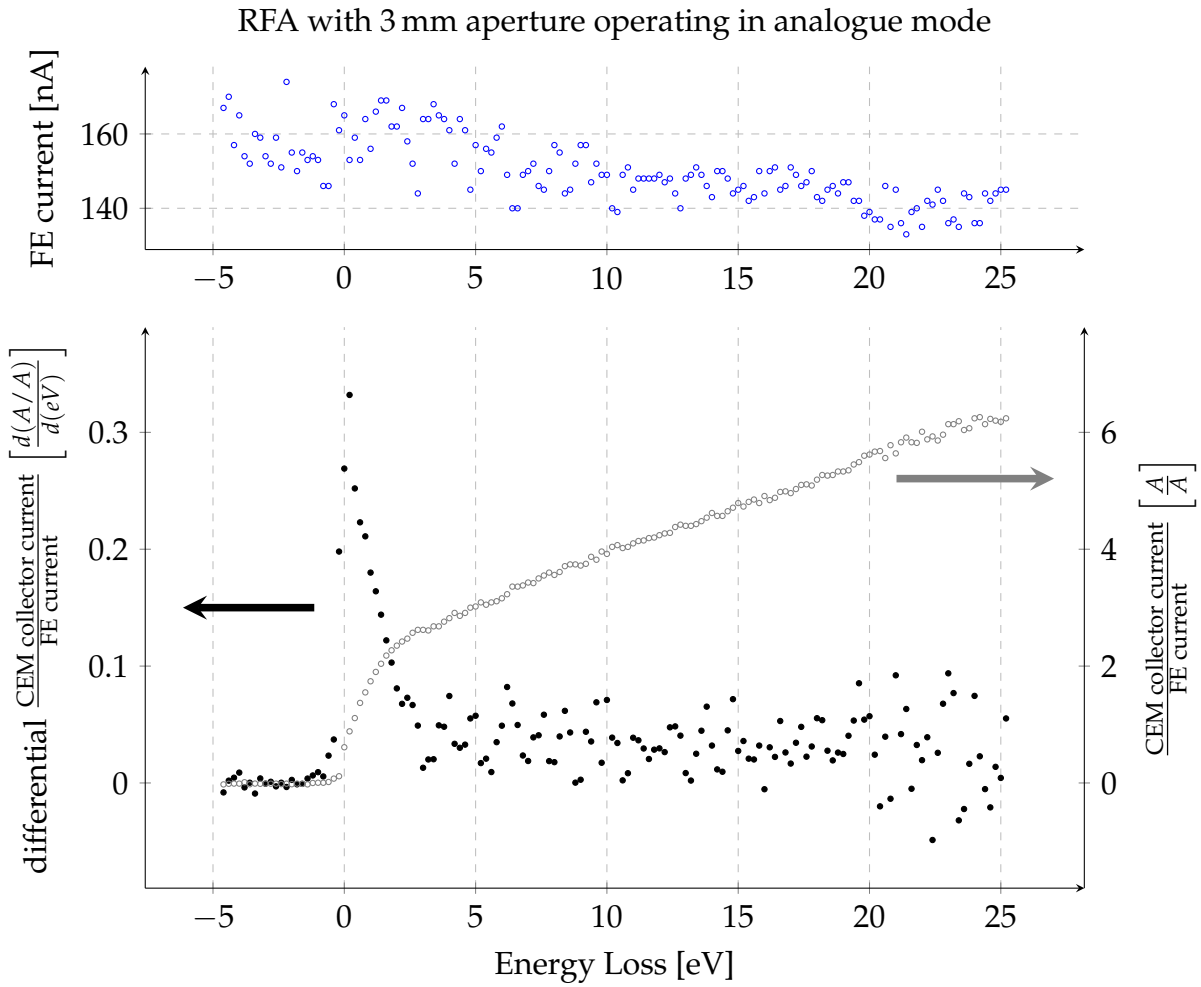


**Figure 5.14:** Total count rate and derived spectrum of HOPG using the RFA with a 3 mm aperture in analogue mode are shown in the lower graph. The current variations during the measurement are compensated by dividing the count rate by the FE current. The spectrum is smoothed using a moving average filter of span 3. The FE voltage was 130 V and the elastic peak maximum is at a retarding voltage of 125.2 V. The maximum current at the CEM collector is 902 nA.

the sample) corresponds to literature values of HOPG [107].

The spectra so far have been obtained using the CEM in pulse counting mode, which limits the count rate to 1 Mcps. Figure 5.14 shows a spectrum obtained in analogue mode using an aperture size of 3 mm. This spectrum has been obtained after the ratemeter saturated in pulse counting mode at 120 V with a FE current between 61.7 nA and

80.4 nA. The tip and sample position was kept constant between these measurements. The higher FE voltage and current of 130 V and 133 nA to 174 nA in analogue mode should lead to a total count rate exceeding 1 MHz, but the signal-to-noise ratio is still insufficient to identify plasmon peaks. The differential spectrum in Figure 5.14 has been smoothed using a moving average filter with a span of 3.

## 5.4 Energy loss images due to plasmon excitation

The first measurements with the MCA from heterogeneous samples have been obtained from annealed HOPG samples with thermally evaporated silver. This leads to a few hundred nm high silver islands randomly positioned on the graphite surface. Figure 5.15 shows a sample prepared by annealing for 15 min at 460 °C, sputtering for 30 s with 500 eV Argon ions and silver deposition for 10 min with the old evaporator using a current of 11.05 A. The sample was subsequently annealed for 15 min at 477 °C. It shows up to 500 nm high silver islands on HOPG in the left image in Figure 5.15. The right image shows the electron reflectivity image taken on the same sample position on the next day. A small drift to the top right is visible. This electron reflectivity image was taken directly before the SPELS image shown in Figure 5.16. Image ① in Figure 5.16 shows the height variations during the SPELS image without any image processing. Therefore, the upper left corner appears lower than in Figure 5.15 as the sample tilt is not compensated. The count rate of elastically backscattered electrons as shown in image ② is higher on graphite than on silver. Image ③ shows the count rate per FE current for energy losses between 3 eV and 4.5 eV which includes the silver surface plasmon energy. The count rate from the silver islands increased slightly but the overall reflectivity change overcompensates this. The signal at the Ag plasmon energy over regions of graphite can be caused by the tail of the elastic peak or a Ag layer on the tip.

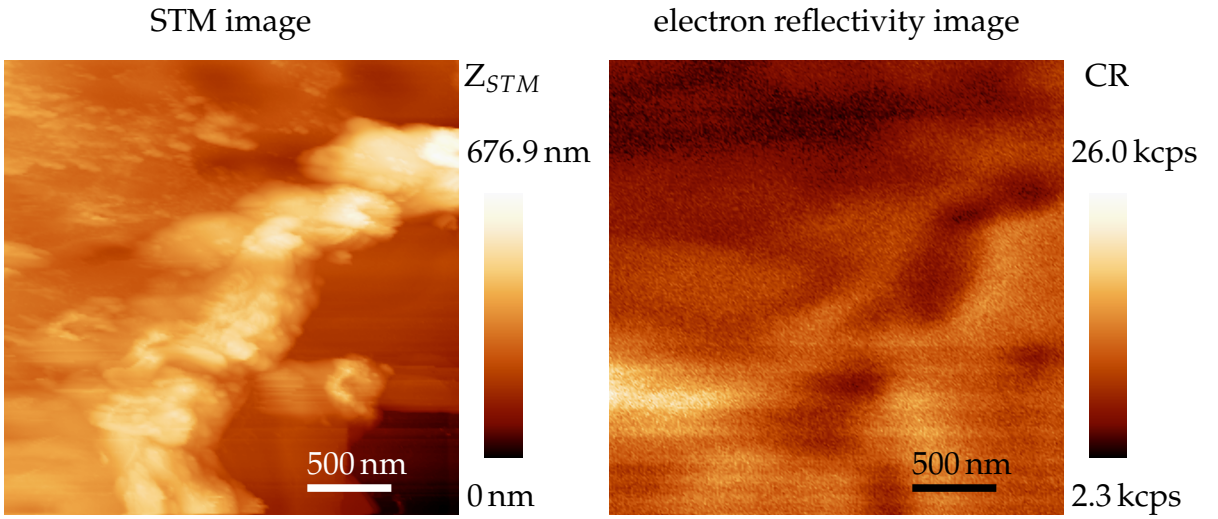


**Figure 5.15:** The left image shows an STM image of a 500 nm high Ag island on HOPG taken at a tunnelling voltage of 0.6 V and a current of 1 nA. Ag was evaporated on HOPG at a sample temperature of 477 °C. A plane fit using the flat area right of the silver island has been applied to compensate for the sample tilt. The right image shows the count rate during a constant current electron reflectivity image using a FE voltage of 60 V at a setpoint of 10 nA of the same area but on the next day. A drift to the right of the image is visible. The scan range is 2.7 µm.

Therefore the spectra from each point have to be normalised individually with respect to the elastic peak. This results in image ④ which maps the relative probability for an electron to lose energy to a silver surface plasmon on the sample. The plasmon intensity (between 3 eV to 4.5 eV) varies between 6.7 % and 14.7 % of the elastic peak maximum.

Figure 5.17 shows normalised and raw data spectra from high signal (Ⓐ) and low signal (Ⓑ) regions in the normalised image for energy losses of 3 eV to 4.5 eV as well as the integrated count rate over all spectra taken during the measurement. The zero energy loss position on the detector of the MCA is assigned at the beginning of a SPELS image and this energy axis is then used for all points of the image. If the tip changes during the image, the work function and therefore the energy of the elastic peak can shift. This is visible in the integrated count rate spectra.

The raw data spectra in Figure 5.17 have the same axis range. You can see that the

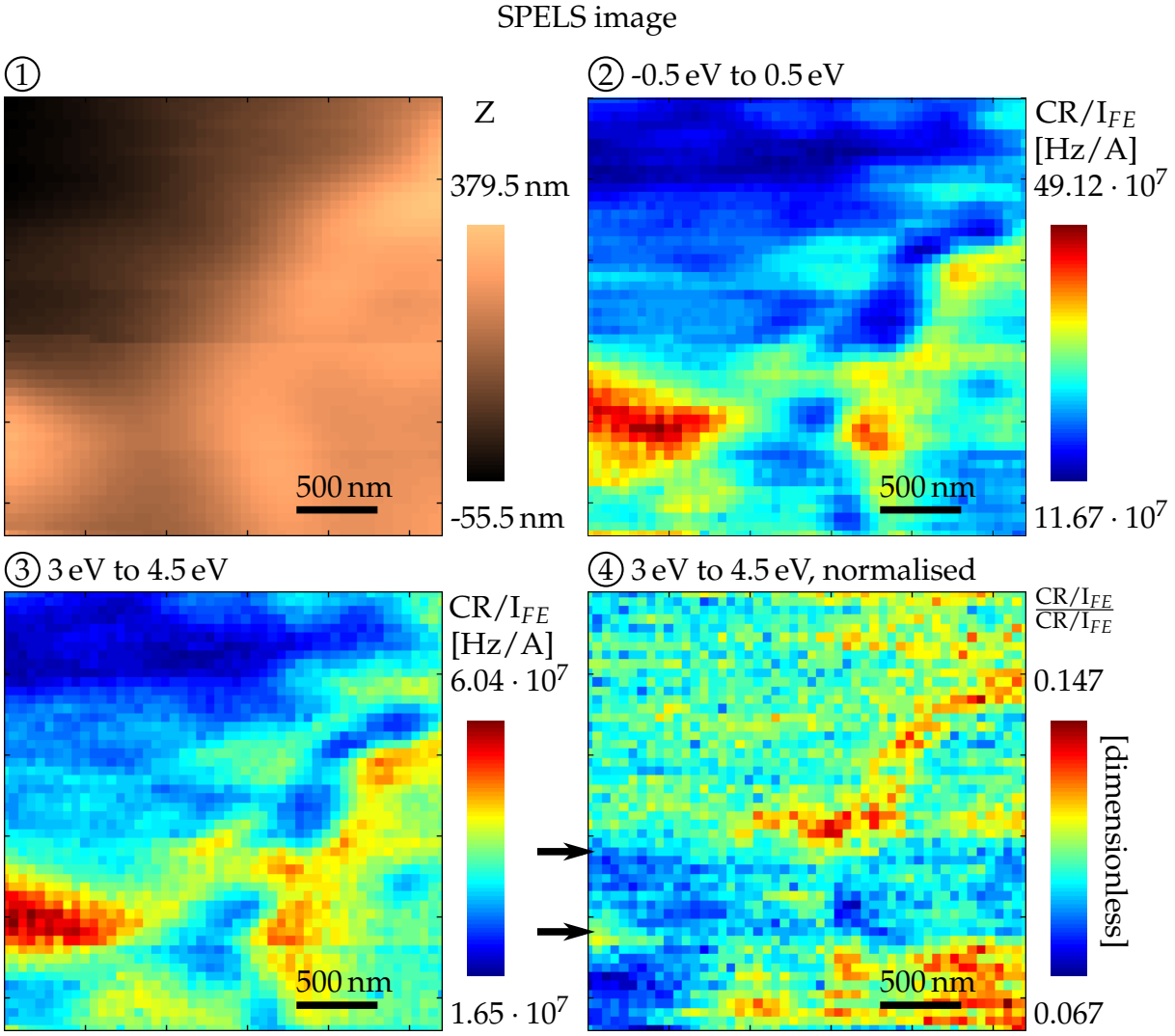


**Figure 5.16:** This SPELS image was taken on the same area as the right image in Figure 5.15. The FE voltage is 150 V, the current set point is 500 nA and the scan range is 2.7 µm. The dwell time per point is 3 s and the scan grid contains 50×50 points. Image ① shows the height variations during the scan at a constant FE current of 500 nA and image ② shows the count rate per current around the elastic peak obtained over each point. Image ③ and ④ show the count rate per current in the range from 3 eV to 4.5 eV. Image ④ is normalised against the maximum count rate per current in the elastic peak for each point (see Figure 5.17 for examples).

absolute change between a low signal and a high signal point for the whole spectra can be significant. Point Ⓐ has a total count rate of 7.04 kcps while point Ⓑ has 12.97 kcps. Both have roughly the same signal intensity around the plasmon energy.

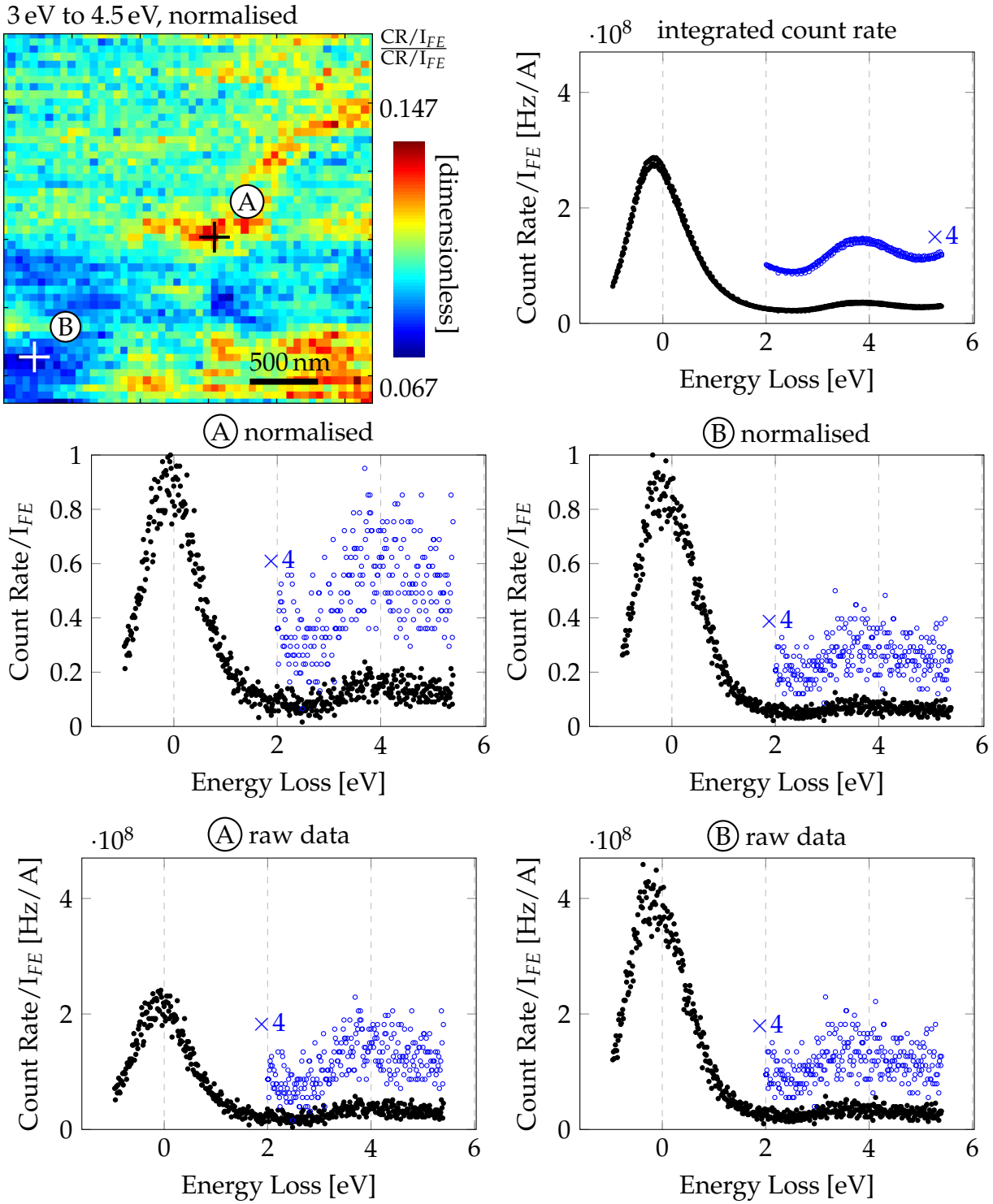


**Figure 5.17:** These energy loss spectra have been obtained during the SPELS image described in Figure 5.16. See text for details.

The normalised spectra show the different plasmon intensities in relation to the local electron reflectivity. High relative plasmon intensities occur at the position of the regions of low electron reflectivity or Ag islands. However, the contrast to the surrounding HOPG surface is not very defined along the island edges and not all of the silver structures appear bright in the normalised plasmon image. This is partly because of a tip change which occurred during the scan and partly because of the low signal to noise ratio of the individual spectra. The image consists of $50 \times 50$ points and needed over 2 hours to complete. The scan direction was bottom to top and forward. After about one fifth of the image (line 12 from the bottom of the image) the normalised plasmon intensity decreased from one line to the next and regained the former level after another 9 lines. This band is marked with arrows in image ④ in Figure 5.16. Please note that both points of the spectra in Figure 5.17 are outside of this band. This band is also visible in the Z image (image ①) as an about 30 nm higher region. This changes the electric field between tip and sample so that the relative plasmon intensity within the band is not comparable with the rest of the image. This is mainly a problem of signal to noise ratio as tip changes during hours of FE at 500 nA are inevitable.

Another difficulty in analysing this kind of measurement on thermally evaporated silver on a graphite surface is that the silver can go anywhere on the surface and will migrate to stable positions like graphite step edges. As SPELS is a technique utilizing low electron energies it is highly surface sensitive (see Figure 1.13) and might detect a signal from small silver islands that are not visible in the large area scan STM image shown in Figure 5.15 due to the limited resolution of the image. Therefore, small silver nanowires at HOPG step edges were made by using a small evaporation rate at elevated sample temperatures similar to the technique described in [102]. This was possible due to the new evaporator described in Section 4.1 which is facing the heatable sample stage in the preparation chamber. By concentrating on the small silver agglomeration at the

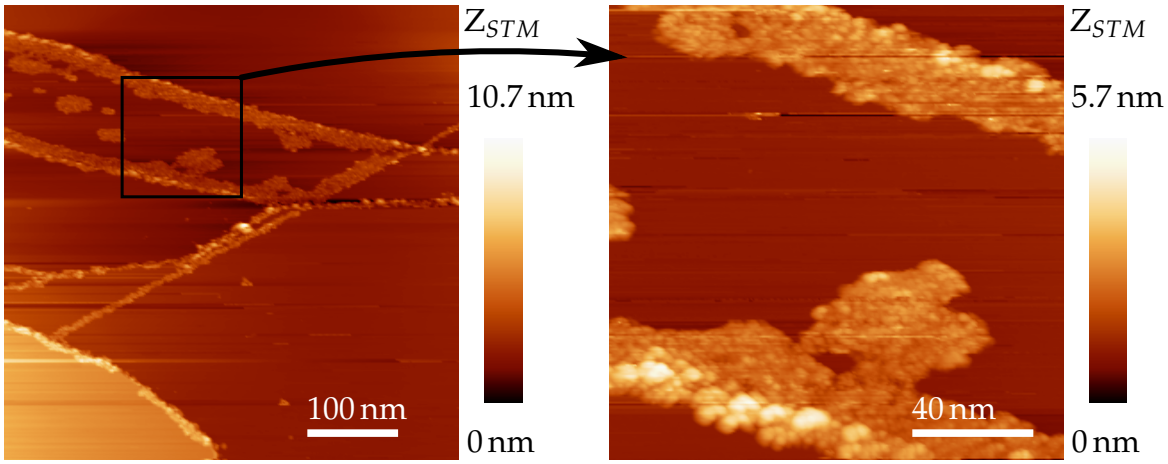


**Figure 5.18:** These STM images show Ag accumulated at HOPG step edges. The height of the silver structures is 1 nm to 3 nm. Both images were taken with a tunnelling voltage of -3 V and a current of 300 pA. SPELS images of these structures show no contrast in the plasmon peak but only in electron reflectivity.

step edges the HOPG terraces are free of silver. This is also a test of the lateral resolution limit of the instrument and its detection limit for smaller structures with decreasing plasmon intensity. Figure 5.18 shows such a sample which was prepared by evaporation of 1.65 Å of silver at a deposition rate of 0.33 Å/s and a sample temperature of 159 °C. The height of the silver structures at the step edges is 1 nm to 3 nm. Although they show a smaller electron reflectivity they showed no plasmon peak in SPELS images. The signal to noise level with the MCA has been too small to detect the small plasmon intensity of these structures.

To control silver structure sizes while keeping HOPG areas free of silver, EBL was used to prepare samples as described in Chapter 4. Figure 5.19 shows an FE height image and an electron reflectivity image of 200 nm silver squares on HOPG which are separated by 200 nm. The height of the silver field was measured by STM to be 40 nm. The lower reflectivity of Ag is visible in the electron reflectivity image and in a subsequent SPELS image but there is no contrast in the energy region of the silver plasmon. The count rate intensity drops by (-18.6±4.8) % at the position of the Ag islands. Samples with thicker

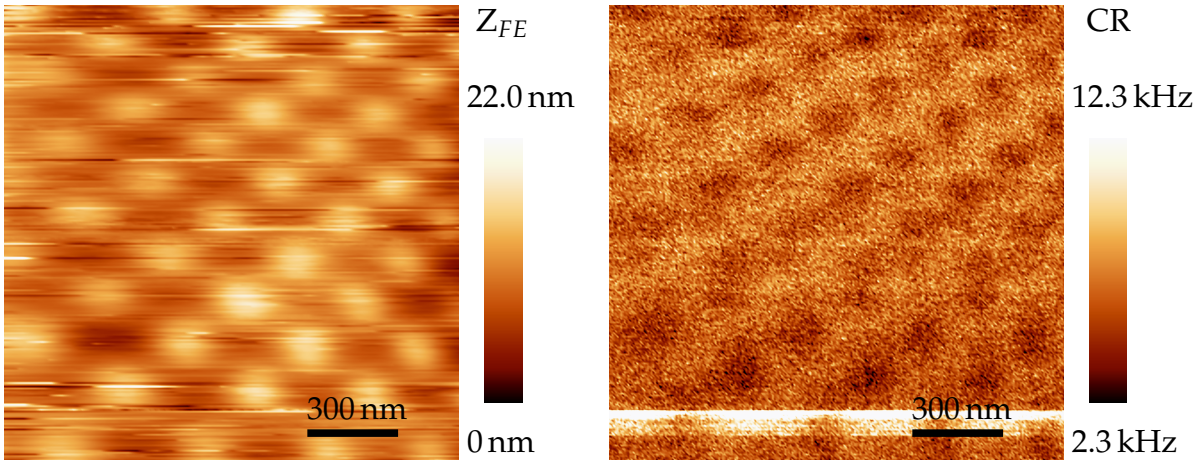


**Figure 5.19:** These electron reflectivity images show the height and count rate variations during the same measurement. The FE voltage and current were 60 V and 1 µA. The pattern of 200 nm big Ag squares is visible in the count rate image through their lower reflectivity. The thickness of the silver film is 40 nm.

Ag layers have only been measured using the RFA.

It is clear from the spectra shown in Section 5.3.2 that the signal-to-noise of the retarding field analyser after the elastic peak is not high enough to enable measurements of plasmon excitations with an intensity as low as in Figure 5.17. However, it allows to cut-off inelastically scattered and secondary electrons and thus permits measurements of elastically backscattered electrons.

## 5.5 Imaging via the electron reflectivity contrast

The reflectivity contrast in SPELS is caused by the surface morphology (e.g. electron blocking), an elemental contrast due to a change in the backscattered electron coefficient for different elements and due to changes of measurement parameters. Surface features with both a reduced electron reflectivity (negative contrast) and an increased reflectivity (positive contrast) to the substrate HOPG have been found and are presented in the following sections.

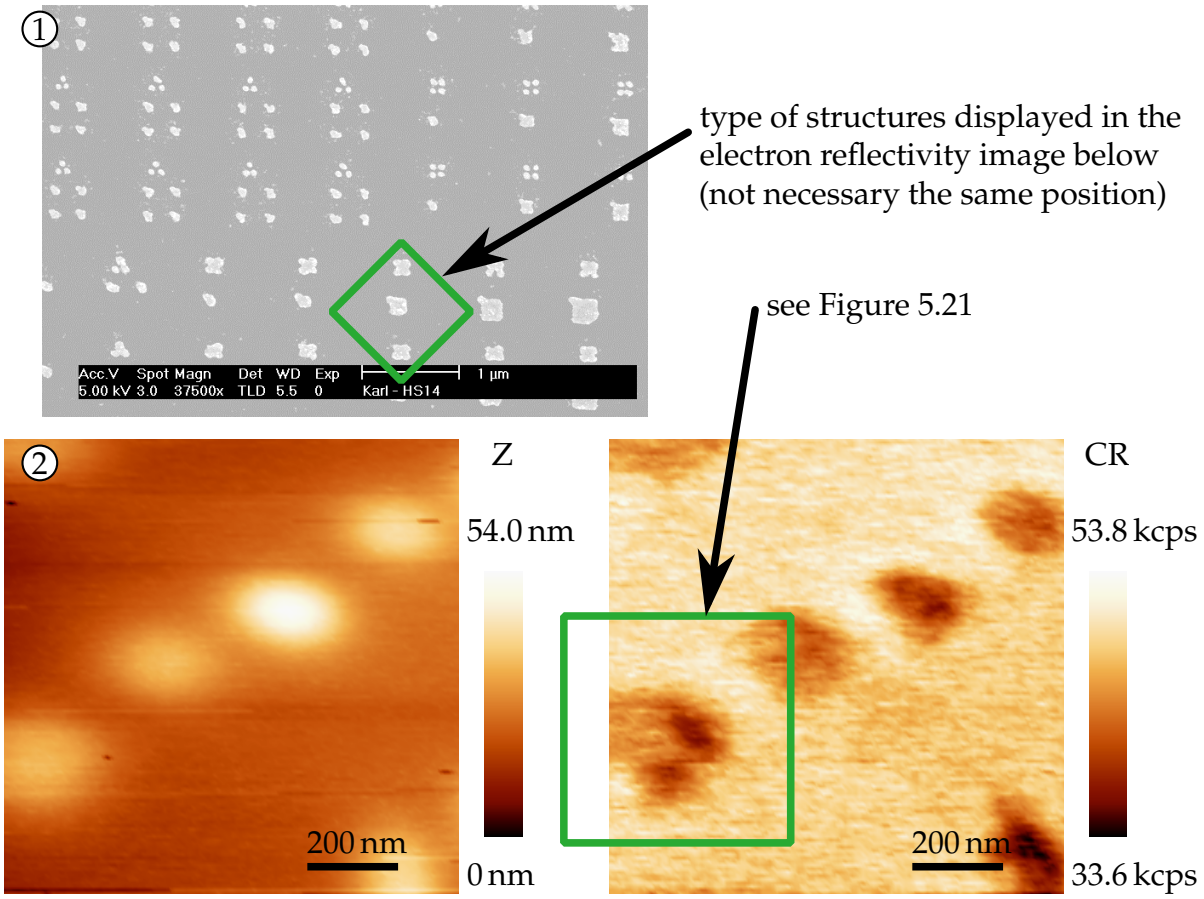


**Figure 5.20:** ① SEM image of the sample displaying the type of structure shown in ② and Figure 5.21. ② FE height and electron reflectivity images using a FE voltage of 60 V, a current of 10 nA and a retarding voltage of 20 V. The tip-sample separation was 100 nm. The position of the electron reflectivity image in Figure 5.21 is marked.

### 5.5.1 Negative reflectivity contrast

Figure 5.20 shows the field emission and backscattered electron image of silver nanostructures on HOPG (②). The type of structure that has been imaged in ② is marked in the SEM image ①, which was taken from the same sample. While the tilted square represents the scan range and orientation of the electron reflectivity image, the SEM image does not necessary show the position of the electron reflectivity image. The horizontal shift of the structure size in image ① is due to a stitching error during EBL. The structure type with four markers (dots with a diameter of 50 nm) consists of squares

with a side length of 100 nm to 350 nm. The step size between the structures is 50 nm. The SEM image shows a protrusion on the upper left corner of each square. This feature is also visible in the electron reflectivity image (rotated by 135 °). The four markers appear to be connected in the electron reflectivity image which is also visible in some of the structures shown in the SEM image (①). The highlighted area in the electron reflectivity image is shown in Figure 5.21. The detector is situated in the lower left corner of the image, which was taken in the forward scan direction. The count rate drop in the middle of the Ag island in Figure 5.21 is (-12.6±1.4) % while the drop at the right edge of the island, which is caused by electron blocking, is (-25.3±1.0) %. These values and errors have been calculated using linear fits to the count rate on the substrate and Ag island. Electron blocking is also visible at the protrusion at the lower side of the square. The count rate increased at the opposite (bottom and left side) edge of the island while the FE current remains constant. This effect is due to the surface being locally tilted towards the detector and is described in Section 1.4. The lateral resolution of this electron reflectivity image is 25 nm.

The lower reflectivity for elastically backscattered electrons for Ag compared with HOPG is measured consistently at varying FE voltages and currents. This effect is surprising as silver has a higher atomic number ($Z = 47$) compared to carbon ($Z = 6$) and is discussed in Chapter 6.

Figure 5.22 shows the field emission and backscattered electron image of a different sample. The two marker structures of 50 nm diameter are clearly visible in the CR image. They represent the dimer triangle structure illustrated as group ⑤ in Figure 4.12. The triangles in Figure 5.22 appear to be connected. The change in count rate per FE current is (-33.3±2.1) % for the island in the centre of the image. This drop is likely a superposition of a geometrical contrast due to electron blocking at the island and the lower reflectivity of Ag.

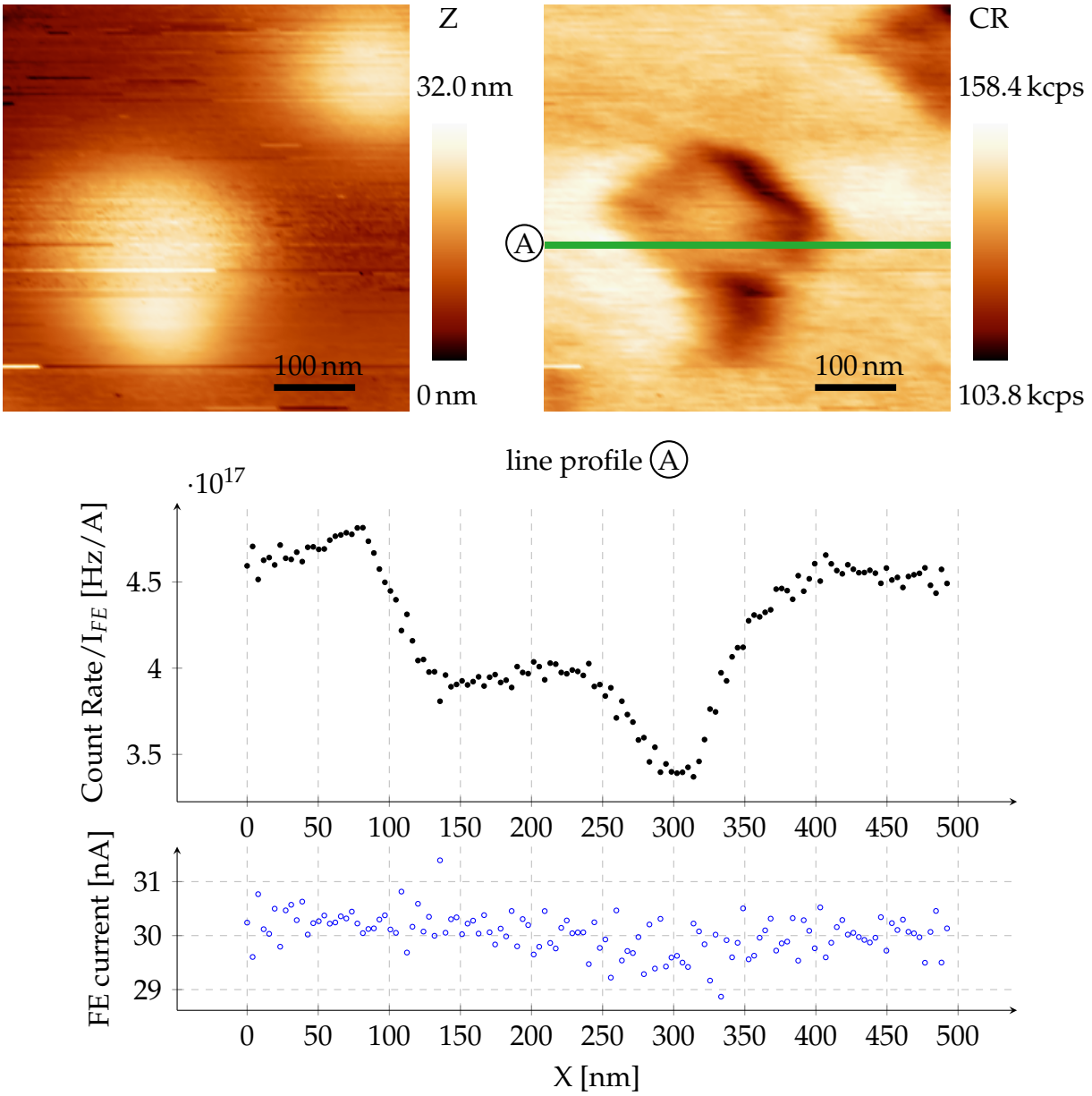


**Figure 5.21:** This electron reflectivity image was taken at a voltage of 55 V, a set point current of 30 nA and a tip-sample separation of 40 nm with the RFA. The retarding voltage was 15 V. The image position is marked in Figure 5.20. All image lines are offset by their line fit. The count rate scale bar values have been offset by the minimum raw count rate on the image before the line fit. The line profile shows raw data. The plateau at lower count rate at the centre of the island is due to the change in the backscattered electron coefficient for the island while the tip at the right is caused by electron blocking. The lateral resolution of the electron reflectivity image is 25 nm.

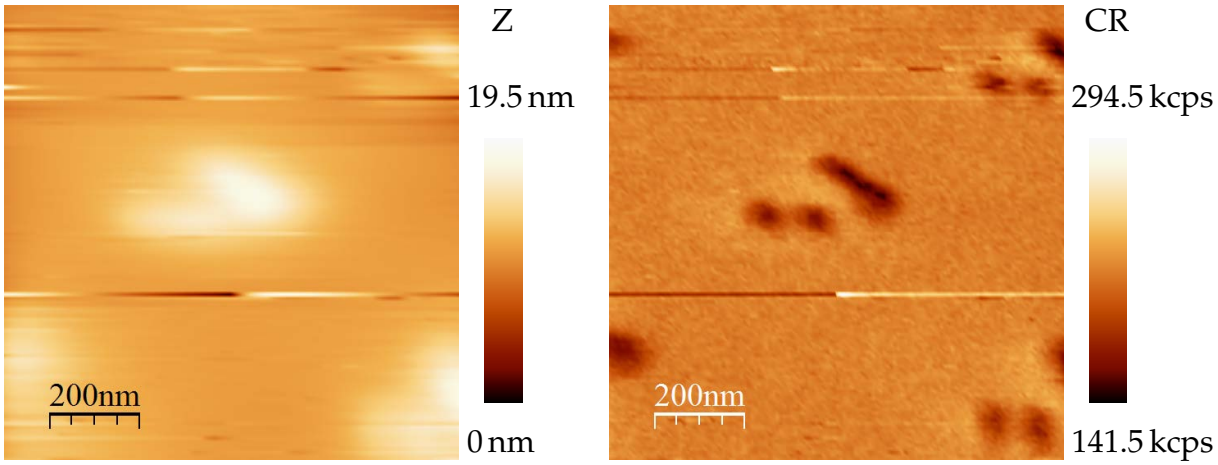


**Figure 5.22:** The left image shows the Z variation during a constant current measurement using a FE voltage of 60 V at a setpoint of 200 nA. The tip-sample separation is 245 nm. The right image shows the corresponding count rate (RFA in pulse counting mode). The scan range is 1 µm and a line fit filter has been applied to both images. The sample has been prepared by EBL on HOPG and a deposition of a 30 nm thick Ag layer. Both markers with a pattern size of $(50 \times 50)\,\mathrm{nm}^2$ are visible next to the structure.

### 5.5.2 Positive reflectivity contrast

To be able to distinguish the geometrical contrast from the backscattered electron contrast, electron reflectivity images from non-silver islands on HOPG are shown below. The following images have been obtained from another sample prepared by EBL and Ag deposition. The surface features do not resemble the EBL pattern and have an increased electron reflectivity compared to HOPG. The imaging parameters are similar to previous measurements were Ag showed a reduced electrons reflectivity. Likely material candidates are residues of the resist (SML-100) or contaminations due to the contact to air (dust).

Figure 5.23 shows an STM height and a FE count rate image of the same area. The pattern of the Ag structures is not visible in the image. The island in the lower left part of the image is 165 nm high which was measured by a linear fit of the averaged areas on the island and of the substrate right of the island. The detector is situated at the lower

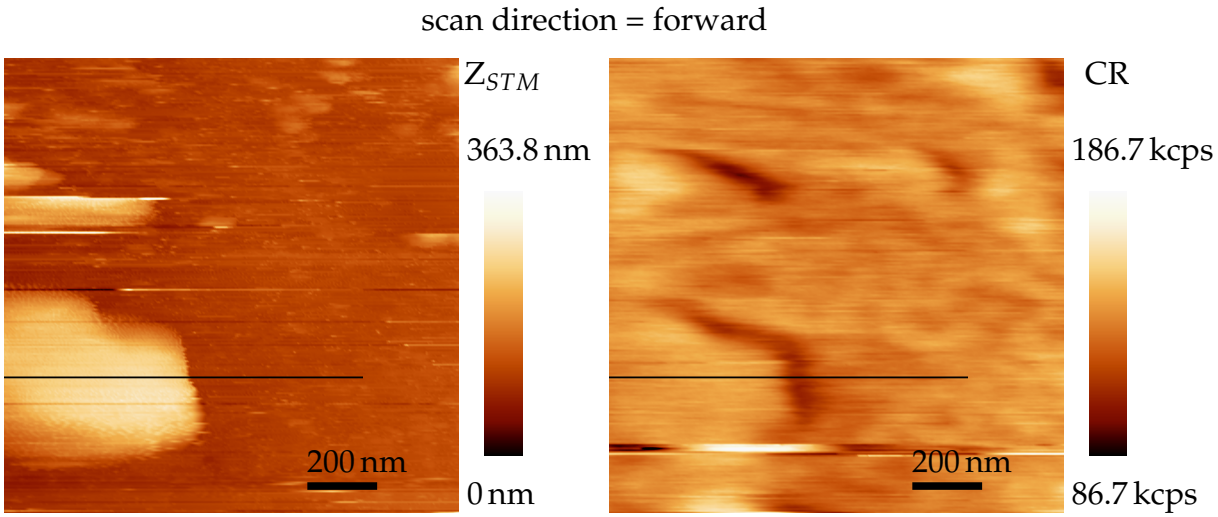


**Figure 5.23:** The left image shows an STM image taken at a tunnelling voltage of -3 V and a current of 300 pA using a linear line fit filter. The sample was prepared by EBL on graphite and the deposition of a 30 nm high Ag layer. The Ag pattern is not visible in the image. The right image shows the electron reflectivity image of the same are for a FE voltage of 60 V at a setpoint of 10 nA and a retarding voltage of 40 V. The tip-sample separation between the images is 470 nm. The scan range is 1.3 µm. The line profiles of the black lines are shown in Figure 5.25.

left corner of the image. The blocking of electrons is visible in the count rate image as a dip in the signal near the right and top edges of the island. The same is true for the backward scan of the same images as shown in Figure 5.24. The black line in the images in Figure 5.23 indicates the position of a line profile taken from both images. The line profiles are shown in Figure 5.25. The line profiles for the backward scan in Figure 5.24 are shown in Figure 5.26. While the images have been filtered by a linear line fit, the profiles show the raw data. The top two graphs show the height profile of the STM and electron reflectivity image followed by the count rate, count rate per current and current profile. The height profile of the STM image is also shown in the other line profiles for comparison. Note that the FE and STM height profiles are shifted to positive Z values. The tip-sample separation, which is the difference between $Z_{STM}$ and $Z_{FE}$ is 470 nm. The electron beam width reduces the lateral resolution and therefore broadens the steep

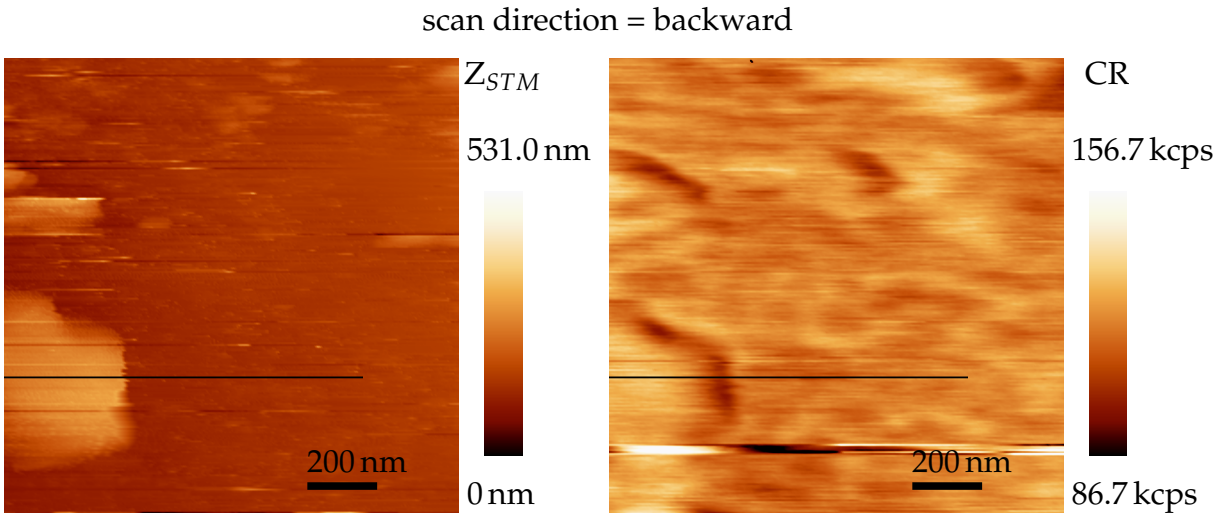


**Figure 5.24:** These are backward scan images from the same measurements as shown in Figure 5.23. The line profiles of the black lines is shown in Figure 5.26. The shift in the island position is caused by the non-linearity of the piezos of the STM at this large scan range of 1.3 µm.

edge of the island as expected.

The level of count rate per FE current from the island rises by (19.6±0.4) % compared with the surrounding substrate. The count rate difference has been calculated by comparison of the linear fits from the left and right side of the island edge from an profile averaged over 25 lines.

The minimum of the dip in the count rate roughly corresponds to the flank of the island but the count rate starts to drop before the edge of the island is reached. The lateral displacement between the onset of the signal drop and the edge of the island is different for the forward and backward scan. A Gaussian fit of the dip in the forward scan has a standard deviation of 20.8 nm and is shifted by 25.4 nm towards the right of the island edge. The corresponding fit for the backward scan has a standard deviation of 30.8 nm and is shifted by 10.6 nm towards the left of the island edge. This is likely due to a shift of the probing area while the tip undershoots during the approach to the island as explained in the following paragraphs.

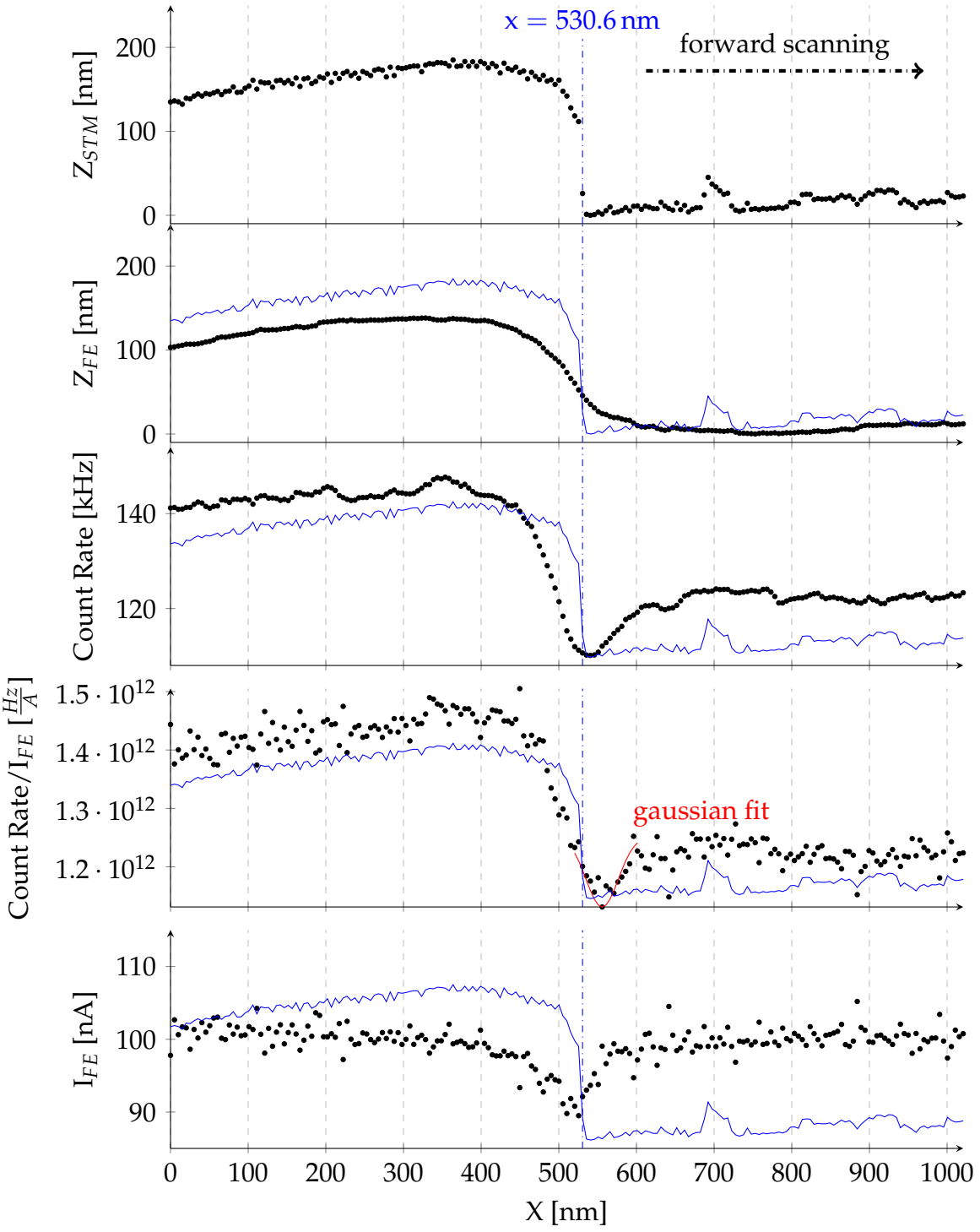


**Figure 5.25:** These profiles have been taken from the black lines marked in Figure 5.23. The blue line in the lower graphs is $Z_{STM}$ from the first scan. The gaussian fit has its center at 556 nm and a standard deviation of 20.8 nm.

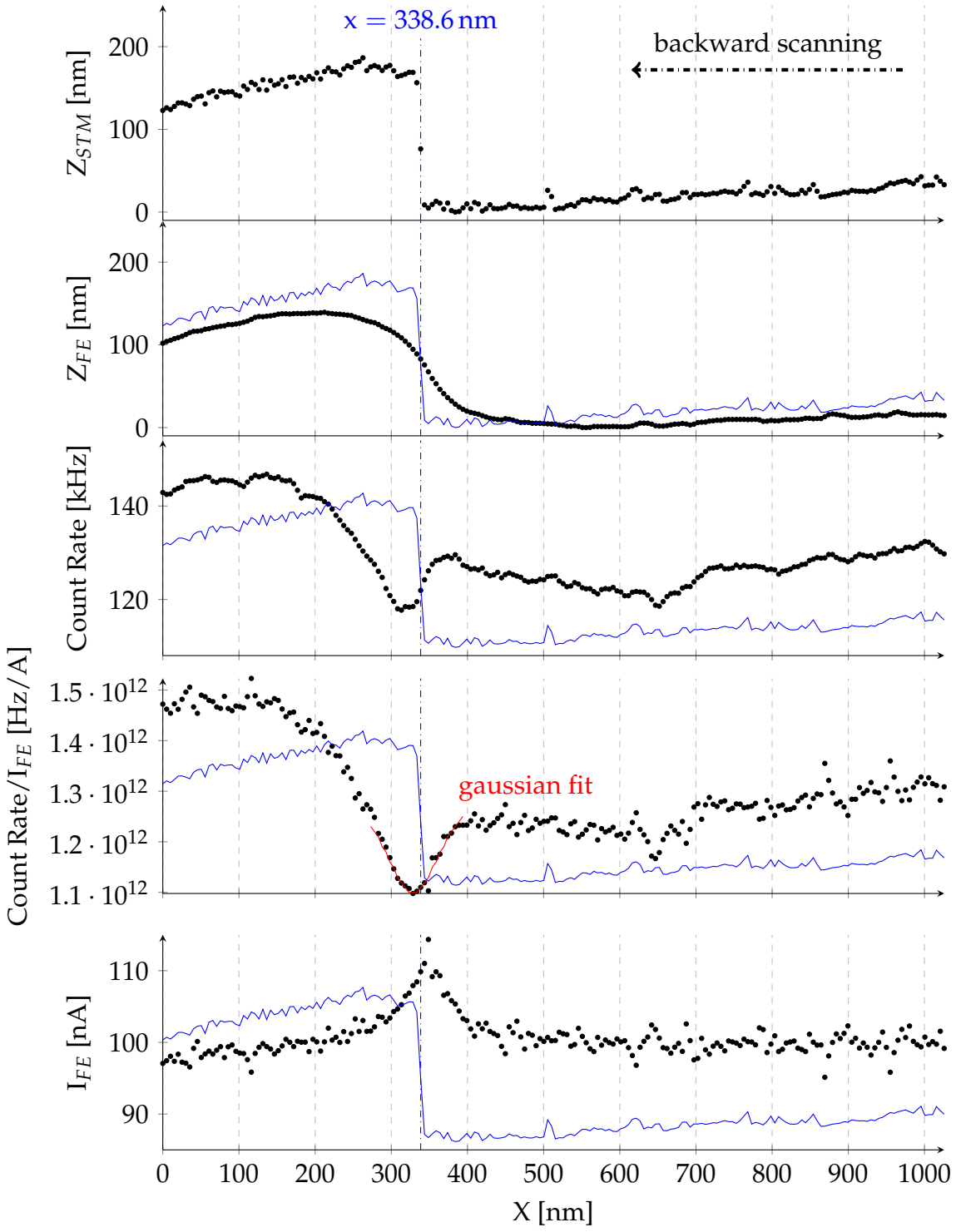


**Figure 5.26:** These profiles have been taken from the black lines marked in Figure 5.24 similar to the profiles in Figure 5.25. The gaussian fit has its center at 328 nm and a standard deviation of 30.8 nm.

First the forward scan, where the tip moves from the top of the island down to the substrate, will be discussed (Figure 5.25). When the tip reaches the edge of the island, the tip-sample separation will increase and weaken the electric field at the tip. Therefore, the emission current drops. This is compensated by the feedback loop which decreases Z but with a finite slew rate. This explains the behaviour of $I_{FE}$ and $Z_{FE}$ but not the count rate per FE current which already compensates for the loss in current. On the other hand, when the tip is still above the island, a part of the electron beam can already reach the substrate when the distance to the edge is smaller than the beam width. Backscattered electrons from this part of the beam would be blocked by the island. However, the area from which backscattered electrons can reach the detector, which was referred to as probing area (PA) in Section 5.2, is located between the tip and the detector and therefore not at this part of the beam. This explains the right shift (by 25.4 nm) of the count rate per current drop which is marked by the Gaussian fit in Figure 5.25.

In the backward scan in Figure 5.26, the FE current increases as the tip starts from the substrate and approaches the island which decreases tip-sample separation and therefore the field intensity at the tip increases. As mentioned earlier, the high island can block electrons and therefore decrease the signal intensity at the edges which do not face the detector direction. However, as the PA is again shifted to the lower left of the image, electrons are not blocked any more once the tip passed the edge of the island. Moreover, the increase in current should lead to higher count rates but the opposite is being measured.

One result from the simulations in Section 5.2 has been that the PA shifts away from the tip position with decreasing tip-sample separation. The FE current is an indicator for the tip-sample separation. In the case of the forward scan the current drops and therefore the tip-sample separation increases while in the backward scan the current

increases leading to a temporarily shorter tip-sample separation. This means that in the backward scan the PA moves away from the tip position where less electrons reach the sample. This is the reason for the offset of the drop in count rate in the backward scan in Figure 5.26.

Another influence in STM measurements is the non-linearity of the piezo movement. The difference in the absolute position of the island edge is due to piezo effects (nonlinear extension and creeping) which are noticeable in this large scan range. As the island is on the left side of the image it appears compressed horizontally in the backward scan while it appears stretched in the forward scan. Therefore, the distance between the drop in count rate and the edge of the island is bigger in the forward scan and smaller in the backward scan. However, the change in the relative position of the drop from right to left of the island edge cannot be explained by piezo effects.

To emphasize this effect, an electron reflectivity image from another sample is shown in Figure 5.27, which was taken using the MCA. The sample was prepared by EBL on HOPG with Ag evaporation. No EBL pattern is visible in the image. The island in the lower part of the electron reflectivity image is 190 nm high and the image was taken during a forward scan. An averaged line profile Ⓐ over the 4 lines marked in the image is also displayed in Figure 5.27. As the tip approaches the island, the FE current increases and the tip starts to retract. However, the count rate per current decreases while the FE current is high which is marked by Ⓑ in the image. This behaviour can again be described by a shift of the PA towards lower intensities of the electron beam distribution. The backscattered electron signal on top of the island is slightly increased (less than 10 %) which allows to measure this effect. The right side of the island shows the expected geometry contrast, blocking the backscattered electrons.

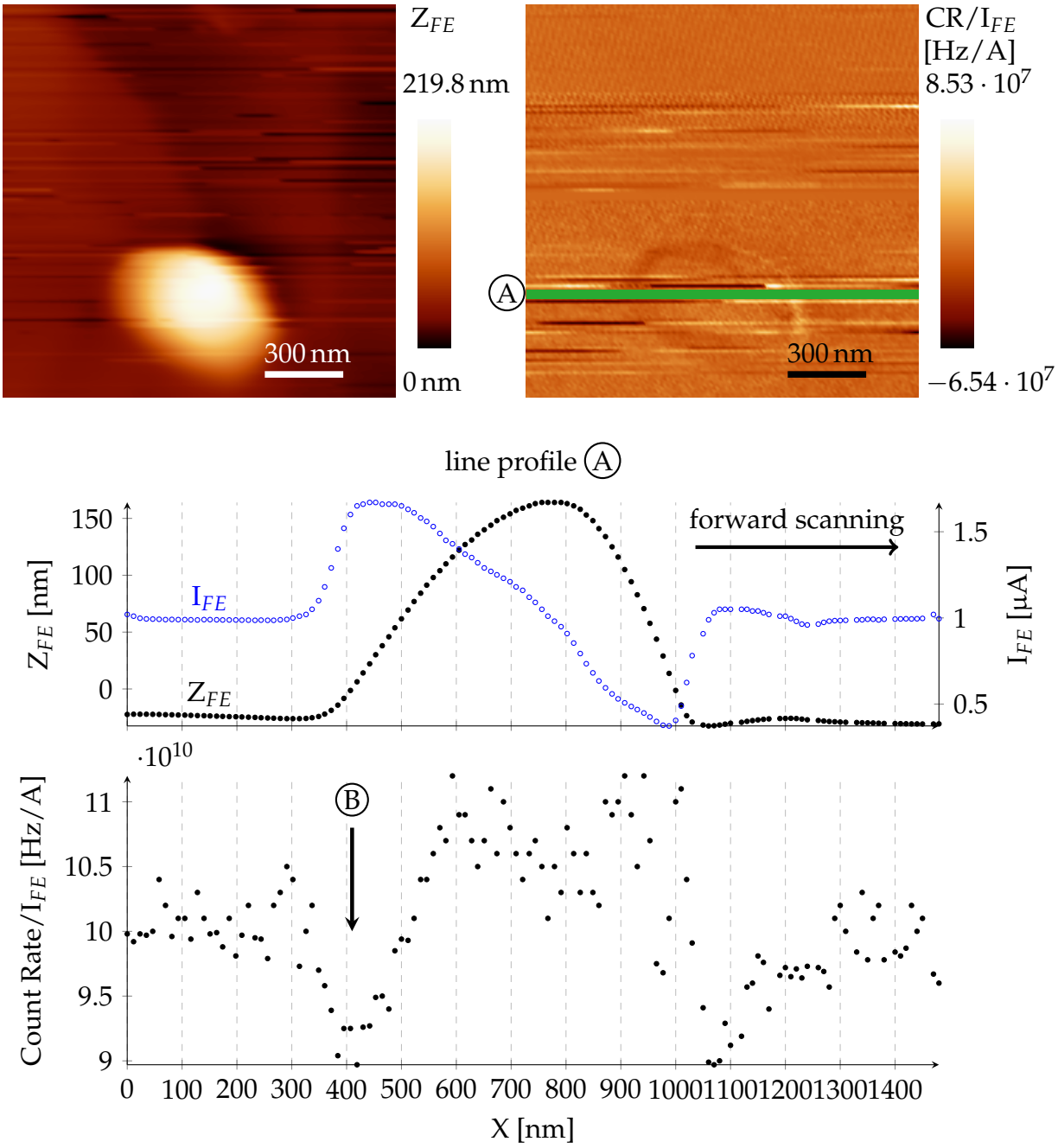


**Figure 5.27:** This electron reflectivity image was taken with the MCA at a voltage of 45 V and a current setpoint of 1 µA. The scan range is 1.5 µm. The line profiles from (A) show the FE voltage and current as well as the count rate per current. (B) indicates the count rate dip due to the shift of the PA.

## 5.6 Nonlinear Field Effects

In August 2014 C. K. Xu *et al.* published their work regarding field enhanced inelastic scattering at Ag nanoparticles [108]. They use a toroidal analyser around an STM to capture electrons over a wide angle from the sides of an STM (see ① in Figure 5.28). They report a nonlinear increase in the intensity of the Ag plasmon loss peak at high

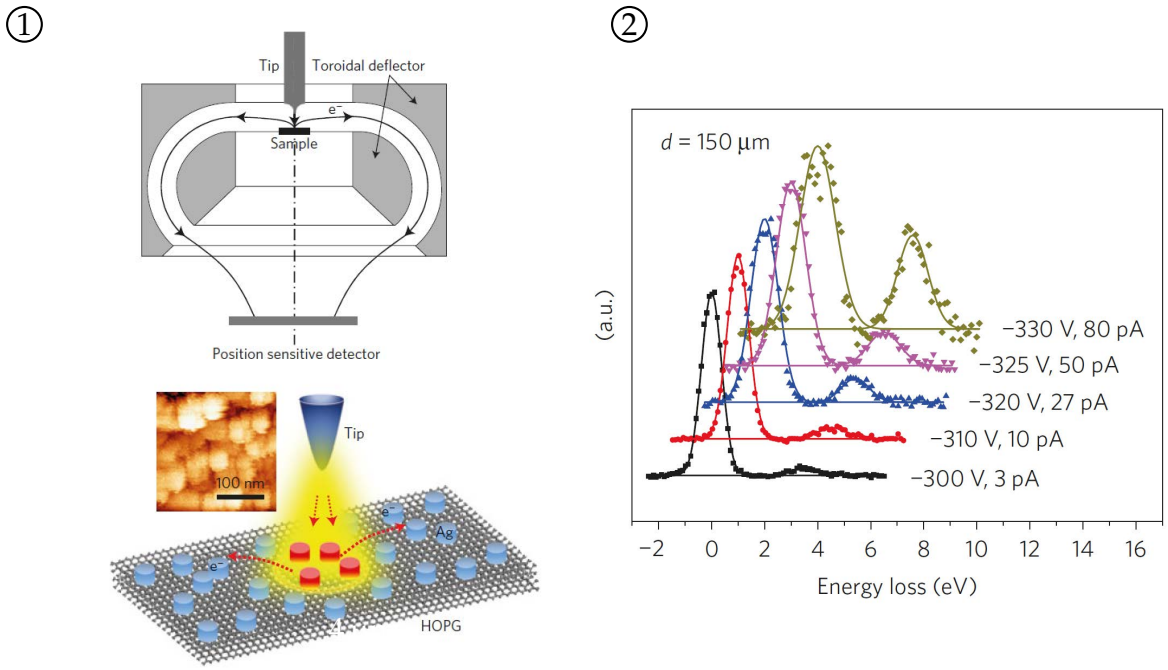


**Figure 5.28:** ① shows the setup using the toroidal analyser. ② shows the FE voltage effect on the intensity of the plasmon loss peak. Both images were taken from [108].

FE voltages up to 60 % of the elastic peak, but no spatial plasmon maps have been presented. Their results were reported from a sample consisting of a 10 nm thick Ag layer on HOPG, which resulted in clustered Ag islands. They could not measure the effect on thicker Ag layers and argued that a high amount of "hot spots", the small gaps between Ag nanoparticles, are only present in the thinner Ag layers and are necessary to observe this effect.

Such an increase in the loss peak would also be visible with the RFA. Therefore,

SPELS with the RFA (3 mm aperture) was used on a sample prepared by EBL, a sample consisting of a thick Ag layer on mica and a sample consisting of a 10 nm high Ag layer on HOPG. Only the 10 nm thick Ag film sample has shown a dependence on the voltage as shown in Figure 5.29. A broad energy loss peak, centred around 2.5 eV, appears with increasing FE voltage from 210 V to 240 V. As the tip position was held constant, the FE current and the count rate increased with higher voltage, but the count rate per current decreased. The energy of the loss peak differs from the position of the Ag plasmon peak at 3.8 eV, which has been measured before. As the RFA does not need to be calibrated there is no risk in distorting data as with the MCA (see Figure 5.9). However, more experiments need to be conducted to confirm their findings and to get meaningful statistics about this effect and its dependence on the Ag film structure.

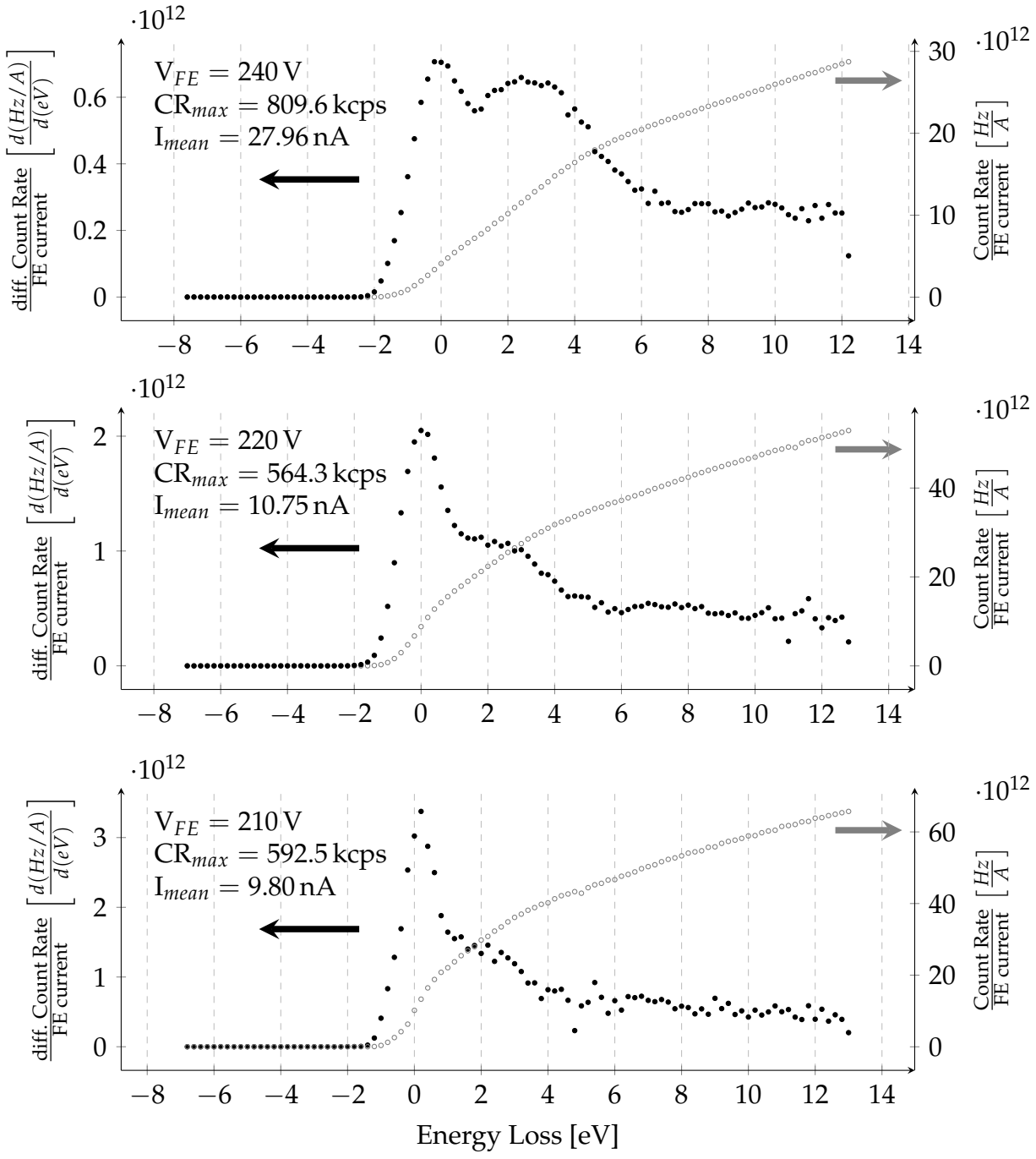


**Figure 5.29:** These spectra have been obtained in succession at the same tip position using the RFA. The FE voltage, count rate and current for each spectra are displayed in the graphs. The current variations during the measurements are compensated by dividing the count rate by the FE current and the differentiated data is smoothed using a moving average filter with a span of 3.

## 5.7 Summary

In summary, the RFA allows one to work regularly at 1 to 2 orders of magnitudes higher signal intensity compared with the MCA. However, this does not fully compensate for the loss in signal to noise due to the retarding field design e.g. the analyser being a high pass filter rather than a band pass filter. This prevents the mapping of plasmon loss features but still allows the detection of backscattered and secondary electrons. The measurement of the local contrast in electron reflectivity helps to identify surface features. The RFA is much easier to set up than the MCA as there are no electron optics that have to be tuned. Imaging in FE mode means that the tip is safe from surface impacts even at the largest scan range at a high scan speed where STM images would break the tip. It is therefore useful as a tool to find bigger structures on a sample if the sample is resistant to the low energy electron beam. However, to achieve high resolution EELS spectra for SPELS a band pass filter analyser, such as the MCA, is necessary. This is due to the low intensity of the plasmon peak compared with the elastic peak at higher absolute energy. With the MCA, plasmon loss features of Ag, Au and graphite as well as spatial plasmon maps have been measured. The shift of the PA as simulated in Section 5.2 has been observed experimentally with both detectors.

Chun Kai Xu *et al.* reported recently enhanced plasmon loss peaks of up to 60 % of the elastic peak at high electric fields between a tip in field emission mode and Ag nanostructures [108]. First attempts to verify their work have shown an increase in the intensity of a loss peak at 2.5 eV, but further experiments are necessary to verify these results.

# Chapter 6

# Summary and Outlook

## 6.1 Summary

In this study of scanning probe energy loss spectroscopy (SPELS) of structured surfaces, the capabilities of the instrument were developed and investigated. This technique requires the optimisation of the field between tip and sample by controlling the tip shape and scanning conditions to improve the signal intensity of backscattered electrons. High tip stability under field emission is necessary for a successful measurement. The best resolution of 25 nm is achieved for close proximity between the tip and sample of below 300 nm. The energy of the probing electrons is defined by the FE voltage that is applied to the tip subtracted by the work function of the tungsten tip of 4.5 eV. The maximum FE voltage is limited by the FE current the tip can withstand without becoming unstable or blunt. To achieve sub 100 nm resolution it is necessary to work with FE voltages of less than 100 V. Higher energy levels are possible but this sacrifices lateral resolution. The energy resolution of the instrument in the current state is limited by the energy distribution of the field emitted electrons which is 0.3 eV. Surface plasmons of Ag and Au have energies of about 3.6 eV and 4.8 eV and are therefore accessible by SPELS. Electron reflectivity images of nanostructures with controlled sizes down to 50 nm have been routinely acquired for the first time.

In this chapter the work that has been presented in the previous chapters is summarised and desirable future studies are discussed.

## Development of SPELS Instrument

The configuration of the instrument as well as tip and sample preparation methods have been revised and extended as explained in Chapter 3. A new electron detector based on the retarding field principle, and using a CEM, has been built as a replacement for the MCA. The compact design of the analyser means that the distance between sample and the CEM can be reduced to 38 mm. Both pulse counting mode and analogue mode for the CEM have been implemented and used for SPELS. SIMION was used to simulate electron trajectories in the RFA and to assess the dependence of the energy resolution on the size of the entry aperture. With the RFA, count rates up to the limit of the ratemeter of 1 MHz are routinely observed in pulse counting mode. The analogue mode allows an even higher count rate, but at a higher noise level.

Important imaging parameters, like energy distribution and tip-sample separation at a given FE voltage and current, depend on the tip condition. Tips, that have been prepared and characterised by SEM during this study, were used for a quantitative statistic about the success rate of various etching parameters. These measurements show that etching voltages above 4 V are preferable for gaining suitably sharp tips for SPELS. The addition of the tip conditioning stage to the vacuum system allows for *in situ* tip preparation with a variety of methods. Field emission at high current as a preparation method has been used as standard procedure to prepare tips. Additionally, field-surface-melting, self-sputtering and e-beam heating have been tested. Furthermore, the addition of this stage allows the field emission stability of the tips to be tested before they are loaded into SPELS. A LabView program has been written to control the high voltage power

supply used in these methods and to log and automatise the experiments. Tips that emit a FE current of 1 μA at a stable FE voltage of 1000 V or below show a good backscattered electron signal in SPELS at much lower currents.

During this study a large amount of measurements have been performed which would not have been possible without custom control software. Software has been written to control SPELS with the MCA, with the RFA, to perform custom experiments, to analyse SPELS data and to control tip and sample preparation.

## Creation of Nanostructured Surfaces

In Chapter 4, the sample preparation of silver and gold nanostructures on HOPG has been discussed. EBL proved to be the most reliable and versatile preparation method. The ability to control the film thickness during metal evaporation was necessary for samples prepared by EBL, due to the limited resist thickness. A home-built evaporator, with water cooling, shutter and integrated quartz crystal monitor providing a high degree of control over metal deposition, has been added and used to prepare samples *in situ* and for EBL samples.

For EBL, a positive resist together with a lift-off process have been used to create Ag and Au structures on HOPG down to a size of 50 nm. The limitation in lateral sample movement to the horizontal axis in SPELS requires a macroscopic sample (several $mm^2$) area to be patterned. Only then is it feasible to find nanostructures on the sample. The EBL pattern layout has been optimised to increase the area covered with nanostructures. The geometries of nanostructures include a variety of sizes and distances between dimers and trimers to generate different degrees of plasmon coupling.

## SPELS Performance and Images of Nanostructured Surfaces

In Chapter 5, the performance of SPELS has been described in dependence of various measurement parameters. SIMION simulations of the tip-sample junction in SPELS have also been performed with the intention to determine how the probing area, only from which backscattered electrons reach the detector, changes with the tip-sample separation. It has been found that the tip-sample separation is inversely proportional to the offset of the probing area from the tip position. As every tip has a different shape this result has only a qualitative character but demonstrates an underlying mechanism.

Spatial maps of backscattered electrons have been presented and analysed. Spatial plasmon mapping has been achieved in case of the MCA on a large (around 500 nm high) island of Ag on HOPG. For spatial plasmon maps, the count rate per FE current has to be normalised against the local reflectivity. The normalised count rate around the Ag plasmon peak (3 eV to 4.5 eV) is correlated to the highest Ag islands.

The total backscattering rate, e.g. the elastic peak height, appears to be lower on Ag than on HOPG, which has been measured with both the MCA and the RFA on several samples. This is counter intuitive as the backscattered electron coefficient is higher for heavier elements like Ag ($Z = 47$) compared to carbon ($Z = 6$). HOPG has a higher atomic density per surface area (factor 3.18) and per volume (factor 1.94) compared to a Ag crystal. But the theoretically difference for the backscattering coefficient is by a factor of 6.02 higher for Ag compared to carbon[1] [109]. However, this calculation is based on measurements using electron energies of several keV. Assa'd and Gomati measured the backscattering coefficient for electron energies as low as 500 eV [110]. They found that the coefficient decreases for materials with $Z > 20$ and samples that have not been cleaned *in situ* as shown in Figure 6.1. A reduced backscatter coefficient

[1] using $E_0$ =100 eV

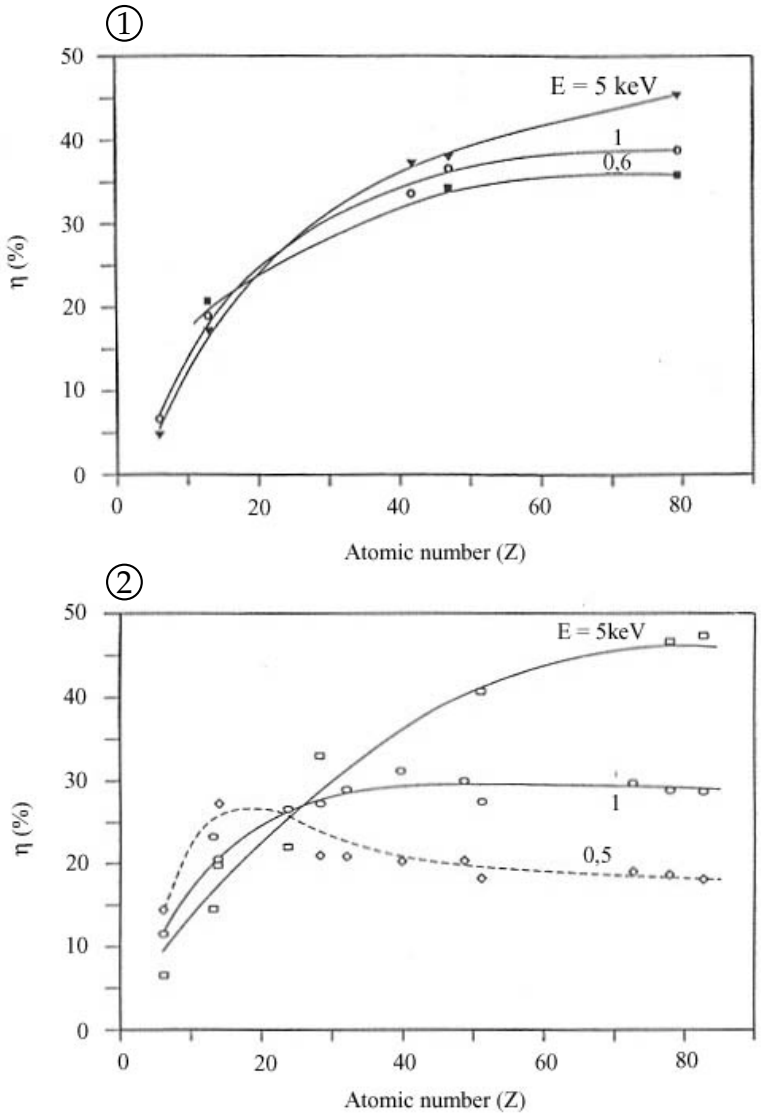


**Figure 6.1:** The backscattered electron coefficient was measured for materials with different atomic numbers and at various electron energies. ① for samples that have been cleaned *in situ* by Ar ion sputtering. ② for samples that have been used as inserted in the vacuum chamber. The coefficient decreases at lower electron energies (500 V) for species with higher (>20) atomic numbers. (taken from [110])

for lower electron energies could explain the contrast visible in SPELS images.

Measurements with the MCA on small silver islands at HOPG step edges and nanostructures prepared by EBL have been presented. However, the signal level of smaller Ag islands was insufficient to generate spatial plasmon maps but showed contrast in

electron reflectivity between Ag islands and graphite. The ability of the MCA to cover a wide range of electron energies in parallel has attendant risk of distortion of data by wrong detector calibration. This issue has been addressed and an experimental procedure to avoid these problems has been discussed.

The RFA showed insufficient signal to noise levels to show plasmon peaks as their signal is measured on top of the high signal from the elastic peak. However, the overall count rate is up to two magnitudes higher compared with the MCA. Electron reflectivity maps that show a contrast between Ag and HOPG have been obtained with the RFA. The reflectivity from Ag has consistently been lower than that from HOPG. The change in reflectivity allows to distinguish between Ag islands and other surface features on the sample. Experimental evidence has been found for the results from SIMION simulations for the position of the probing area adding to our understanding of the contrast mechanism in SPELS images.

The increase in intensity of a loss feature at 2.5 eV with higher FE voltage demonstrates that the RFA can be used to measure loss features with high intensity. However, further experiments need to be carried out to verify the results of C. K. Xu (see *et al.* [108]).

## 6.2 Outlook

This study of SPELS has shown interesting possibilities but also limitations of the technique regarding spatially resolved images. Higher electron energy has to be traded against spatial resolution, which limits accessible surface excitations. Surface plasmons of nanostructures are an interesting subject to study. The contrast in reflectivity demonstrates that the lateral resolution of the instrument is sufficient but the signal to noise ratio has to be increased to achieve reliable spatial plasmon mapping.

The electron reflectivity contrast should be investigated for materials with different atomic numbers than silver (e.g. copper and gold) and for various electron energies. The dependence of the backscattered electron signal on the electron mean free path in the sample could be investigated by thin film bi- or tri-layers. This could also investigate the surface sensitivity of SPELS in dependence of the electron energy. At higher electron energies, the measurement of loss signals from sub-surface layers should in principle be possible.

More experiments on the 10 nm thick Ag layer at high FE voltages should be conducted to investigate if the increase in the intensity of the loss peak can be assigned to the nonlinear field effect as proposed in [108]. It would also be interesting to investigate whether this effect can be seen with other materials like Au.

### 6.2.1 Towards next generation SPELS

The RFA had an insufficient signal to noise ratio at the plasmon energies but a high overall signal intensity, while the MCA had superior energy resolution but at a low signal. As the maximum energy resolution of the MCA of 2 meV is not needed for SPELS, a smaller cylindrical sector or other band pass filter type analyser could be used. A compact analyser of this type could be placed nearly as near to the sample as the RFA, although the distance to the detector (e.g. CEM) would be larger. The LK1000, a smaller brother of the analyser (ELS5000) used at the beginning of this work, could be used for this purpose. It has a radius of 35 mm and would fit between the support columns of the Omicron STM-1, this has been shown by a CAD drawing. Together with the already established tip and sample preparation methods, this could lead to spatial resolution plasmon maps with a high signal.

# Appendices

# Appendix A

# Derivation of the Spot Size of the Evaporator

The dimensions of the aperture of the evaporator and the assumed position of the crucible below the aperture is shown in Figure A.1. The diameter of the evaporation

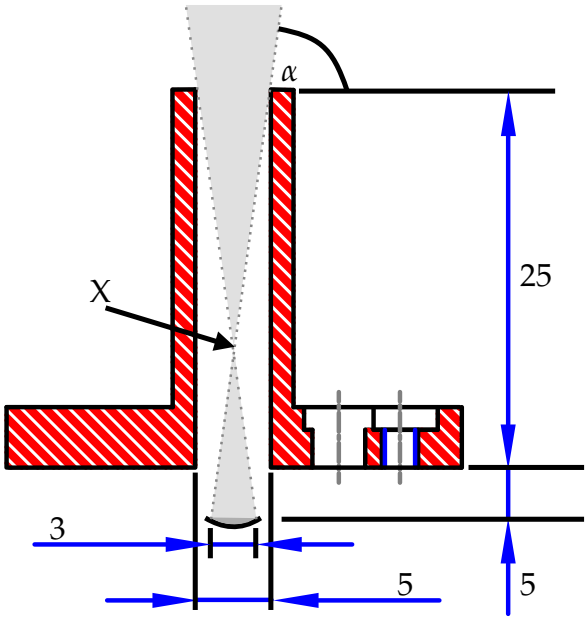


**Figure A.1:** Schematic of the aperture of the evaporator. All dimensions in mm.

source is approximately 3 mm and the source is centred 5 mm below the aperture. The angle $\alpha$ is the tangent from the distance between the crucible and the end of the evaporator and the distance from one end of the crucible to the alignment of inner wall

of the aperture:

$$\tan\alpha = \frac{30}{4}. \tag{A.1}$$

If $h$ is the distance from crosspoint X in the image to the upper end of the aperture then $\tan\alpha$ is

$$\tan\alpha = \frac{30-h}{1.5} \tag{A.2}$$

and with $\beta = 90^\circ - \alpha$ the spot diameter $S$ at distance $d$ is

$$S(d) = 2\cdot(h+d)\cdot\tan\beta = 2\cdot(-1.5\cdot\tan\alpha + 30 + d)\tan\beta. \tag{A.3}$$

# Appendix B

# Set up of Electron Lens Voltages

The ID's of the virtual lens voltages as well as their DAC and voltage ranges were listed in Table B.1.

**Table B.1:** Range of DAC values and lens voltages. Note that the length of the binary representation is different for different voltages.

| | | maximum values | | minimum values | |
|---|---|---|---|---|---|
| ID | Lens | DAC | Voltage | DAC | Voltage |
| 24 | Window | 65000 | 1,646 | 0 | 0,000 |
| 25 | AN1 | 65000 | 26,308 | 0 | 0,001 |
| 26 | B4 | 65000 | 21,018 | 0 | -5,302 |
| 27 | E1 | 65000 | 88,442 | 0 | 0,000 |
| 32 | B3 | 65000 | 127,822 | 0 | -6,783 |
| 33 | E0 | 65000 | 82,801 | 0 | -14,781 |
| 34 | ExitGrid | 65000 | 4,955 | 0 | -5,321 |
| 40 | ^B4 | 4080 | 2,636 | 0 | -2,651 |
| 41 | ^E1 | 0 | 2,404 | 4080 | -2,500 |
| 54 | Offset | 4080 | 2,641 | 0 | -2,659 |
| 55 | ^AN1 | 4080 | 25,393 | 0 | 0,001 |
| 57 | E2 | 4080 | 9,867 | 0 | -9,981 |
| 61 | ^E2 | 0 | 2,474 | 4080 | -2,596 |
| 52 | E1 ramp | 4080 | 1,984 | 0 | 0,000 |
| 42 | B3 ramp | 4080 | 1,689 | 0 | 0,000 |
| 51 | B4 ramp | 4080 | 1,980 | 0 | 0,000 |
| 56 | Beam | 0 | 16,267 | 4080 | -244,991 |
| 53 | Win-mult | 4080 | 31,875 | 0 | 0,000 |

The conversion formula for the transition from a DAC value to a virtual lens voltage V is

$$V = V_0 + \text{slope} \cdot (\text{DAC} - \text{DAC}_0)\,. \tag{B.1}$$

The coefficients $\text{DAC}_0$ and $V_0$ are listed in Table B.2. The conversion formulae from the

**Table B.2:** Coefficients of the conversion formula between DAC values and virtual lens voltages.

| | Coefficients of the conversion formula | | |
|---|---|---|---|
| Lens | $\text{DAC}_0$ | $V_0$ | slope |
| Window | 39623 | 1,0036215000 | 2,5329265830E-05 |
| AN1 | 7432 | 3,0106650000 | 4,0469060960E-04 |
| B4 | 50056 | 14,9670600000 | 4,0491894767E-04 |
| E1 | 4434 | 6,0333930000 | 1,3606422423E-03 |
| B3 | 12987 | 20,1113100000 | 2,0708344973E-03 |
| E0 | 16540 | 10,0499151000 | 1,5012509110E-03 |
| ExitGrid | 30481 | -0,5020620000 | 1,5808014960E-04 |
| ^B4 | 2046 | 0,0000587527 | 1,2958908997E-03 |
| ^E1 | 2000 | 0,0000551789 | -1,2020574759E-03 |
| Offset | 2820 | 1,0041150000 | 1,2989844760E-03 |
| ^AN1 | 777 | 4,8367200000 | 6,2236081080E-03 |
| E2 | 3087 | 5,0359500000 | 4,8646869959E-03 |
| ^E2 | 1991 | -0,0001143648 | -1,2425259674E-03 |
| E1 ramp | 2056 | 1,0000000000 | 4,8638132300E-04 |
| B3 ramp | 2415 | 1,0000000000 | 4,1407867500E-04 |
| B4 ramp | 2061 | 1,0000000000 | 4,8520135900E-04 |
| Beam | 567 | -20,0400000000 | -6,4033865800E-02 |
| Win-mult | 128 | 1,0000000000 | 7,8125000000E-03 |

virtual lens voltages to the actual lens voltages are

$$\begin{aligned}
\mathit{Beam} &= \text{Beam} \\
\mathit{E2\,RT} &= |\text{Beam}| + \text{E2} + \frac{1}{2} \cdot \text{^E2} \\
\mathit{E2\,LT} &= |\text{Beam}| + \text{E2} - \frac{1}{2} \cdot \text{^E2} \\
\mathit{E1\,UP} &= \text{E1} + \frac{1}{2} \cdot \text{^E1} + \text{E1 ramp} \cdot (\text{Window} \cdot \text{Win-mult} + \text{Offset})
\end{aligned}$$

$$E1\,DN = \text{E1} - \frac{1}{2} \cdot \hat{}\text{E1} + \text{E1 ramp} \cdot (\text{Window} \cdot \text{Win-mult} + \text{Offset})$$

$$E0 = \text{E1} + \text{E0} + \text{E1 ramp} \cdot (\text{Window} \cdot \text{Win-mult} + \text{Offset})$$

$$B3 = \text{B3} + \text{B3 ramp} \cdot (\text{Window} \cdot \text{Win-mult} + \text{Offset})$$

$$B4\,UP = \text{B4} + \frac{1}{2} \cdot \hat{}\text{B4} + \text{B4 ramp} \cdot (\text{Window} \cdot \text{Win-mult} + \text{Offset})$$

$$B4\,DN = \text{B4} - \frac{1}{2} \cdot \hat{}\text{B4} + \text{B4 ramp} \cdot (\text{Window} \cdot \text{Win-mult} + \text{Offset})$$

$$AN1\,IN = \text{AN1} + \frac{1}{2} \cdot \hat{}\text{AN1} + \text{Window} \cdot \text{Win-mult} + \text{Offset}$$

$$AN1\,OUT = \text{AN1} - \frac{1}{2} \cdot \hat{}\text{AN1} + \text{Window} \cdot \text{Win-mult} + \text{Offset}$$

$$EXIT\,GRID = \text{ExitGrid} + \text{AN1} + \text{Window} \cdot \text{Win-mult} + \text{Offset}$$

# Appendix C

# Characterisation of Tips and Samples: AFM and SEM

The following techniques were used to characterize samples and tips before they are introduced into the UHV chamber of the SPELS instrument.

## C.1 AFM

AFM allows the imaging of the topography of an insulating or conducting surface by a probe tip. This technique was used to characterize samples. The schematic of the setup is displayed in Figure C.1.

The AFM tip is fabricated on a small flexible bar which is called a cantilever. The movement of the cantilever is realised with piezo crystals. As the tip is pressed gently on the surface, the displacement of the cantilever is measured with a laser beam which is reflected from the back side of the cantilever and detected by a 4-part photodiode. The difference in current generated by the four independent parts of the photodiode provides an accurate measurement of the laser spot position.

The cantilever can scan the sample in three different modes. These are the "contact mode", the "non-contact mode" and the "tapping mode". The force with respect to the

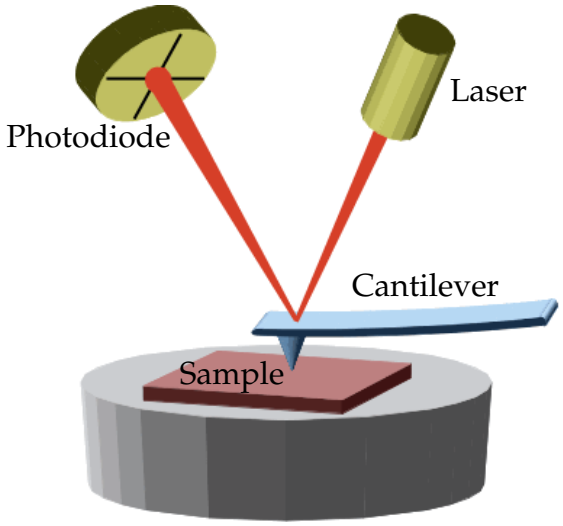


**Figure C.1:** Schematic of the principle of an atomic force microscope (taken from [111]).

tip-sample separation is displayed in Figure C.2. During the contact mode the tip is pressed on the surface with a repulsive force, which is marked in Figure C.2 by the red area. As the tip follows the surface topography, so does the displacement of the cantilever which is detected as the deflection of the laser beam. A feedback loop reacts to these changes by adjusting height of the cantilever so that the force on the sample is constant. The variations in Z provide an image of the surface topography. Alternatively, the height of the tip is held constant while the displacement of the cantilever together with its spring constant provides a measurement of the forces on the tip. With an electrically conductive tip working in the contact mode the local conductivity of the sample can be measured parallel to the topography. This method is called "conductive AFM". The contact mode has the disadvantage that sensitive samples could be damaged or manipulated by the force applied by the tip. In the case of thin films, the tip could lift the film which would result in the distortion effect described in Figure C.3.

This can be avoided using the non-contact mode. This mode utilises the attractive van der Waals forces. These forces are too small to be measured directly by a displacement of the cantilever. So the tip is forced to oscillate with a frequency right next to the resonant

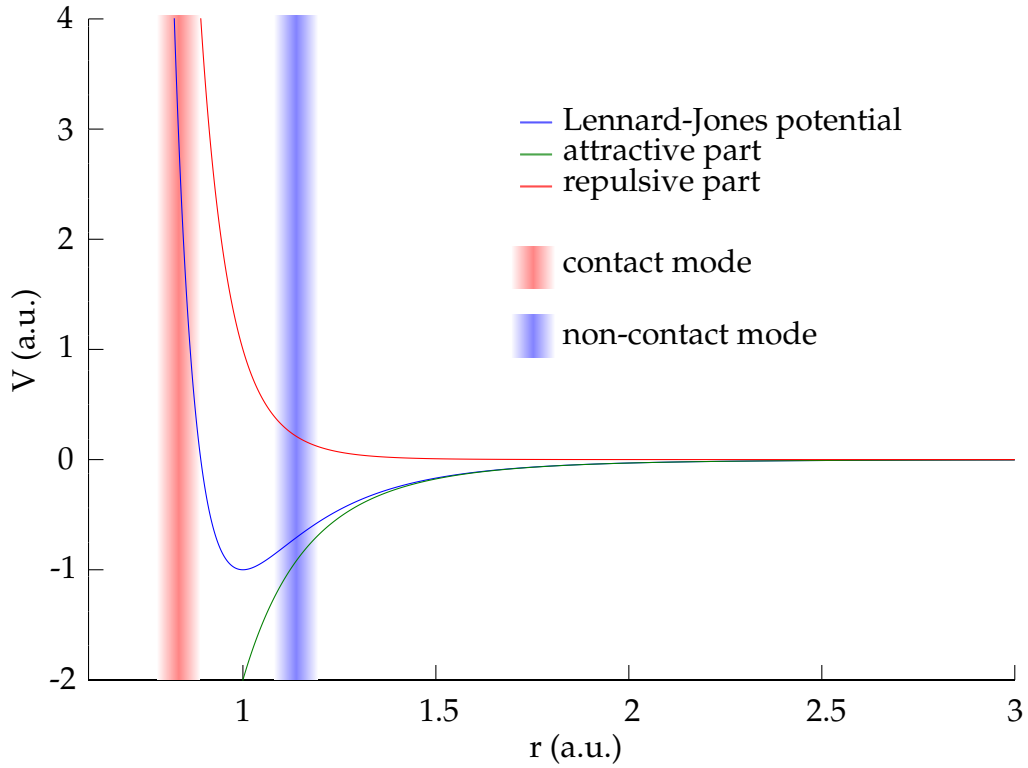


**Figure C.2:** Example of the Lennard-Jones potential. The displayed equation is: $((1/x)^{12}) - (2 \cdot (1/x)^{6})$. The red area indicates the range of the contact mode, where the force on the tip is repulsive. The blue area marks the range of the non-contact mode, where the force on the tip is attractive.

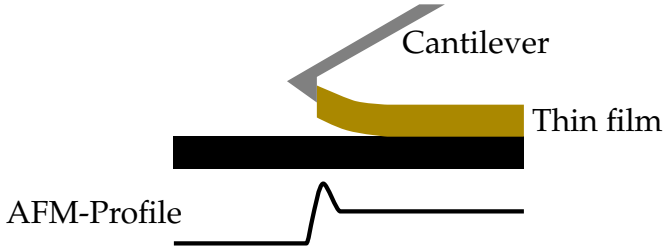


**Figure C.3:** Schematic of distortion effect of AFM tip induced force on thin films on a surface.

frequency of the cantilever by the Z piezo crystal. When the tip approaches the sample, the resonant frequency of the cantilever decreases due to attractive van der Waals forces between the sample and tip. This changes the gap between the resonant frequency and

the operating frequency and therefore the amplitude of the oscillation changes. This signal is high enough to be measurable. In contrast to the contact mode, the tip does not apply any lateral force on the sample. A limitation of this measurement mode is that the natural liquid film on a sample measured in air can be higher than the range of the van der Waals forces so that the actual topography of the sample can not be resolved.

The tapping mode is an approach to combine the advantages of both measurement modes described above. In this mode the tip is forced to oscillate with a frequency near the resonant frequency. This leads to oscillation amplitudes up to 20 nm. The tip-sample separation is then reduced so far that a repulsive force appears on the tip at the lower reversal point of the oscillation which reduces the amplitude. The height is then varied to keep that amplitude constant during a scan. Recording the z-position of the tip then leads to an image of the topography.

The AFM has the same limitations as STM in imaging features with a high aspect ratio due to the tip size as described in Chapter 1.2. The AFM was used in non-contact mode in this work.

## C.2 SEM

SEM scans the surface with an electron beam whilst measuring the emitted secondary electrons to reveal a topographic image of a surface. This technique does not perform an energy resolved measurement of the secondary electrons but the wide range of magnifications from the millimetre down to the nanometre regime was used to characterize STM tips for SPELS and samples.

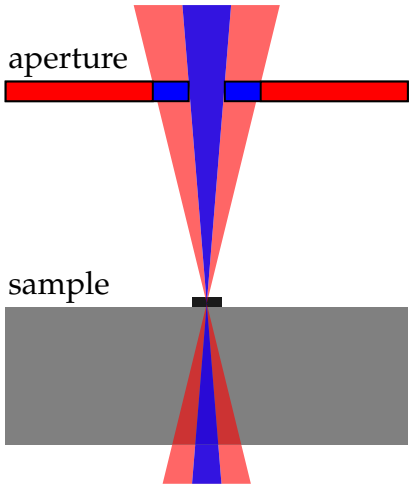


**Figure C.4:** Schematic of the electron beam with big (red) and small (blue) aperture.

The images are typically in gray scale with brighter areas corresponding to higher electron count rates. The contrast mechanism is due to the fact that the number of electrons reaching the detector is dependent on the surface orientation, structure and material. Secondary electrons with a high normal velocity component are more likely to leave the sample [112]. Hence, if the normal of a surface is facing the detector it appears brighter while a surface with a small angle to the detector appears darker. Sharp edges have a higher local surface and allow more electrons to leave the sample and appear therefore bright in SEM images. The depth of focus can be influenced by the aperture size of the SEM and by the working distance between the electron lens system and the sample. A bigger aperture will lead to a higher current and therefore a higher signal to noise ratio, but it will also decrease the depth of focus as it is displayed in Figure C.4. A bigger working distance increases the depth of focus but decreases resolution.

If the rate of charge dissipation in the surface is low the electron beam will charge the sample locally, which is visible in subsequent images. A feature is always measured by

starting with a low magnification to avoid this effect. Also, calibration steps are taken far away from interesting sites on the sample.

The SEM has also the capability to produce structures on surfaces. This is either done by electron beam lithography or by maskless electron beam induced deposition (EBID) [113]. With these methods structures in the nanometre regime can be produced.

The SEM instrument used in this work is described in Section 3.2.3.1.

# List of References


[1] Müller, E. W. (1956) Resolution of the Atomic Structure of a Metal Surface by the Field Ion Microscope. **J. Appl. Phys.** 27 (5): 474

[2] Binnig, G., Rohrer, H., Gerber, C., *et al.* (1982) Surface Studies by Scanning Tunneling Microscopy. **Phys. Rev. Lett.** 49 (1): 57–61

[3] Nordling, C., Sokolowski, E., and Siegbahn, K. (1957) Precision Method for Obtaining Absolute Values of Atomic Binding Energies. **Phys. Rev.** 105 (5): 1676–1677

[4] Palmer, R. E., Eves, B. J., Festy, F., *et al.* (2002) Scanning probe energy loss spectroscopy. **Surface Science**, 502-503: 224–231

[5] Festy, F. and Palmer, R. E. (2004) Scanning probe energy loss spectroscopy below 50nm resolution. **Appl. Phys. Lett.** 85 (21): 5034

[6] Lawton, J. J., Pulisciano, A, and Palmer, R. E. (2009) Local secondary-electron emission spectra of graphite and gold surfaces obtained using the Scanning Probe Energy Loss Spectrometer (SPELS). **J. Phys.: Condens. Matter**, 21 (47): 474206

[7] Eves, B. J., Festy, F., Svensson, K., *et al.* (2000) Scanning probe energy loss spectroscopy: Angular resolved measurements on silicon and graphite surfaces. **Appl. Phys. Lett.** 77 (25): 4223

[8] Arden, W. M. (2002) The International Technology Roadmap for Semiconductors – Perspectives and challenges for the next 15 years. **Curr. Opin. Solid State Mater. Sci.** 6 (5): 371–377

[9] Manoharan, H. C., Lutz, C. P., and Eigler, D. M. (2000) Quantum mirages formed by coherent projection of electronic structure. **Nature**, 403 (6769): 512–515

[10] Alivisatos, A. P. (1996) Semiconductor Clusters, Nanocrystals, and Quantum Dots. **Science**, 271 (5251): 933–937

[11] Duan, X. and Lieber, C. M. (2000) General Synthesis of Compound Semiconductor Nanowires. **Adv. Mater.** 12 (4): 298–302

[12] Alliata, D., Andolfi, L., and Cannistraro, S. (2004) Tip to substrate distances in STM imaging of biomolecules. **Ultramicroscopy**, 101 (2-4): 231–240

[13] Misra, M. and Egerton, R. F. (1984) Assessment of electron irradiation damage to biomolecules by electron diffraction and electron energy-loss spectroscopy. **Ultramicroscopy**, 15 (4): 337–344

[14] Kroto, H. W., Heath, J. R., O'Brien, S. C., *et al.* (1985) C60: Buckminsterfullerene. **Nature**, 318 (6042): 162–163

[15] Dekker, C. (1999) Carbon Nanotubes as Molecular Quantum Wires. **Phys. Today**, 52 (5): 22

[16] **Zyvex Technologies** [online]. Available from: http://zyvextech.com [Accessed Apr. 10, 2012]

[17] Binnig, G. (1982) Tunneling through a controllable vacuum gap. **Appl. Phys. Lett.** 40 (2): 178

[18] Binnig, G., Rohrer, H., Gerber, C., *et al.* (1983) 7 x 7 Reconstruction on Si(111) Resolved in Real Space. **Phys. Rev. Lett.** 50 (2): 120–123

[19] Gamow, G. (1928) Zur Quantentheorie des Atomkernes. **Z. Phys.** 51 (3-4): 204–212

[20] Gurney, R. W. and Condon, E. U. (1928) Wave Mechanics and Radioactive Disintegration. **Nature**, 122 (3073): 439–439

[21] Gurney, R. and Condon, E. (1929) Quantum Mechanics and Radioactive Disintegration. **Phys. Rev.** 33 (2): 127–140

[22] Sonnenfeld, R. and Hansma, P. K. (1986) Atomic-Resolution Microscopy in Water. **Science**, 232 (4747): 211–213

[23] Tersoff, J. and Hamann, D. R. (1985) Theory of the scanning tunneling microscope. **Phys. Rev. B**, 31 (2): 805–813

[24] Bardeen, J. (1961) Tunnelling from a Many-Particle Point of View. **Phys. Rev. Lett.** 6 (2): 57–59

[25] Tersoff, J. and Hamann, D. R. (1983) Theory and Application for the Scanning Tunneling Microscope. **Phys. Rev. Lett.** 50 (25): 1998–2001

[26] Crommie, M. F., Lutz, C. P., and Eigler, D. M. (1993) Imaging standing waves in a two-dimensional electron gas. **Nature**, 363 (6429): 524–527

[27] Feenstra, R., Stroscio, J. A., and Fein, A. (1987) Tunneling spectroscopy of the Si(111)2 x 1 surface. **Surf. Sci.** 181 (1-2): 295–306

[28] Gomer, R. (1992) **Field Emissions and Field Ionization** AVS Classics in Vacuum Science and Technology: American Inst. of Physics.

[29] Fowler, R. H. and Nordheim, L. (1928) Electron Emission in Intense Electric Fields. **Proc. R. Soc. A-Math. Phys. Eng. Sci.** 119 (781): 173–181

[30] Young, R. D. (1959) Theoretical Total-Energy Distribution of Field-Emitted Electrons. **Phys. Rev.** 113 (1): 110–114

[31] Good, R. H. and Müller, E. W. (1956) "Field Emission." In **Handbuch der Physik.** Vol. 21 Berlin, Göttingen, Heidelberg: Springer-Verlag.

[32] Young, R. and Müller, E. (1959) Experimental Measurement of the Total-Energy Distribution of Field-Emitted Electrons. **Phys. Rev.** 113 (1): 115–120

[33] Kirkpatrick, D. A., Mankofsky, A., and Tsang, K. T. (1992) Analysis of field emission from three-dimensional structures. **Appl. Phys. Lett.** 60 (17): 2065

[34] Young, R. (1972) The Topografiner: An Instrument for Measuring Surface Microtopography. **Rev. Sci. Instrum.** 43 (7): 999

[35] Fink, H. (1988) Point source for ions and electrons. **Phys. Scr.** 38 (2): 260–263

[36] Reihl, B. and Gimzewski, J. (1987) Field emission scanning auger microscope (Fesam). **Surf. Sci.** 189-190: 36–43

[37] Allenspach, R. and Bischof, A. (1989) Spin-polarized secondary electrons from a scanning tunneling microscope in field emission mode. **Appl. Phys. Lett.** 54 (6): 587

[38] Tomitori, M., Terai, H., and Arai, T. (1999) Energy spectrum of backscattered electrons excited by a field emission scanning tunneling microscope with a build-up [111]-oriented W tip. **Appl. Surf. Sci.** 144-145: 123–127

[39] Tomitori, M., Hirade, M., Suganuma, Y., *et al.* (2001) An applicability of scanning tunneling microscopy for surface electron spectroscopy. **Surf. Sci.** 493 (1-3): 49–55

[40] Xu, C., Chen, X., Zhou, X., *et al.* (2009) Spatially resolved scanning probe electron energy spectroscopy for Ag islands on a graphite surface. **Rev. Sci. Instrum.** 80: 103705

[41] Festy, F, Svensson, K, Laitenberger, P, *et al.* (2001) Imaging surfaces with reflected electrons from a field emission scanning tunnelling microscope: image contrast mechanisms. **J. Phys. D: Appl. Phys.** 34 (12): 1849–1852

[42] Yin, J., Pulisciano, A., and Palmer, R. E. (2006) Local Secondary-Electron Emission Spectra via Scanning Probe Energy Loss Spectroscopy. **Small**, 2 (6): 744–746

[43] Pulisciano, A., Park, S. J., and Palmer, R. E. (2008) Surface plasmon excitation of Au and Ag in scanning probe energy loss spectroscopy. **Appl. Phys. Lett.** 93 (21): 213109

[44] Song, M. Y., Robinson, A. P. G., and Palmer, R. E. (2010) Fabrication of co-axial field emitter tips for scanning probe energy loss spectroscopy. **Nanotechnology**, 21 (15): 155304

[45] Song, M. Y., Lawton, J. J., Robinson, A. P. G., *et al.* (2010) Scanning probe energy loss spectroscopy with microfabricated coaxial tips. **Phys. Rev. B**, 81 (16)

[46] Ruocco, A., Milani, M., Nannarone, S., *et al.* (1999) Scattering mechanism of electrons interacting with surfaces in specular reflection geometry: Graphite. **Phys. Rev. B**, 59 (20): 13359–13364

[47] Eves, B. J. (2002) **Scanning Probe Energy Loss Spectroscopy**. PhD thesis, University of Birmingham

[48] Tanuma, S., Powell, C. J., and Penn, D. R. (2011) Calculations of electron inelastic mean free paths. IX. Data for 41 elemental solids over the 50 eV to 30 keV range. **Surf. Interface Anal.** 43 (3): 689–713

[49] Penn, D. (1987) Electron mean-free-path calculations using a model dielectric function. **Phys. Rev. B**, 35 (2): 482–486

[50] Saldin, D. (1988) Angle-resolved electron-energy-loss spectroscopy: Atomic-core excitations at adsorbates on surfaces. **Phys. Rev. Lett.** 60 (12): 1197–1200

[51] Persson, B. (1980) Inelastic scattering of slow electrons from adsorbed molecules. **Surf. Sci.** 92 (1): 265–282

[52] Siller, L., Vanter, N., and Palmer, R. E. (2000) Negative ion resonance states of SF6 physisorbed on the graphite surface investigated by high-resolution electron energy loss spectroscopy. **Surf. Sci.** 465 (1-2): 76–80

[53] Thiry, P. A., Liehr, M, Pireaux, J. J., *et al.* (1987) Electron Interaction Mechanisms in High Resolution Electron Energy Loss Spectroscopy. **Phys. Scr.** 35 (3): 368–379

[54] Maier, S. A. (2007) **Plasmonics** Norwell: Springer.

[55] Gadzuk, J. and Plummer, E. (1973) Field Emission Energy Distribution (FEED). **Rev. Mod. Phys.** 45 (3): 487–548

[56] Meitner, L. (1922) Über die Entstehung der $\gamma$-Strahl-Spektren radioaktiver Substanzen. **Z. Phys.** 9 (1): 131–144

[57] Auger, P. (1925) Sur l'effet photoélectrique composé. **J. Phys. Radium**, 6 (6): 205–208

[58] Palmberg, P. W. (1968) Auger Electron Spectroscopy of fcc Metal Surfaces. **J. Appl. Phys.** 39 (5): 2425

[59] Lander, J. (1953) Auger Peaks in the Energy Spectra of Secondary Electrons from Various Materials. **Phys. Rev.** 91 (6): 1382–1387

[60] Mehlhorn, W (1998) 70 years of Auger spectroscopy, a historical perspective. **J. Electron Spectrosc. Relat. Phenom.** 93 (1-3): 1–15

[61] Palmberg, P. W. (1969) High Sensitivity Auger Electron Spectrometer. **Appl. Phys. Lett.** 15 (8): 254

[62] Seah, M. (1972) Quantitative Auger electron spectroscopy and electron ranges. **Surf. Sci.** 32 (3): 703–728

[63] Bommel, A. J. van, Crombeen, J. E., and Tooren, A. van (1975) LEED and Auger electron observations of the SiC(0001) surface. **Surf. Sci.** 48: 463–472

[64] **JKU, ZONA, Scanning Auger electron spectroscopy** [online]. Available from: http://www.jku.at/zona/content/e82347/e41471/ [Accessed May 10, 2012]

[65] Koh, A. L., Bao, K., Khan, I., *et al.* (2009) Electron Energy-Loss Spectroscopy (EELS) of Surface Plasmons in Single Silver Nanoparticles and Dimers: Influence of Beam Damage and Mapping of Dark Modes. **ACS Nano**, 3 (10): 3015–3022

[66] Sokolowski, E., Nordling, C., and Siegbahn, K. (1958) Magnetic analysis of X-ray produced photo and auger electrons. **Ark. Fys.** 12: 301–18

[67] Escher, M., Weber, N., Merkel, M., *et al.* (2005) NanoESCA: imaging UPS and XPS with high energy resolution. **J. Electron Spectrosc. Relat. Phenom.** 144-147: 1179–1182

[68] Bates, C., Wertheim, G., and Buchanan, D. (1979) Nature of the 3.8 eV plasmon in x-ray photoemission from silver. **Phys. Lett. A**, 72 (2): 178–180

[69] Daimon, H., Matsuda, H., Toth, L., *et al.* (2007) Stereo-PEEM for three-dimensional atomic and electronic structures of microscopic materials. **Surf. Sci.** 601 (20): 4748–4753

[70] Herzog, R. and Viehböck, F. (1949) Ion Source for Mass Spectrography. **Phys. Rev.** 76 (6): 855–856

[71] Liebl, H. (1967) Ion Microprobe Mass Analyzer. **J. Appl. Phys.** 38 (13): 5277

[72] Magee, C. W., Harrington, W. L., and Honig, R. E. (1978) Secondary ion quadrupole mass spectrometer for depth profiling - design and performance evaluation. **Rev. Sci. Instrum.** 49 (4): 477

[73] Lee, Y. J., Perdian, D. C., Song, Z., *et al.* (2012) Use of mass spectrometry for imaging metabolites in plants. **Plant J.** 70 (1): 81–95

[74] Orloff, J., Li, J.-Z., and Sato, M. (1991) Experimental study of a focused ion beam probe size and comparison with theory. **Journal of Vacuum Science Technology B: Microelectronics and Nanometer Structures**, 9 (5): 2609 –2612

[75] Guerquin-Kern, J., Wu, T., Quintana, C., *et al.* (2005) Progress in analytical imaging of the cell by dynamic secondary ion mass spectrometry (SIMS microscopy). **Biochim. Biophys. Acta-Gen. Subj.** 1724 (3): 228–238

[76] Wang, L., Ma, X., Qi, Y., *et al.* (2005) Controlled growth of uniform silver clusters on HOPG. **Ultramicroscopy**, 105 (1-4): 1–5

[77] MathWorks United Kingdom **MATLAB - The Language of Technical Computing** [online]. Available from: http://www.mathworks.co.uk/products/matlab/ [Accessed Apr. 10, 2012]

[78] BURLE ELECTRO-OPTICS INC. (n.d.) **Channeltron electron multiplier handbook for mass spectrometry applications**:

[79] Advanced Measurement Technology, Inc. ***ORTEC® Model 9302 Amplifier-Discriminator - Operating and Service Manual*** (2002), version C

[80] PHOTONIS USA, Inc. ***CEM 4502 EIC Specification*** (2010), version 30070

[81] Keithley Instruments, Inc. ***Model 6485 Picoammeter Instruction Manual*** (2001), version 6485-901-01 Rev. A

[82] Taylor, N. J. (1969) Resolution and Sensitivity Considerations of an Auger Electron Spectrometer Based on Display LEED Optics. **Review of Scientific Instruments**, 40 (6): 792

[83] **Omicron NanoTechnology GmbH** [online]. Available from: http://www.lktech.com/products/EA5000MCA.php [Accessed Apr. 3, 2015]

[84] Lucier, A., Mortensen, H., Sun, Y., *et al.* (2005) Determination of the atomic structure of scanning probe microscopy tungsten tips by field ion microscopy. **Phys. Rev. B**, 72 (23)

[85] **Philips XL 30 SEM | SEMTech Solutions** [online]. Available from: http://www.semtechsolutions.com/node/124/philips-xl-30-sem [Accessed June 5, 2012]

[86] Oatley, C. W. (1982) The early history of the scanning electron microscope. **J. Appl. Phys.** 53 (2): R1

[87] Lucier, A. (2004) **Preparation and Characterization of Tungsten Tips Suitable for Molecular Electronics Studies**. PhD thesis, McGill University

[88] Boling, J. L. and Dolan, W. W. (1958) Blunting of Tungsten Needles by Surface Diffusion. **J. Appl. Phys.** 29 (3): 556

[89] Binh, V. T. and Uzan, R. (1987) Tip shape evolution: Capillarity-induced matter transport by surface diffusion. I. **Surface Science**, 179 (2-3): 540–560

[90] Binh, V. T. and García, N. (1992) On the electron and metallic ion emission from nanotips fabricated by field-surface-melting technique: experiments on W and Au tips. **Ultramicroscopy**, 42-44: 80–90

[91] Waugh, A., Boyes, E., and Southon, M. (1976) Investigations of field evaporation with a field-desorption microscope. **Surface Science**, 61 (1): 109–142

[92] Tsong, T. T. and Müller, E. W. (1970) Field evaporation rates of tungsten. **Physica Status Solidi (a)**, 1 (3): 513–533

[93] Ekvall, I., Wahlström, E., Claesson, D., *et al.* (1999) Preparation and characterization of electrochemically etched W tips for STM. **Measurement Science and Technology**, 10 (1): 11–18

[94] Ernst, S., Wirth, S., Rams, M., *et al.* (2007) Tip preparation for usage in an ultra-low temperature UHV scanning tunneling microscope. **Science and Technology of Advanced Materials**, 8 (5): 347–351

[95] Nanotec **WSxM Program** [online]. Available from: http://www.nanotec.es/products/wsxm/index.php [Accessed May 10, 2012]

[96] Horcas, I., Fernandez, R., Gomez-Rodriguez, J. M., *et al.* (2007) WSXM: A software for scanning probe microscopy and a tool for nanotechnology. **Rev. Sci. Instrum.** 78 (1): 013705

[97] **Gwyddion - Free SPM (AFM, SNOM/NSOM, STM, MFM, ...) data analysis software** [online]. Available from: http://gwyddion.net/ [Accessed May 10, 2012]

[98] Image Metrology A/S **Image Metrology - SPIP** [online]. Available from: http://www.imagemet.com/ [Accessed May 10, 2012]

[99] Dickreuter, S., Gleixner, J., Kolloch, A., *et al.* (2013) Mapping of plasmonic resonances in nanotriangles. **Beilstein Journal of Nanotechnology**, 4: 588–602

[100] Jensen, T. R., Malinsky, M. D., Haynes, C. L., *et al.* (2000) Nanosphere Lithography: Tunable Localized Surface Plasmon Resonance Spectra of Silver Nanoparticles. **The Journal of Physical Chemistry B**, 104 (45): 10549–10556

[101] Levlin, M. and Laakso, A. (2001) Evaporation of silver thin films on mica. **Applied Surface Science**, 171 (3-4): 257–264

[102] Francis, G. M., Kuipers, L., Cleaver, J. R. A., *et al.* (1996) Diffusion controlled growth of metallic nanoclusters at selected surface sites. **Journal of Applied Physics**, 79 (6): 2942

[103] Wan, K., Lin, X., and Nogami, J. (1993) Surface reconstructions in the Ag/Si(111) system. **Phys. Rev. B**, 47 (20): 13700–13712

[104] Gangnaik, A., Georgiev, Y. M., McCarthy, B., *et al.* (2014) Characterisation of a novel electron beam lithography resist, SML and its comparison to PMMA and ZEP resists. **Microelectronic Engineering**, 123: 126–130

[105] Wiener, A., Duan, H., Bosman, M., *et al.* (2013) Electron-Energy Loss Study of Nonlocal Effects in Connected Plasmonic Nanoprisms. **ACS Nano**, 7 (7): 6287–6296

[106] **LK Technologies, Inc** [online]. Available from: http://www.omicron.de/en/home [Accessed May 10, 2012]

[107] Maeda, F., Takahashi, T., Ohsawa, H., *et al.* (1988) Unoccupied-electronic-band structure of graphite studied by angle-resolved secondary-electron emission and inverse photoemission. **Physical Review B**, 37 (9): 4482–4488

[108] Xu, C. K., Liu, W. J., Zhang, P. K., *et al.* (2014) Nonlinear inelastic electron scattering revealed by plasmon-enhanced electron energy-loss spectroscopy. **Nature Physics**

[109] Love, G and Scott, V. D. (1978) Evaluation of a new correction procedure for quantitative electron probe microanalysis. **Journal of Physics D: Applied Physics**, 11 (10): 1369–1376

[110] Assad, A. M. D. and El Gomati, M. M. (1998) Backscattering coefficients for low energy electrons. **Scanning Microscopy**, 12 (1): 185

[111] **AFM Principles, Universität Greifswald** [online]. Available from: http://www3.physik.uni-greifswald.de/method/afm/eafm.htm [Accessed Oct. 2010]

[112] Baroody, E. (1950) A Theory of Secondary Electron Emission from Metals. **Phys. Rev.** 78 (6): 780–787

[113] Furuya, K. (2008) Nanofabrication by advanced electron microscopy using intense and focused beam. **Sci. Technol. Adv. Mater.** 9 (1): 014110